

University of St Andrews



Full metadata for this thesis is available in
St Andrews Research Repository
at:

<http://research-repository.st-andrews.ac.uk/>

This thesis is protected by original copyright

THE UNIVERSITY OF ST. ANDREWS

Spiral waves in accretion discs

Danny Steeghs

Submitted for the degree of Ph.D.

30 September 1999



TH
0524

ABSTRACT

This thesis discusses observations of the interacting binary IP Pegasi and shows that its accretion disc carries strong, tidally driven spiral arms during outburst. The distribution of line emission across the accretion disc is resolved using Doppler tomography and reveals a two armed spiral pattern in a variety of emission lines. The spirals persist as a strong co-rotating pattern throughout the outburst maximum for at least 8 days, while the disc radius decreases exponentially. During quiescence, the disc lacks such open spirals but remains non-axisymmetric.

Hydrodynamical simulations are used to calculate the properties of thin accretion discs carrying tidal density waves. Predicted emission line properties and simulated image reconstructions reproduce the observations in detail and confirm that the spiral structure observed in IP Pegasi is a tidally driven phenomenon. The IP Pegasi observations provide the first convincing evidence for tidally driven spirals that were proposed over 13 years ago as a possible source of angular momentum transport in accretion discs. The disc simulations also indicate that similar disc structure is expected in other systems carrying large discs such as dwarf novae in outburst and nova-like variables. For small, cool accretion discs, tidally driven spiral waves can be present but are too tightly wrapped to be resolved in the strong emission lines.

It is clear that tidally driven waves can severely alter the global dynamics and structure of accretion discs. However, a significant amount of shear viscosity is still needed to switch from a small disc in quiescence to the large disc observed in outburst so that strong open spirals are generated. How much angular momentum can be transported via such waves in comparison to angular momentum dispersal through local viscous processes remains to be quantified by comparing realistic model calculations with present and future observations.

DECLARATION

I, Daniel Theodore Hubert Steeghs, hereby declare that this thesis, which is approximately 35 000 words in length has been written by me, that it is the record of work carried out by me and that it has not been submitted in any previous application for a higher degree

I was admitted as a research student in October, 1996 and as a candidate for the degree of Ph.D. in Astronomy in October, 1997; the higher study for which this is a record was carried out in the University of St. Andrews between 1996 and 1999.

In submitting this thesis to the University of St. Andrews I understand that I am giving permission for it to be made available for use in accordance with the regulations of the University Library for the time being in force, subject to any copyright vested in the work not being affected thereby. I also understand that the title and abstract will be published, and that a copy of the work may be made and supplied to any bona fide library or research worker.

St.Andrews, 30 September 1999

I hereby certify that the candidate has fulfilled the conditions of the Resolution and Regulations appropriate for the degree of Ph.D. in the University of St. Andrews and that the candidate is qualified to submit this thesis in application for that degree.

St.Andrews, 30 september 1999

ACKNOWLEDGMENTS

Most of all I am indebted to Prof. Keith Horne for all his help and guidance in the past years. His enthusiasm has been very stimulating for me, and I hope he enjoyed this time as much as I have. The hours in the coffee room juggling with plots have been of great help, although I hope I haven't taken the hint of his '*I'm the boss*'-mug too lightly.

I would like to thank Emiliou Harlaftis for providing me with all the IP Pegasi data that feature in this thesis, and for his help and advice. The night time trips to Dundee are not to be dismissed either of course. Thanks also to the members of the National Observatory of Athens and the University of Athens for their hospitality during my stay in Greece.

Rudolph Stehle supplied the hydrodynamical accretion disc simulations that are discussed in Chapter 4, and I thoroughly enjoyed working with him. Tom Marsh is thanked for his advice and his most useful set of data reduction/analysis software that he made readily available.

On the financial side I would like to thank the University of St. Andrews for awarding me a University Scholarship. St. Leonard's College for awarding a Russell Trust Grant to finance my SAAO observing trip. Many thanks to the Head of School of Physics & Astronomy for generously awarding a travel grant that allowed me to participate in observing trips and attend conferences. The British Council is thanked for their financial contribution to my visit to Athens in 1998.

Cheers to all the members of the astronomy group at St. Andrews for the good time I had. Kieran & Marti for putting up with that *dodgy foreigner*, and all the good laughs we had in and outside the office. Dave for the many *Cossack* adventures to Edinburgh airport and for, well, being Dave. I hope the 'tigerrrrrrrrr'-roar may prove to be useful.

To friends and family in Holland, thanks for the support and interest you all showed in the past years. '*Pap en Mam, danke veur alles, misschien wuurt det nog es get met ugge klcinc remmel*'.

Kara, thanks for love and happiness.

CONTENTS

Abstract	i
Declaration	ii
Acknowledgements	iii
List of Figures	ix
List of Tables	x
1 Introduction	1
1.1 Mass transfer in binary stars	2
1.1.1 Cataclysmic variables	3
1.1.2 Accretion discs	4
1.1.3 Dwarf novae and disc instabilities	6
1.2 The angular momentum enigma	7
1.2.1 The α prescription	8
1.2.2 Local disc hydrodynamics	9
1.2.3 Global waves: spiral arms	9

1.2.4	Magnetic fields; an α after all?	14
1.3	Observing the accretion phenomena in CVs	16
2	Astro-tomography	19
2.1	Eclipse mapping	20
2.2	Doppler tomography	22
2.3	Echo tomography	31
3	The dwarf nova IP Pegasi	32
3.1	An eclipsing dwarf nova above the period gap	32
3.2	The observations	35
3.3	Data reduction	38
3.4	The accretion disc	39
3.5	The companion star and disc thickness	58
4	Simulating tidal spiral waves	63
4.1	The grid of hydrodynamic disc models	63
4.2	Emission lines from spiral shocks	65
4.2.1	Doppler tomograms and line profiles	65
4.3	Model predictions	70
4.3.1	Axisymmetric discs	71
4.3.2	Model I: High Mach number disc	71
4.3.3	Model II: dwarf nova outbursts	75
4.4	Reconstructing spiral structures using tomography	78

4.4.1	Realistic data quality	78
4.4.2	High M model	79
4.4.3	Low M model	80
4.4.4	Instrumental requirements	81
4.4.5	Other emission line sources	84
4.5	The influence of spiral waves on light curves	87
4.6	Summary	92
5	Comparing theory and observations	94
5.1	The spiral wave interpretation of the disc in IP Pegasi	94
5.2	Is IP Pegasi alone?	100
6	Conclusions	107
6.1	Dissecting the accretion disc	107
6.2	The dwarf nova IP Pegasi	108
6.3	Searching for spiral waves	108
6.4	The success of a tidal interpretation	109
A	List of Publications	111
	REFERENCES	113

LIST OF FIGURES

1.1	The Roche potential	2
1.2	Cartoon of a Cataclysmic Variable	5
1.3	The grand design spiral in M51	10
1.4	A 3D simulation of the gas flow in a binary	12
1.5	A global MHD simulation of a Keplerian disc	15
2.1	An eclipse map of IP Pegasi	22
2.2	The formation of a double peaked line profile from a disc	23
2.3	Doppler coordinates in relation to Cartesian XY coordinates in the binary frame	26
2.4	A maximum entropy reconstruction of phase resolved emission line data . . .	28
2.5	Doppler tomography of the polar HU Aqr in two states	30
3.1	Long term lightcurve of IP Peg	36
3.2	A statistical analysis of the outburst behaviour	37
3.3	Doppler maps of IP Pegasi at the start of an outburst	40
3.4	The azimuthal properties of the observed disc images	41
3.5	A model disc carrying spiral arms	43
3.6	The azimuthal dependence of a two armed spiral pattern	44

3.7	Subtracting the secondary star contribution	45
3.8	IP Pegasi in quiescence	47
3.9	The outburst spectrum of IP Peg	48
3.10	Orbital continuum and emission line lightcurves	49
3.11	The HeII and Bowen blend emission lines in outburst	50
3.12	The velocity resolved eclipse of HeII4686	51
3.13	HeII4686 tomogram	52
3.14	The average H α profiles	54
3.15	The disc radius evolution	56
3.16	H α from the companion star	59
3.17	High ionisation emission from the Roche lobe	61
4.1	Some physical properties of the Model I simulation	66
4.2	Some physical properties of the Model II simulation	67
4.3	The temperature radius behaviour of the models	68
4.4	The line emission from a high Mach number disc	72
4.5	The effect of shear broadening	73
4.6	Gaussian fits to the phase dependence of the emission line peaks	75
4.7	Line emission from an open spiral pattern	76
4.8	The departure from Keplerian velocity field	77
4.9	Synthetic data and reconstructed tomograms for Model I	80
4.10	Synthetic data and reconstructed tomograms for Model II	81
4.11	Comparing the asymmetries in the Doppler tomograms	82

4.12	The properties of low vs. high Mach number discs	83
4.13	Some representative maximum entropy reconstructions	85
4.14	The influence of signal to noise on recovered image contrast	86
4.15	Monochromatic eclipse lightcurves across the UV/optical wavebands	88
4.16	A comparison between lightcurves from a symmetric disc and the two models	89
4.17	A radial cut through the disc; the disc scale height	91
5.1	The observed IP Pegasi Doppler tomogram in comparison to a model reconstruction	95
5.2	Comparison of finite difference and SPH simulations of the disc flow in IP Pegasi	97
5.3	Doppler tomography of SS Cygni in outburst	102
5.4	Doppler tomography of the eclipsing nova-like V347 Puppis	104

LIST OF TABLES

3.1	IP Pegasi system parameters	33
3.2	Journal of Observations	35
3.3	Disc properties from the average $H\alpha$ profiles	55
3.4	Red star contribution to the $H\alpha$ line flux	60
3.5	The red star emission across the Roche lobe	61

CHAPTER 1

Introduction

Accretion concerns the extraction of gravitational potential energy from material falling into a potential well. Though nuclear fusion is the central energy source that allows a star to withstand the gravitational forces due to its own mass, the most energetic phenomena in the universe are powered by the large amount of potential energy that can be freed through accretion. These potential wells can be the massive mass concentrations in centers of galaxies, compact objects formed as the end product of stellar evolution, and very young stellar objects surrounded by ambient gas after a cloud collapse. In all cases matter is accreted by the central compact object and the potential energy is released in the form of radiation and heat.

The burning of hydrogen into helium as occurs in the sun and during most of any star's lifetime, liberates a steady rate of energy in its core. For the proton-proton cycle the energy liberated through fusion per hydrogen nucleus of mass m_p amounts to $\Delta E_{pp} = 0.007m_p c^2$, or in terms of energy per unit rest mass, the efficiency of nuclear fusion is about 0.7%. In comparison, the amount of potential energy that is freed by accreting a mass m from infinity onto a central object with mass M and radius R is $\Delta E_{acc} = \frac{GMm}{R}$. The efficiency of accretion is thus directly proportional to the compactness M/R of the central object. For example a neutron star with mass $1.4M_\odot$ and a radius of ~ 10 km, would give an efficiency of 20%.

The Roche potential for $q=0.5$

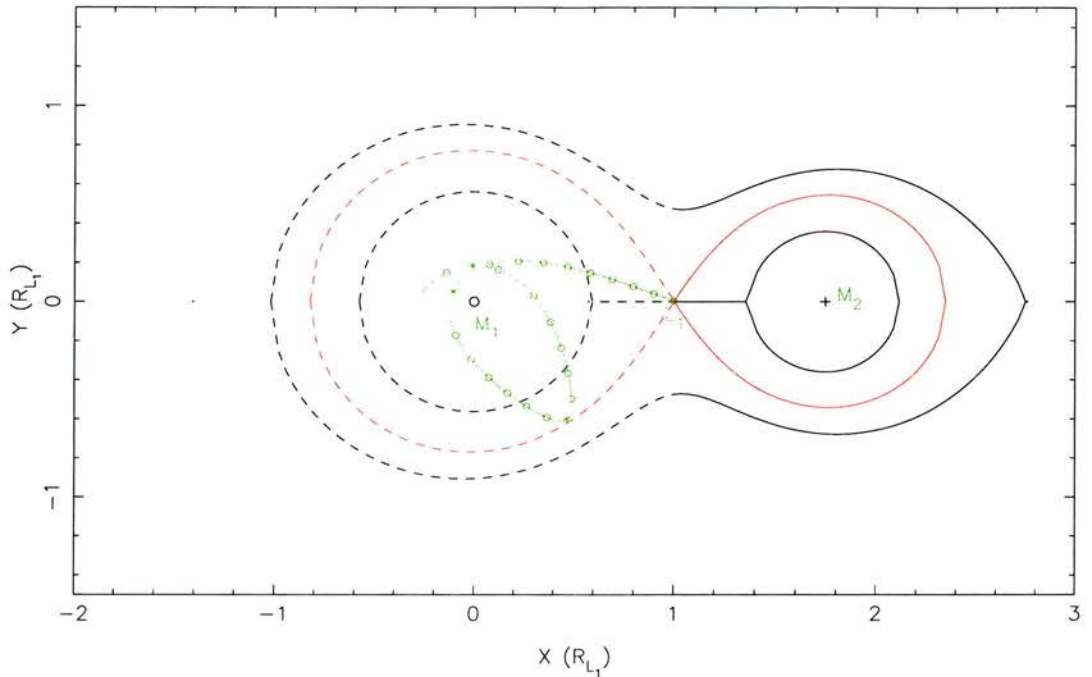


Figure 1.1: *The equipotential surfaces in the orbital plane of a binary system with mass ratio $q = M_2/M_1 = 0.5$. Shown are three curves of the Roche potential, above, below and at the critical value that defines the Roche lobes of the two stars (red). The critical point between the two stars is the first Lagrangian point ($L1$). From now on the positive x -axis points towards the donor star (M_2), with the compact object (M_1) as origin. A simple test particle trajectory injected from the $L1$ point from the less massive star towards the compact object is plotted in green.*

1.1 Mass transfer in binary stars

Binary stars are a natural environment where accretion is important. More than half of all stars are dynamically bound to a nearby companion. Though most of these are wide, long period systems, mass transfer can occur in a variety of circumstances as the orbits decay over time and the separation between the two stars decreases. Mass transfer and the resulting accretion flow thus determines the long term evolution of the binary as well as the fate of the stellar components. Typically the more massive stellar component evolves first and leaves a compact stellar object, followed by the expansion of the companion star as it evolves on a longer time-scale until it fills the critical Roche lobe volume in the binary potential and mass

transfer commences (e.g. Rappaport, Joss & Webbink 1982; Verbunt 1993). Mass transfer through Roche lobe overflow (Figure 1.1) powers almost all galactic accretion sources. It was the binary setting that made it possible to establish the existence of stellar black holes by means of the orbital motion of the orbiting companion star that feeds the compact object (Cowley 1992).

This thesis is concerned with the dynamics of accretion through Roche lobe overflow onto white dwarfs. This class of interacting binaries is called cataclysmic variables (CVs), and provides a formidable laboratory to study accretion physics. There are several reasons for choosing cataclysmic variables and not the more energetic X-ray binaries containing neutron stars and black holes to study the physics of accretion. A typical CV consists of a $0.7M_{\odot}$ white dwarf and a slightly lower mass late-type star that fills its Roche lobe in a close binary orbit. Such systems are fairly common, more so than neutron star binaries, and have the advantage of being relatively close, typically a few hundred parsecs. The white dwarf potential well results in accretion energies that are radiated mostly in the optical and ultraviolet wavebands, whereas the more compact sources emit mostly in the X-ray regime. This opens up the opportunity to study the accretion flows using ground based telescopes and well developed optical instruments. The orbital periods range between 1 and 10 hours, and so dynamical time scales are very accessible to human observers.

1.1.1 Cataclysmic variables

Documented observations of the systems collectively called CVs date back to the earliest records we have of celestial events. The so-called novae are thought to be thermonuclear runaway events on the surface of the white dwarf triggered when a critical amount of mass is accreted. Although this interpretation dates from the second half of this century, novae have been observed for millennia (e.g. Duerbeck 1987). In 1855, Hind observed a new kind of variable star, U Geminorum (Hind 1856), which would form the first member of the so-called dwarf novae. These systems exhibit semi periodic outburst, during which they brighten by several magnitudes compared to their quiescent state. The second object in this class was SS Cygni (Wells 1896), the brightest CV visible from earth and now one of the best studied variable stars, for which an almost continuous light curve since its discovery is available.

The modern picture of CVs was mostly motivated by spectroscopic work in the 40's and 50's, showing several CVs to be spectroscopic binaries. The Roche lobe model was put together by Crawford & Kraft (1956) in their study of AE Aqr, where they first proposed the picture of a late-type star filling its Roche lobe and transferring mass to the primary star. Dynamically stable mass transfer can occur over long time scales as long as the donor star is less massive than the white dwarf. This means that the companions in CVs are low mass late-type stars of type K or M. Approximately 600 CVs have been identified now and for about 300 of these orbital periods have been measured (Ritter & Kolb 1998). I refer to Warner (1995) for a very extensive review of all material related to CV research.

The CV population is divided into several sub classes.

- The classical and recurrent *novae*; large outbursts that are powered by thermonuclear events on the surface of the white dwarf
- *dwarf novae*; exhibit semi-periodic changes in the mass accretion rate, leading to small amplitude outbursts
- *nova-like variables*; steady high mass-transfer rate systems
- magnetic CVs; containing a magnetised white dwarf that is able to control part (*intermediate polars*) or all (*polars*) of the accretion flow

1.1.2 Accretion discs

As material leaves the donor star near its L1 point, it carries the orbital angular momentum with it as it is pulled into the potential well of the white dwarf. This prevents the gas from falling directly onto the white dwarf as is demonstrated by the particle trajectory in Figure 1.1. In order for it to do so, the angular momentum has to be extracted on its way in. The gas spirals in through a geometrically thin accretion disc which is the medium for this momentum dispersal (Figure 1.2). Angular momentum transport is therefore a fundamental process for accretion to occur. The formation of an accretion disc can be understood from a few simple arguments. As gas is continuously fed through the L1 point by the donor star, it initially circularises at the circular orbit corresponding to its specific angular momentum.

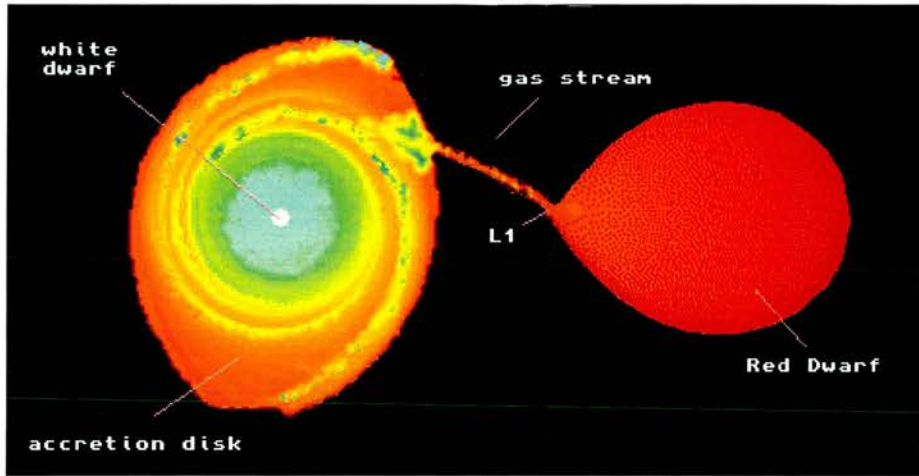


Figure 1.2: *A cataclysmic variable transfers mass from a late-type star onto a thin accretion disc around the white dwarf. In the cool outer regions the impact of the gas stream causes a local bright spot.*

Angular momentum dispersal through viscous interaction ensures that some gas slowly spirals inwards, while other particles carry the excess angular momentum to larger radii. The ring thus spreads and forms a thin disc. It is the detailed process of angular momentum transport that determines the properties of accretion flows in close binaries. Before turning to this exchange of angular momentum I will review a few fundamental properties of accretion discs. Note that this standard paradigm of accretion via a disc is not confined to binary stars. A very similar geometry is used to model active galactic nuclei and the discs around young stars, where a similar angular momentum barrier exists.

Close to the white dwarf with mass M_1 and radius R_1 , the orbits are circular, with angular velocity v_ϕ equal to the Keplerian velocity;

$$v_\phi = v_{Kep}(R) = \sqrt{GM_1/R} \quad (1.1)$$

A small radial velocity v_r exists that allows material to accrete at a rate $v_r \sim \nu/R$ due to the presence of a kinematic viscosity ν . If we demand a steady state, that is at each radius the mass inflow from larger radii (\dot{M}) is balanced by mass outflow towards smaller radii, one can calculate the structure of such discs using mass and angular momentum conservation and a prescription for the viscosity (Pringle 1981; Frank, King & Raine 1985). In the vertical direction the scale height H is set by demanding hydrostatic equilibrium between gravity and gas pressure and is then:

$$\frac{H}{R} = \frac{c_s}{v_\phi} \quad (1.2)$$

with c_s the local sound speed. In other words, the disc is geometrically thin if and only if the local Keplerian velocity is highly supersonic, i.e. the azimuthal Mach number $M = \frac{v_\phi}{c_s} \gg 1$. The Keplerian velocities around a white dwarf range between a few thousand km/s in the inner disc regions down to several hundred km/s at the outer disc. The sound speed of hydrogen gas at $10^4 K$ is only 10 km/s, so the discs in CVs are indeed expected to be highly supersonic and therefore geometrically thin. Treating the disc as an infinite uniform plane, the importance of self gravity can be estimated by comparing the magnitude of the self-gravity force, $\sim G\rho H$, to the vertical gravitational force due to the primary, $\sim GM_1 H/R^3$. Self gravity can thus be neglected since $\rho \ll M_1/R^3$ at all radii (Frank, King & Raine 1985). At larger radii the influence of the companion star can no longer be ignored and particle orbits will no longer be circular and may even cross (Paczynski 1977). Ultimately it is through these tidal forces of the companion star that the angular momentum of the disc is extracted from the disc altogether and coupled back into the binary's orbit (Papaloizou & Pringle 1977; Lin & Papaloizou 1979). Roughly half of the available potential energy is radiated ; $L_{disc} = \frac{GM_1\dot{M}}{2R_1}$ whereas the other half goes into the kinetic energy of the gas. Viscous dissipation in this picture is the heat source which is subsequently radiated away locally. In the steady state situation this then dictates the temperature structure of the disc to be:

$$T(R) = \left(\frac{3GM_1\dot{M}}{8\pi R^3\sigma} \left[1 - \left(\frac{R_1}{R} \right)^{1/2} \right] \right)^{1/4} \propto R^{-3/4} \text{ for } R \gg R_1 \quad (1.3)$$

Near the surface of the white dwarf, the kinetic energy is then dissipated in the so-called boundary layer where the rapidly rotating disc material connects with the surface material of the spinning white dwarf.

1.1.3 Dwarf novae and disc instabilities

The dwarf nova systems are a particularly intriguing class of CVs that provide many opportunities to test our understanding of accretion. These highly time-dependent systems tell us that accretion is not a steady process, and understanding their behaviour in detail is a

challenging task. There are various subclasses within the group of dwarf nova systems, but the common cause of their semi periodic outbursts is thought to be due to a thermal disc instability (Osaki 1996). The rapid change in opacity when hydrogen ionises around 7000K provides two stable branches for thin viscous accretion discs. On the one hand a cool, low mass accretion rate branch in the quiescent state, and on the other a hot, high mass accretion rate state during outburst. The two branches are connected via an unstable branch that leads to a limit cycle behaviour of the disc, alternating between the two states (Meyer & Meyer-Hofmeister 1981). The instability is triggered locally when some annulus in the disc exceeds the local critical surface density and enters the unstable branch. A heating wave then propagates through the disc and switches the whole disc to a high state. Although this basic picture has been very successful, there is still a poor understanding of the details that govern the equilibrium relations for accretion discs (Livio 1999). Numerical disc instability calculations are still only 1D, and it is clear that many effects are not satisfactorily controlled (e.g Hameury et al. 1998), limiting their predictive power. An alternative process that could modulate the mass accretion rate through the disc would be a time dependent mass-transfer rate from the companion star. A poor understanding of the atmospheres of the rapidly rotating companion stars makes it difficult to quantify the mass transfer rate history that is expected.

1.2 The angular momentum enigma

I now return to the important question of angular momentum transport in accretion discs. I have already mentioned the importance of the kinetic viscosity term ν in driving the accretion onto the compact star, without specifying a prescription for this. From now on (as in all the literature on accretion) viscosity in this text refers to the collective processes that transport angular momentum on a local scale. To illustrate that this point has to be made I estimate the molecular viscosity of gas in a typical accretion disc:

$$\nu_{mol} \sim \frac{10^{10} T^{5/2}}{ln\Lambda n} \quad \text{cm}^2/\text{s} \quad (1.4)$$

T is the temperature in K, $ln\Lambda$ the Coulomb logarithm and n the particle number density per cm^{-3} (Livio 1994). The hydrodynamical Reynolds number is defined as:

$$Re = \frac{v_\phi R}{\nu_{mol}} \quad (1.5)$$

The Reynolds number for typical CV discs ($M_1 \sim M_\odot$, $n \sim 10^{15}$, $T \sim 10^4$, $\ln \Lambda \sim 10$) is of the order of 10^{14} , and molecular viscosity is thus dynamically totally unimportant since $Re \gg 1$. This is why the term viscosity as it is used in the accretion physics community has little to do with the kinematic viscosity as defined in fluid hydrodynamics. Yet we observe high accretion luminosities from accretion discs and we see the dwarf nova systems adjusting to radical changes in the accretion rate in the course of a few days. The viscous timescale can be written as:

$$\tau_{visc} = \frac{R}{v_r} = \frac{R^2}{\nu} = Re \frac{R}{v_\phi} \quad (1.6)$$

With R/v_ϕ being of the order of hours, one needs an effective Reynolds number of the order of $Re \sim 10^2$ to explain a viscous timescale of a few days. Somehow efficient angular momentum transport is occurring throughout these discs, and this poses a serious and still unsettled problem in accretion theory. What is the physical foundation of the angular momentum transport in accretion discs?

1.2.1 The α prescription

Shakura & Sunyaev (1973) considered two alternative ways to generate local viscous angular momentum transport; turbulence and magnetic stresses. On dimensional grounds they argued that the turbulent viscosity can be written as a product of a typical turbulent velocity and length scale, i.e. $\nu_{turb} \sim v_{turb} \times l_{turb}$. Turbulent eddies are most likely smaller than the scale height H of the disc and the turbulent velocity is sub-sonic so $\nu_{turb} \sim \alpha c_s H$ with $\alpha \leq 1$ (Lynden-Bell & Pringle 1974). A similar argument was made that the magnetic Maxwell stresses $B_r B_\phi / 4\pi$ represent a source of shear viscosity and can be parameterised by an α in the sense that $\nu_{r\phi} \sim \langle \frac{B_r B_\phi}{4\pi} \rangle \leq \langle \frac{B^2}{4\pi} \rangle \leq p$ since the magnetic pressure is smaller than the gas pressure p . Without theoretical understanding of the processes involved, this is really only a convenient prescription that allows us to parameterise the unknown viscosity processes in a dimensionless constant α . The big success of this prescription is that one can then solve

and model the structure of thin viscous discs. As I will discuss in section 1.2.4, only recently has there been considerable theoretical breakthrough in establishing a physical basis for such turbulent viscosity, although not to the level that we actually have a workable prescription for the viscosity. The α prescription is therefore still the fudge factor used in most accretion disc models. Observations suggest that angular momentum transport in CV discs demands an α between 0.01 and 0.3.

1.2.2 Local disc hydrodynamics

The very large Reynolds number in accretion flows might suggest that the sheared flow is unstable towards hydrodynamical turbulence. However the Rayleigh criterion for linear stability is always satisfied in Keplerian accretion discs where velocity increases inwards and angular momentum increases outwards (Chandrasekhar 1961). Unless a non-linear instability operates, purely hydrodynamical turbulence is not likely to be a viable angular momentum transport mechanism. Balbus, Hawley & Stone (1996) and Hawley, Balbus & Winters (1999) performed a series of local 3D numerical simulations to investigate the non-linear stability of shear flows and found that initial finite amplitude perturbations quickly die out in a Keplerian flow. Keplerian flows seem therefore to be also non-linearly stable towards turbulence.

Ryu & Goodman (1992) investigated the angular momentum transport in discs which were convectively unstable. They found that the associated angular momentum transport is very small and actually inwards. Apart from the fact that it is not clear if convection is relevant for binary accretion discs, it will transport angular momentum in the wrong direction.

It appears therefore that it is very unlikely that angular momentum can be transported *locally* in Keplerian accretion discs via purely hydro-dynamical processes.

1.2.3 Global waves: spiral arms

An alternative hydrodynamical phenomenon was brought into attention by Sawada, Matsuda & Hachisu (1986). When performing 2D simulations of mass transfer via Roche lobe overflow, a strong two armed spiral pattern developed in their disc simulations. Numerical viscosity was kept very low, in order to investigate the properties of inviscid discs, and could only

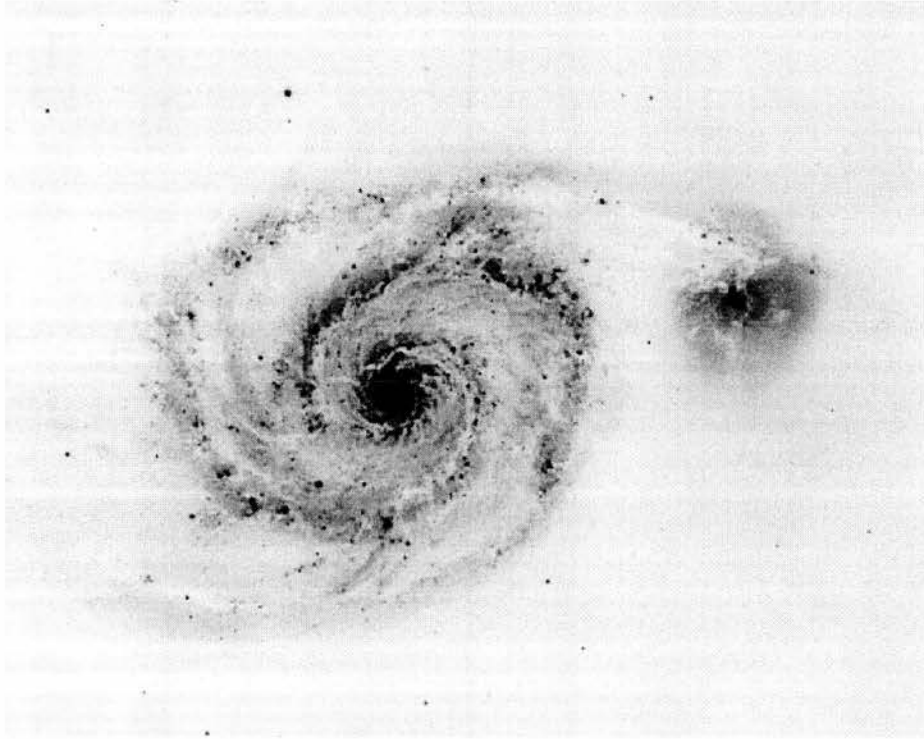


Figure 1.3: *A grand design spiral pattern in the galactic context; the galaxy M51 is one of the prime examples of a galactic disc carrying a spiral density wave, perhaps triggered by the nearby companion galaxy.*

contribute to a small fraction of the angular momentum transport that was going on (Sawada et al. 1987). Angular momentum dissipation in the spiral shocks was responsible for the bulk transport of angular momentum outwards and disc material inwards. This novel, non-local way of transporting angular momentum is possible since the tidal torques of the companion star effectively extract the disc's angular momentum through such tidally generated waves. The ability of density waves to transport angular momentum in self gravitating discs (Figure 1.3) is well known (Toomre 1969; Binney & Tremaine 1987; Bonnel & Bates 1994) since this transport is a direct result from purely gravitational interaction. Waves of this type can still transport angular momentum in the absence of self gravity provided that a dissipative mechanism exists that exchanges angular momentum between the trailing wave and the fluid (Spruit et al. 1987). The angular momentum of a wave in the high frequency limit can be estimated by $\frac{1}{2}\rho v^2 m/\sigma$, with m the azimuthal order of the wave and σ the wave frequency in a frame co-moving with the fluid (Spruit et al. 1987). In the co-rotating frame of the fluid, a trailing wave travels in the opposite direction and thus $m/\sigma < 0$, i.e. the wave carries

negative angular momentum with respect to the fluid. Exchange of angular momentum will thus slow the fluid down, and increases the angular momentum of the wave, making it less negative. This is the basis of angular momentum transport via density waves.

In the outer regions of the accretion disc, the disc gas revolves around the white dwarf on non-axisymmetric orbits where the streamline–density for a pressure free gas is highest towards the secondary and lowest normal to it (Paczynski 1977). In a low–temperature disc, the shape of the streamlines are still similar to the pressure free gas, but the variation of the streamline–density with azimuth along a particle orbit will excite pressure waves which steepen to shock waves while they travel inward (Spruit, Matsuda, Inoue & Sawada 1987). Additionally, shocks can be excited by the crossing of particle orbits if the disc is larger than the tidal radius. The opening angle of the shock arms depend mainly on the azimuthal Mach number $M = v_\phi/c_s$, i.e. the wave is wound up in the angular direction at roughly the local Keplerian speed as it propagates inwards with the sound speed (Różyczka & Spruit 1989).

Even though the tidal forces are effective only in directly perturbing the flow in the outer disc, the above effects will shear such perturbations into trailing spiral waves that can in principle travel all the way down to the compact object. Several groups have since found such prominent spiral arms to develop in 2D disc simulations (e.g. Matsuda et al. 1990, Różyczka & Spruit 1993, Savonije, Papaloizou & Lin 1994, Heemskerk 1994) for various mass ratios. Spruit (1987) developed a self-similar approach in order to handle the problem analytically. He also estimated the angular momentum transport to be comparable with an $\alpha \leq 0.01$ when radiative losses are taken into account. Whereas this is most likely reasonable in the inner regions, the self similar approach breaks down in the outer regions of the disc. Indeed, Matsuda et al. (1990) compare the effective α obtained from numerical simulations to those of self similar shocks. Whereas their values converged to self similar solutions in the inner disc, the strengths of the shocks in the outer disc regions were considerably higher. The effective α for those simulations where a strong function of mass ratio and varied between $\alpha_{eff} \sim 10^{-3} - 10^{-1}$. Obviously angular momentum dispersal via spiral shocks is strongly dependent on radius (e.g. Savonije et al. 1994), so is not well described by a single α parameter. Unfortunately since radiative cooling was not taken into account, the disc temperatures in those simulations were too high and since the efficiency of spiral shocks

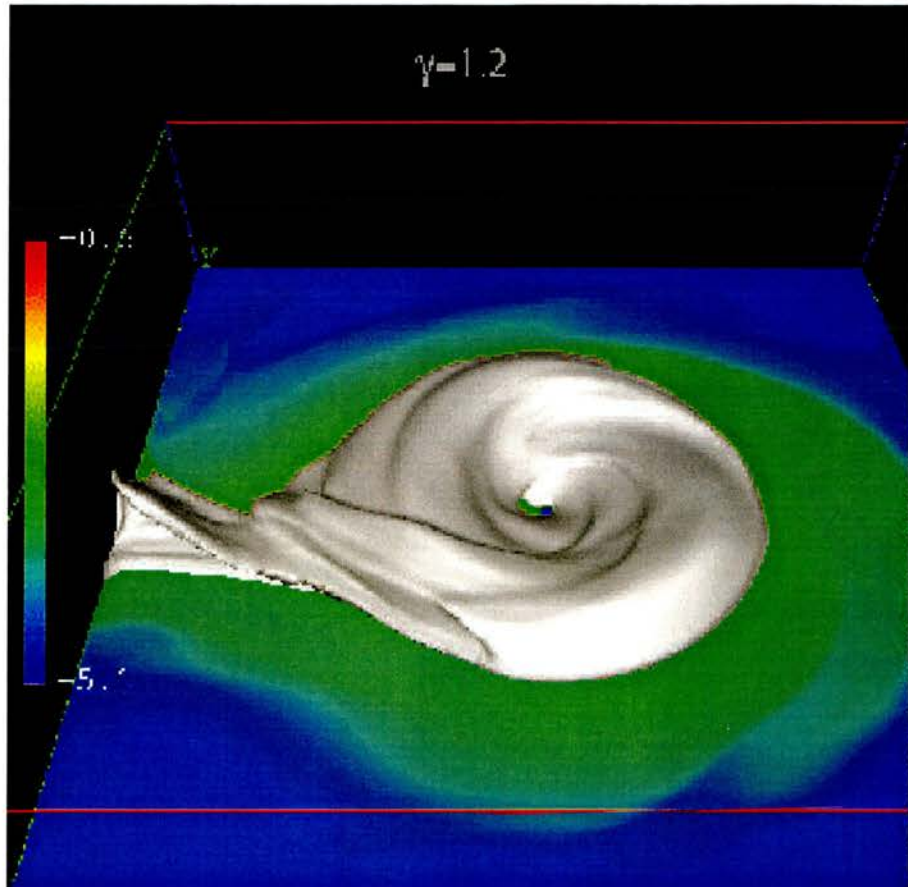


Figure 1.4: A 3D simulation of the gas flow in a binary using a polytropic equation of state by Makita et al. (1998). Tidally driven spiral shocks are clearly visible in this particle density plot.

decreases with decreasing temperature, it is not clear how much angular momentum transport can actually be achieved in realistic discs.

In order to truly assess the implications of such waves to the angular momentum budget of discs, realistic 3D simulations are required, with realistic physics for the local heating and cooling of the disc as well as enough resolution to resolve the vertical structure. Since these are global waves, the disc as a whole has to be simulated at this level. This formidable computational task means that some sacrifices have to be made. Yukawa, Boffin & Matsuda (1997) performed 3D particle simulations for non-viscous gas, but without radiative cooling. Again, prominent spiral shock arms form, but the intrinsic numerical viscosity introduced by particle methods makes it difficult to disentangle the angular momentum transport of the spirals compared to viscous transport. They also note, that in order to resolve such

features the number of particles used is very important. The results of Yukawa et al. (1997) are in stark contrast to those claimed by Lanzafame et al. (1992), with significantly less particles. Makita, Miyawaki & Matsuda (1998) performed both 2D and 3D simulations using an Eulerian scheme. They report steady state spiral arms in 3D for a range of polytropic indices (Figure 1.4). Although confirming that spiral arms can form in 3D environments, these simulations are still without radiative cooling, leading to very hot accretion disc temperatures.

An alternative approach was pursued by Stehle & Spruit (1999) and Stehle (1999). Their simulations involved a 2D numerical grid with additional equations for the vertical motions that allowed the disc scale height to vary for each grid point. The advantage of this was that 3D effects were captured to first order, and realistic radiative losses could be calculated for each grid cell. The disc temperatures were chosen to reflect the conditions of CV accretion discs in a high mass transfer state. In addition, a local shear viscosity was included to investigate its effect on the properties of the spiral arms. They also pointed out that vertical resonances can occur within the disc for the mass ratios relevant to CVs, and that due to the tidal forcing the disc height will vary dramatically across the disc and can significantly depart from the hydrostatic equilibrium value. In Chapter 4 I will use these simulations to construct synthetic emission line profiles and light curves that can be compared with observations.

Note that such global waves can co-exist with local turbulent viscosity. Indeed in Savonije et al. (1994) and Stehle (1999) a shear viscosity $\nu_{r\phi}$ in the parameterisation of Shakura & Sunyaev's α was included. A strong *radial* viscous force (bulk viscosity as opposed to shear viscosity), if present in accretion discs, may on the other hand damp the shocks over a short range or may even prevent the pressure disturbance to steepen into a shock (Savonije, Papaloizou & Lin 1994). This is most likely why some particle methods with intrinsic bulk viscosity (Larwood 1997) have difficulty in resolving the sharp spiral waves.

It appears that accretion via tidally induced shock waves is a viable angular momentum transport mechanism in accretion discs, however the amplitude of this transport may not be sufficient to explain the accretion rate in CV discs. The possibility that such a process occurs together with a local shear-type viscosity means that its relevance to the overall disc dynamics should not be dismissed, even if its contribution to the angular momentum transport is not

sufficient to drive accretion in the inner disc. I will come back to this point extensively in Chapter 5.

1.2.4 Magnetic fields; an α after all?

Hydrodynamic and *magneto*-hydrodynamic (MHD) discs behave in fundamentally different ways. Balbus & Hawley (1991) pointed out that a linear MHD instability already investigated by Velikhov (1959) and Chandrasekhar (1961), had dramatic implications for the prospect of MHD turbulence in astrophysical accretion discs. The presence of a weak magnetic field is sufficient to de-stabilise the flow and provide an environment for self-sustained MHD turbulence (Hawley, Gammie & Balbus 1995, Brandenburg et al. 1995, Stone et al. 1996). The instability operates in sheared flows that have a small seed magnetic field and whose angular velocity increases inwards. Imagine two fluid elements at different radii r_1, r_2 in the disc, connected by a magnetic field B . With the field line there is an associated magnetic tension force $B^2/4\pi$ that tries to conserve the field lines' shape. When $d\Omega/dr < 0$ and $r_2 > r_1$, the fluid element at r_1 orbits more rapidly and the field line is stretched. The two elements can therefore be viewed as two masses connected with a massless string with tension $B^2/4\pi$ (Balbus & Hawley 1998). If the two fluid elements are moved apart, m_1 loses angular momentum to m_2 . Thus the inner fluid element moves in further while the outer element moves outwards corresponding to the orbits of their new angular momentum value. This stretches the string (i.e. the magnetic field) even further and we have an instability provided the magnetic tension is not too strong. This limit on the magnitude of the magnetic tension thus places an upper limit on the field strength for this instability to work. Balbus & Hawley (1998) show that for coupling to a vertical field, the Alfvén speed must significantly exceed the sound speed in order to stabilise the disc.

Angular momentum transport via magnetic fields is possible via the Maxwell stress $\propto B_r B_\phi$, as long as a specific correlation between radial and toroidal magnetic fields exists such that $\langle B_r B_\phi \rangle$ does not vanish. Local 3D simulations indeed demonstrate that net angular momentum transport outwards is achieved with an effective α of 0.005-0.02. The presence of a net vertical field produces much stronger turbulence and can obtain $\alpha \geq 0.1$ (Hawley & Balbus 1999), although such results depend on the specific choice of boundary conditions



Figure 1.5: *A 2D simulation of MHD flow in a Keplerian disc. Left the radial magnetic field component, right the azimuthal field. Through correlation between the two, angular momentum transport outwards is possible. From Armitage (1998).*

(Torkelson, private communication).

Some attempts at global disc simulations have recently been undertaken. Matsimoto & Shibata (1997) simulated a constant angular momentum torus embedded in a vertical magnetic field in 3D. Armitage (1998) simulated a Keplerian disc in 2D and showed how an initial vertical field lead to turbulence and angular momentum transport (Figure 1.5). Hawley & Balbus (1999) presented some first results of their own global code. The main concern here is that grid resolution will limit the possibility to resolve the turbulence at its smallest length scales.

MHD turbulence appears to be essential in order to transport angular momentum in a local turbulent way as envisaged by Shakura & Sunyaev (1973). As more physics is put into the numerical models, we should reach the point where such models have clear predictive power that would allow us to confirm if MHD turbulence is indeed producing the shear viscosity powering angular momentum transport in discs and if an α parameterisation is appropriate. I remark that, just like for the case of spiral density waves, it has not yet been convincingly demonstrated that MHD turbulence can provide a shear viscosity of $\alpha \geq 0.1$ for a realistic accretion disc.

1.3 Observing the accretion phenomena in CVs

The accretion disc temperatures in CVs range from several thousand K in the outer regions to several tens of thousands close to the white dwarf with the resulting emission spanning the optical/UV wavelengths. The white dwarf is usually heated to several tens of thousands of degrees due to accretion, and becomes an important source in the UV regime (Sion 1999), with typically only a small contribution in the optical waveband. The other stellar component is a cool red dwarf whose contribution to the continuum light is only appreciable in the far red and infrared (Dhillon & Marsh 1995, Dhillon 1998). The optical window is therefore ideal to study the accretion disc, since it is usually the dominant light source in that waveband.

A traditional tool that is invaluable in the study of variable stars are orbital light curves of eclipsing systems. If the orbital inclination is large enough (greater than 70° or so), the Roche lobe of the companion star is able to cover the white dwarf and its accretion flow from view near inferior conjunction of the white dwarf and its accretion disc. The multi-color continuum emission from the accretion disc and white dwarf is then progressively eclipsed each binary orbit, allowing a fairly direct measurement of several binary parameters (e.g. Cook & Warner 1984). In some cases the light curves are dominated by a prominent hump just before eclipse, associated with the impact of the ballistic gas stream with the accretion disc. In other cases, no hump is evident and the light curve shows the gradual eclipse of an extended accretion disc. The presence of a hump does allow one to constrain system parameters by measuring the ingress and egress phases of the spot in the continuum (e.g. Wood et al. 1986).

Spectroscopy reveals prominent emission lines from the Balmer series as well as some neutral helium and ionised helium, carbon, nitrogen and oxygen line emission. In some low inclination systems absorption lines as opposed to emission lines are formed indicating large optical depths in the disc. The broad emission lines are formed in the accretion disc, and their shape is dominated by the Doppler broadening introduced by the large Keplerian velocities in the disc. Emission line formation in the accretion disc is a process that is poorly understood (e.g. Robinson, Marsh & Smak 1993). Fortunately, since the shape of the lines are dominated by the dynamical Doppler shifts, the exact shape of the local line profile does not affect the

analysis of the line shapes much, so some properties of the flow can be directly inferred from the profile shapes. The detection of P Cygni profiles in IUE spectra of high \dot{M} CVs (Cordova & Mason 1982, Knigge & Drew 1997) shows that in the inner regions, outflows may become important in addition to the supersonic flow in the accretion disc. In particular, the way in which the disc and white dwarf are connected via the boundary layer is an area that is still not well understood.

Magnetic fields are important on various scales, from the possibly turbulent MHD fields within the disc to ordered magnetic fields anchored to the stellar components. Near a magnetic white dwarf, magnetic forces become as important as gravitational forces and will dominate the accretion flow. In the so-called polars, the field is so strong that no disc is formed and the matter flows, after an initial ballistic free fall from the L1 point, along magnetic field lines onto the poles of the white dwarf (Cropper 1990). In intermediate polars, the field is not so strong and a disc is still formed but truncated once magnetic forces take over. These magnetic systems are recognized by their large X-ray flux, produced near the white dwarf as the in-falling gas makes a shock wave above the surface and a considerable number of them have been discovered from the ROSAT sky survey (Verbunt et al. 1997). The magnetic field from the rapidly rotating companion star may well have important consequences for the short and long term evolution of CVs. Unfortunately, on the observational side, we have not yet been able to measure the surface magnetic fields on these stars.

Variability is observed on many timescales; the recurrent novae with typical timescales of many years, the rapid flickering occurring on timescales of seconds, and the coherent oscillations with periods around 30s found in some systems. There are three fundamental timescales that govern the evolution of geometrically thin discs. The shortest timescale is the dynamical timescale, which is the Keplerian period, that ranges from seconds near the white dwarf to hours at the outer disc:

$$\tau_{dyn} \sim 1/\Omega \sim R/v_\phi \sim H/c_s \quad (1.7)$$

The thermal timescale is the ratio of the thermal content to the local dissipation rate:

$$\tau_{th} \sim \frac{c_s^2}{\nu\Omega^2} \sim \frac{\tau_{dyn}}{\alpha} \quad (1.8)$$

which is a factor of $1/\alpha$ longer than the dynamical timescale and will be several hours to

days. The viscous timescale is the time it takes for gas to viscously drift inwards and is given by:

$$\tau_{visc} \sim \frac{R^2}{\nu} \sim \frac{R^2}{\alpha c_s H} \sim \frac{1}{\alpha} \frac{R^2}{H^2} \tau_{dyn} \quad (1.9)$$

which is again an order of magnitude longer and is of the order of several days. It is the accessibility of all these timescales that make CVs so fruitful as laboratories of high energy astrophysics.

CHAPTER 2

Astro-tomography

With a typical distance of 100 pc and a binary separation of a few solar radii, the angle subtended by a CV on the sky works out to be of the order:

$$\theta_{CV} \sim \frac{R_{\odot}}{d} \sim \frac{10^{11} \text{ cm}}{10^{20} \text{ cm}} \sim 10^{-9} \text{ degrees} \sim 10^{-6} \text{ arcseconds} \quad (2.1)$$

Direct imaging of the stellar components and the accretion flow is therefore out of the question as these sources will be point sources in even unrealistically large telescopes. To further our understanding we will need to fit physical models to the light curves and spectra of CVs in the hope that such models only depend on a small number of physical parameters which can then be determined from the observations (e.g. Frank & King 1981, Zhang & Robinson 1987). Unfortunately, our understanding of the physics of accretion discs and their emitted spectrum is still too poor for this approach to be successful.

An alternative approach to the problem was pioneered by Horne (1985), who developed a method to derive the brightness distribution of an accretion disc through maximum likelihood fitting of the observed light curves of eclipsing systems. Maximum entropy optimisation was used to derive a model independent spatially resolved image of the continuum emission from the accretion disc. This *eclipse mapping* was the first of a number of indirect imaging methods whose aim are to provide spatially resolved images of the accretion flows in close binary systems, thus effectively achieving micro-arcsecond resolution. This Chapter will discuss three types of imaging methods currently in use for the study of interacting binaries.

2.1 Eclipse mapping

The orbital light curves of the eclipsing systems are characterised by periodic dips of several magnitudes when the accretion disc and white dwarf are covered by the Roche-lobe filling companion star. The mass ratio and orbital inclination uniquely sets the geometry of this eclipsing system, and with these two parameters one can predict the shape of the light curve given a model for the binary components. An arbitrary brightness distribution across the accretion disc translates into a particular eclipse shape. Eclipse mapping inverts this process and finds the brightness distribution I that can fit the observed light curve O (Figure 2.1). In effect, the intensity of each image pixel is treated as a free parameter. The distribution map is adjusted in order to achieve a good fit with the data as quantified by the maximum likelihood χ^2 statistic;

$$\chi^2 = \frac{1}{N} \sum_{k=1}^N \left[\frac{O(k) - P(k)}{\sigma(k)} \right]^2 \quad (2.2)$$

with N the number of observed data points $O(k)$ with uncertainty $\sigma(k)$, and $P(k)$ the predicted data for the current image I with M elements (pixels). As a one dimensional light curve does not uniquely constrain a two dimensional brightness distribution, a regularisation constraint in the form of an image entropy was introduced by Horne (1985). Image entropy as a measure of image smoothness was then maximised to recover the 'smoothest' image I that would fit to the data. The image entropy S is defined relative to a so-called default image D , and it is via the particular choice of the default that one has some control over the recovered image structure;

$$S = \sum_{j=1}^M I(j) - D(j) - I(j) \ln \frac{I(j)}{D(j)} \quad (2.3)$$

The image entropy is then maximised when the image I equals the default image. Given the constraints to fit the data to a specified level as quantified by χ^2 , the choice of default image determines the structure that is favored through the maximum entropy criterion. One can demand for example the most uniform image by setting the default to be a constant image, or the most axisymmetric image if the default is the average of all image values at a particular

radius from the white dwarf. The latter choice is appropriate if one is interested in the radial dependence of the disc, e.g. the recovery of a temperature profile if multi-color light curves are available (Horne 1993).

Horne & Cook (1985) used UBV light curves of the dwarf nova Z Cha to map the accretion disc during early decline from an outburst. The optical colors of the disc in Z Cha fall between blackbodies and main sequence stellar atmospheres, implying an optically thick disc. The derived brightness temperature profile corresponds closely to a steady state disc accreting mass at a rate of $3 \times 10^{-9} M_{\odot} yr^{-1}$. However in dwarf novae in quiescence and in some of the nova-like variables, a much flatter profile is recovered (e.g. Wood et al. 1986, Wood, Horne & Vennes 1992, Rutten, van Paradijs & Tinbergen 1992). This would imply a disc far from steady state, accreting gas at much higher rates in the outer disc compared to the inner regions. Perhaps the energy in the inner regions is not radiated away but carried away by an outflow (e.g. a disc wind), or there are additional energy dissipation mechanisms in the outer disc. However, care must be taken that such profiles are derived under the assumption that no self occultation occurs anywhere within the disc. Geometrically thick disc structures could block the inner disc regions from view and alter the apparent temperature profile (Smak 1994, Marsh 1999).

Since the original eclipse mapping code was presented by Horne, a variety of extensions to it have been developed. One assumption of the original code was that all emission was confined to the orbital plane, i.e. the disc is infinitely thin. For very high inclinations and high mass-transfer rate discs, this assumption is clearly violated and changes to the disc geometry have been included to address these issues; for example the inclusion of a flared disc with a constant opening angle, or the addition of image pixels to represent the contribution from the bright spot and/or disc rim (e.g. Bobinger et al. 1997). Rutten et al. (1993) presented an extension to the technique called spectrally resolved eclipse mapping, by constructing independent eclipse maps for a large number of wavelength bins from a spectrophotometry dataset. Given the stack of recovered accretion disc images as a function of wavelength, a spectrum for a particular position in the disc can then be constructed by slicing through this stack. In, for example UX UMa, Baptista et al. (1998) recover a blue continuum with absorption lines in the inner disc, whereas the disc spectrum is much redder and contains

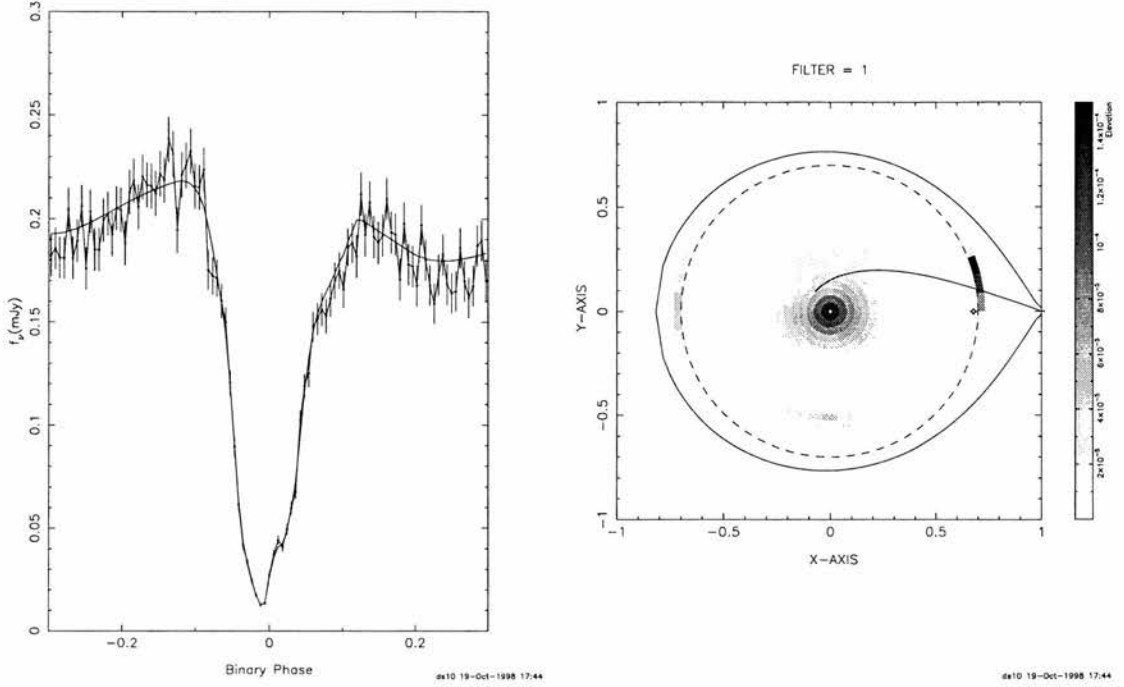


Figure 2.1: *Left: an eclipse of the binary IP Pegasi (points with error bars) and the fit achieved by the eclipse mapping method (solid line) using the code by Bobinger (1999). Right: The corresponding eclipse map of the accretion disc, carrying a strong hot spot.*

emission lines in the outer regions. Such spatially resolved disc spectra are extremely useful observational tests for accretion disc atmosphere modeling. More recent developments are the physical parameter eclipse mapping (Vrielmann et al. 1999) that aims to spatially resolve physical parameters such as surface density and temperature from multi-color data.

2.2 Doppler tomography

The optical spectra of CVs are characterised by strong emission lines that are Doppler broadened to a width of several thousands of km/s due to the large Keplerian velocities in the inner disc. The origin of most emission line flux lies in the accretion disc, which produces a double peaked emission profile (Figure 2.2). Each region in the disc contributes to the local profile at its radial velocity with respect to the observer, by an amount proportional to the local line emissivity. Fortunately, since the local thermal line profile has only a width of ~ 10 km/s, the global shape is not affected by the exact shape of the local line profile, and it can thus be used to analyse the gas dynamics in the disc (e.g. Smak 1981, Horne & Marsh 1986). Any

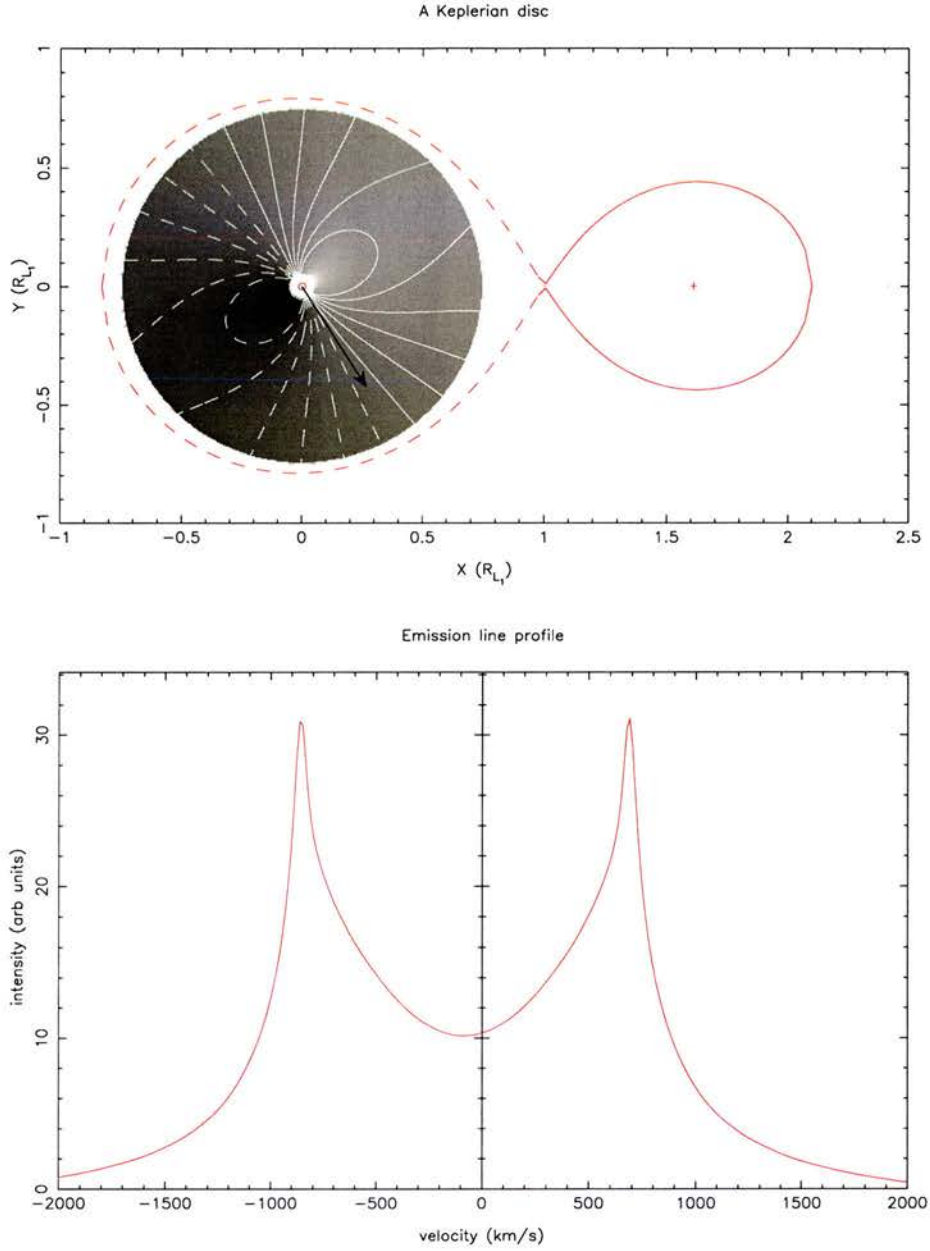


Figure 2.2: *The emission line profile formed by a uniform, Keplerian accretion disc. Top shows the binary geometry including an extended accretion disc with Keplerian orbits around the white dwarf. The grayscale denotes the radial velocity of the disc material with respect to an observer that is sitting in the direction of the arrow. Contours of constant radial velocity form a dipole pattern. The line profile (bottom) is the sum of all disc elements Doppler shifted to their radial velocity. A double peaked profile is the result, where the peaks correspond to the outer disc regions coming towards and going away from the observer. The profile is slightly off-centered due to the radial velocity of the white dwarf.*

asymmetry in the line emissivity across the disc will enhance a particular bin of the line profile. As the binary rotates, this enhanced site will have a different radial velocity with respect to the observer, tracing a sinusoidal curve in the radial velocity-orbital phase plane (trailed spectrogram) with a period equal to the orbital period of the binary. The amplitude of the radial velocity curve then gives the true velocity of the disc region, and its phasing the phase angle of the spot. In this way the line profile can be viewed as the sum of all contributions across the disc, each represented by a specific sinusoidal velocity curve (S-wave):

$$v(\phi) = \gamma - (V_x \sin(2\pi\phi) + V_y \cos(2\pi\phi)) \sin(i) + V_z \cos(i) \quad (2.4)$$

with i the inclination of the binary, γ the radial velocity of the binary system, and V_x, V_y, V_z the velocity vector (\vec{v}) components in the binary frame. From now on the x -axis will be defined as the line between the two stars, the y -axis perpendicular to it in the orbital plane of the binary, and the z -axis orthogonal to the orbital plane. In order to relate this velocity to a position in the binary system, one needs to know the velocity field of the disc material. For example, under the assumption of Keplerian velocities, one could then calculate the position corresponding to each velocity vector.

If we have a particular line emissivity distribution across the accretion disc, we can therefore predict the phase dependent emission line profiles produced by this disc. Or in reverse, if we observe the emission lines as a function of phase, one can reconstruct the distribution of line emission across the disc. Doppler tomography was introduced by Marsh & Horne (1988) to achieve such image reconstructions from observed CV emission lines. Rather than assuming a velocity field, a reconstruction in velocity space was favored (Marsh 1986). Each point (V_x, V_y) in the reconstructed Doppler map can then be traced by a specific S-wave having amplitude V_x and V_y . Therefore it is very straightforward to produce a predicted trailed spectrogram from a Doppler map. Since no assumptions are made regarding the velocity field, this approach also applies to emission line sources not related to the Keplerian flow. In Figure 2.3 the relation between these Doppler coordinates and the spatial coordinates in the binary frame is explored. Each emission line source will contribute at a corresponding pixel in the Doppler image, and we can therefore easily separate and resolve the various components of the binary. The two stars perform a solid body rotation in the binary, corresponding to the radial velocity amplitudes K_1 (white dwarf) and K_2 . These

two velocity vectors are mapped onto the V_x axis at $V_y = +K_2$ and $-K_1$. Because of the solid body rotation, the Roche lobe shape is conserved, and the secondary maps to a Roche lobe shaped area in the Doppler map. The ballistic gas stream can be similarly mapped by plotting its velocity coordinates in the tomogram. A circular accretion disc around the white dwarf will produce a circular image centered around the white dwarf at $V_x = 0, V_y = -K_1$. Each radius in the disc corresponds to a particular Keplerian velocity, and will map to a ring at that velocity in the Doppler image. The azimuthal structure (spots 1-8 in Figure 2.3), is conserved, but the radial structure is mapped inside out. Inner disc emission is found at high velocities, in the outer regions of the map, whereas the outer disc is mapped towards the inner regions of the map. The disc edge will provide an edge to the disc emission in the tomogram, at slightly higher velocities than the red star.

In order to reconstruct such Doppler tomograms from real data, the simplest procedure is to perform a back-projection. The *back projection* method traces all possible S-waves and calculates the average flux through that particular S-wave (Horne 1991). Each wave corresponds to a point in the Doppler map, and the average flux gives its intensity. Note that one is only able to derive an orbital phase averaged flux distribution, which is one of the fundamental limitations of Doppler tomography. It assumes that each emission site is equally visible at all phases. Combined with a Fourier filter, the filtered back projection provides a straightforward and fast way of calculating Doppler tomograms from phase-resolved spectroscopy (Horne 1991).

However, the presence of noise and phase gaps introduces artifacts in the recovered image structure. Maximum entropy algorithms can then be used to recover a smooth image in a very similar way to in eclipse mapping. The big difference here is that the 2D data set almost completely determines the image structure, and the maximum entropy optimisation merely removes noise artifacts. Although slower than a back projection, the maximum entropy based Doppler tomography technique allows an image reconstruction without strong artifacts even with poor signal to noise and/or phase coverage. All Doppler tomograms presented in this thesis are based on the DOPPLER-code developed by Tom Marsh. This Fortran code is based on the MEMSYS optimiser (Skilling & Bryan 1984), and implements various choices for the default image. Again, the procedure is very similar to the case of eclipse mapping.

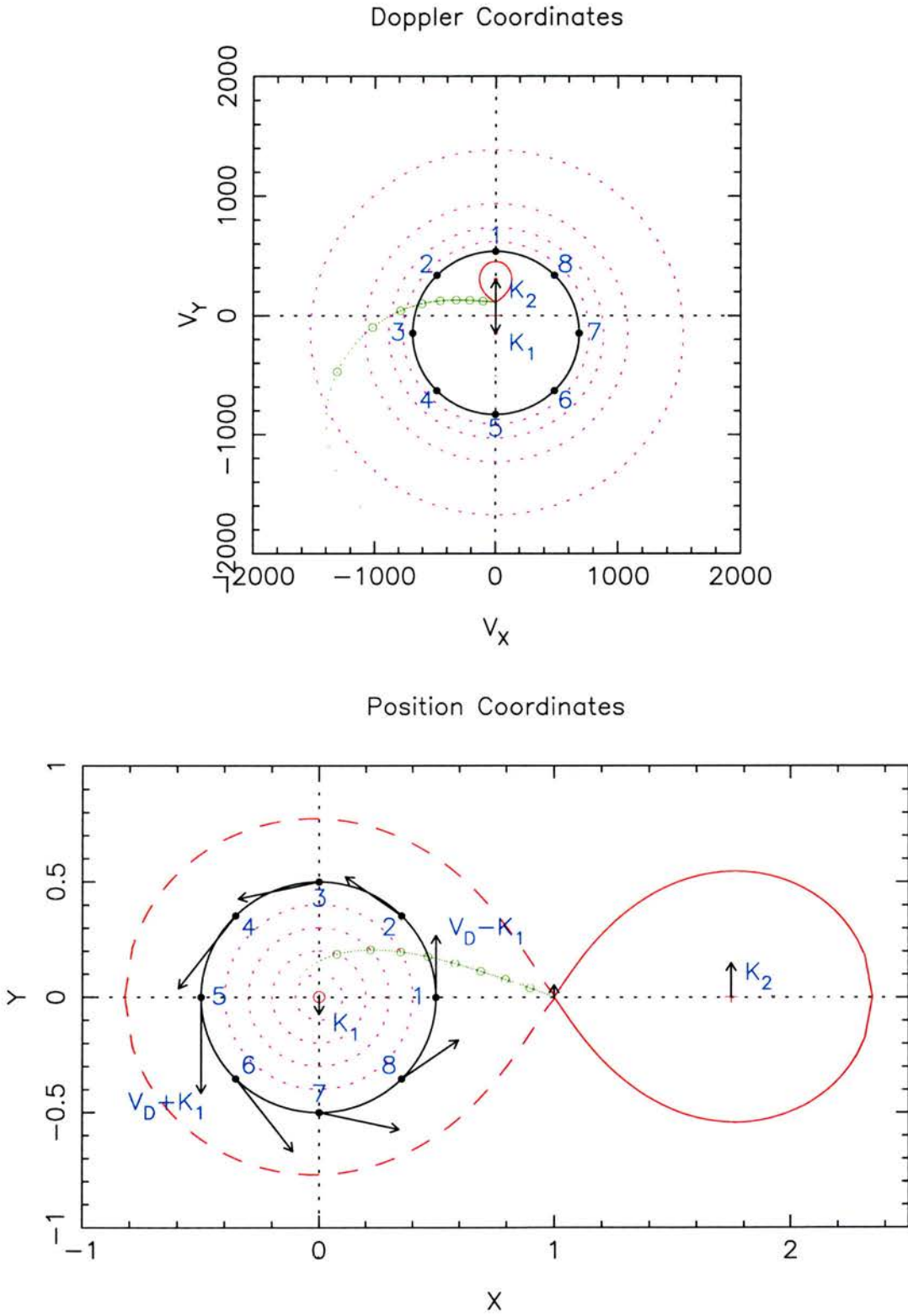


Figure 2.3: The Doppler coordinates used in Doppler maps (top) compared to the Cartesian XY coordinates in the binary frame. See text for details.

The Doppler image I is adjusted in order to minimise χ^2 whilst maximising the entropy relative to the supplied default D . After each iteration, a new default image is calculated by applying a Gaussian filter to the current image. This low pass filter ensures that the global image structure is conserved, whereas local noise artifacts are removed. The iterations are converged when the required χ^2 value is achieved and entropy is maximised. This balance between simplicity (maximising entropy) and realism (fitting to the data) can be quantified using a Lagrangian multiplier α . One then finds the image I that minimises:

$$Q^2 = \chi^2(I) - \alpha S(I, D) \quad (2.5)$$

α controls the tradeoff between the two, as α approaches 0, the maximum likelihood solution is approached, whereas for $\alpha \rightarrow \infty$, entropy dominates and I approaches the default image. Some input is thus required to select the desired trade-off between the two. The trajectory of maximum entropy solutions run from $I = D$ at $\alpha \rightarrow \infty$ to $\alpha = 0$. Along this trajectory the contours of constant χ^2 are tangent to those of the entropy, i.e. the gradients of χ^2 and entropy are parallel vectors. To ensure that convergence is reached, a test criterion is calculated that measures the angle θ between $\nabla\chi^2$ and ∇S ;

$$TEST = \frac{1}{2} \left| \frac{\nabla\chi^2}{|\nabla\chi^2|} - \frac{\nabla S}{|\nabla S|} \right|^2 \sim 1 - \cos\theta \quad (2.6)$$

Iterations are stopped once this criterion falls below 10^{-5} (see also Horne 1994).

Figure 2.4 demonstrates a maximum entropy reconstruction using fake data. A model accretion disc consisting of an axisymmetric line distribution falling off as a powerlaw with radius and a Gaussian spot of enhanced emission was used to generate the data in the top left panel. The double peaks of the disc and the S-wave corresponding to the spot are clearly visible. Random noise was added to simulate a signal-to-noise of 30, assuming a continuum level comparable to the level of the peaks (top, right). The reconstructed maximum entropy image (middle, right) is a slightly blurred version of the input model due to the presence of noise but captures all details. The predicted data (bottom, left) fits the observed data with a χ^2 of 1, and the corresponding residuals between fit and data (bottom, right) are small. This technique can be applied to a variety of accretion configurations as one does not assume a particular velocity field or geometry. Its main limitation is that one can only recover features

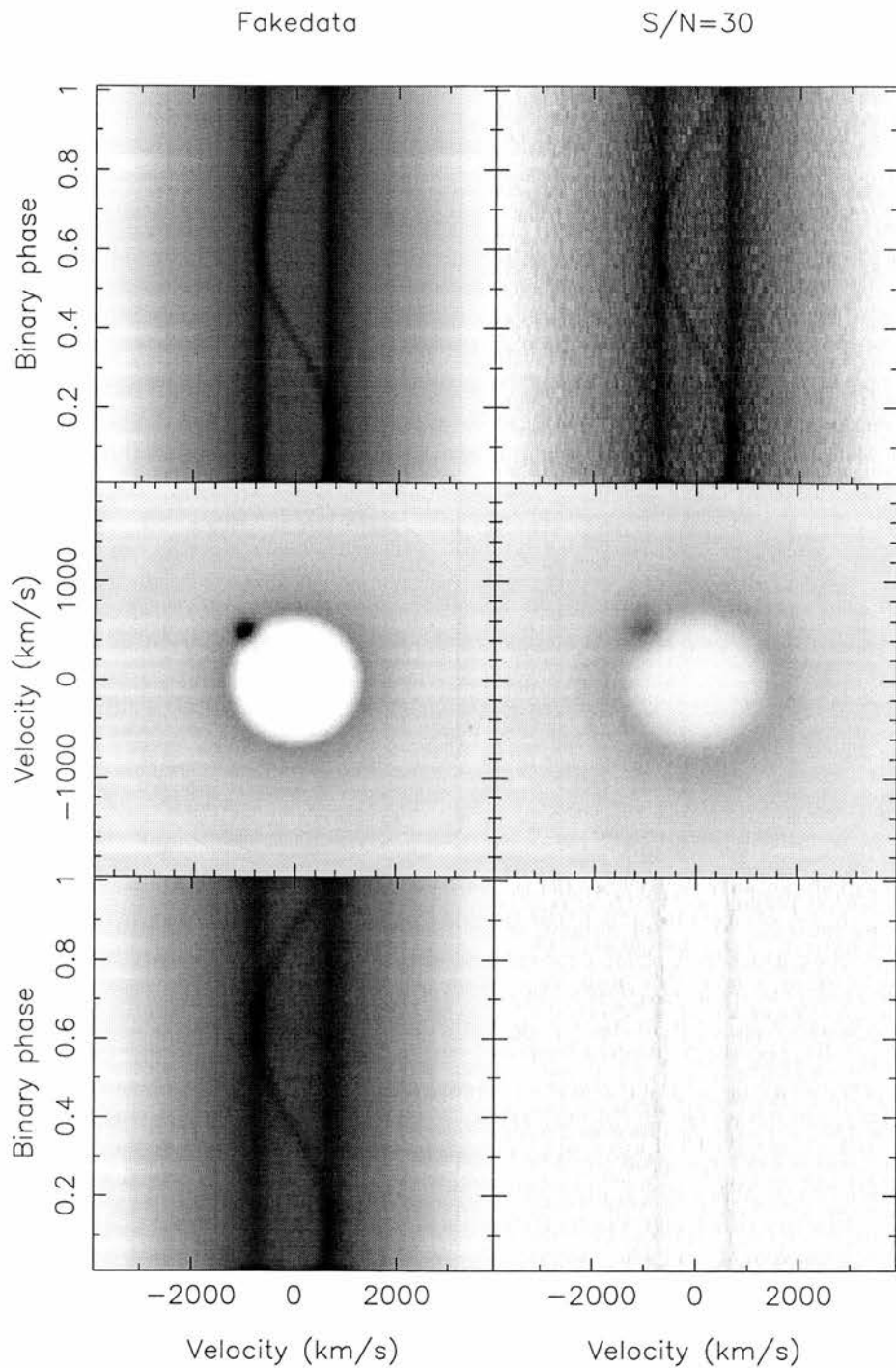


Figure 2.4: A maximum entropy reconstruction. The data in the top left panel is calculated from a model disc carrying a hot spot. The model in Doppler coordinates is plotted in the middle panel on the left. Random noise was added to the data (top, right) and the tomogram was reconstructed from this noisy data (middle, right). The predicted data corresponding to this map (bottom, left) shows an excellent fit to the data with only small residuals (bottom, right).

that are corotating in the binary frame over a time scale of at least an orbital period, and any modulation in the intensity as a function of the orbital phase is averaged out.

Marsh et al. (1990) presented Doppler tomograms of U Gem, displaying a symmetric accretion disc and a strong bright spot. The velocity of the gas was between the ballistic stream and that of the disc at the impact site. However, in IP Pegasi the gas follows the ballistic trajectory closely during quiescence, with no evidence for a bright spot in outburst (Marsh & Horne 1990). Red star emission is identified in several systems, mostly during outburst. Harlaftis & Marsh (1996) found extended emission from the bright spot as well as Balmer emission from the secondary star of the dwarf nova OY Car in outburst. The radial dependence of the line emissivity is generally close to $\propto R^{-1.5}$, which may indicate a connection with line emission from the chromospheres of active stars (Horne & Saar 1991).

An altogether different geometry is provided in the polars. Here no disc is formed, instead the material falls initially ballistically towards the white dwarf and is then caught by the magnetic field of the primary and funneled onto its poles. The properties of the emission lines can change dramatically between the low and high states that most of these systems exhibit. Figure 2.5 shows the observed HeII emission line profiles as a function of orbital phase for the eclipsing polar HU Aqr. The Doppler tomograms nicely demonstrate that the gas trajectory is indeed very different in the two states. Theoretical models can then be fitted to reproduce the observed kinematics as derived from the tomograms (Schwope et al. 1997, Heerlein et al. 1999). In QQ Vul, we have used this to model the emission and absorption from the companion star (Schwope et al. 1999b). For an overview of recent results from tomography of polars see Schwope et al. (1998,1999a).

Another example where Doppler tomography provided important insight into the disc dynamics is the application to black hole transients. Marsh, Robinson & Wood (1994) revealed a compact bright spot at the outer disc in the transient source A0620-00. Harlaftis et al. (1996,1997) used phase resolved spectroscopy obtained with the 10m Keck I telescope to image the accretion disc in the transients GS 2000+25 and Nov Oph 1977 during quiescence. The presence of bright spot emission in quiescence demonstrates that mass transfer continues many years after the outburst.

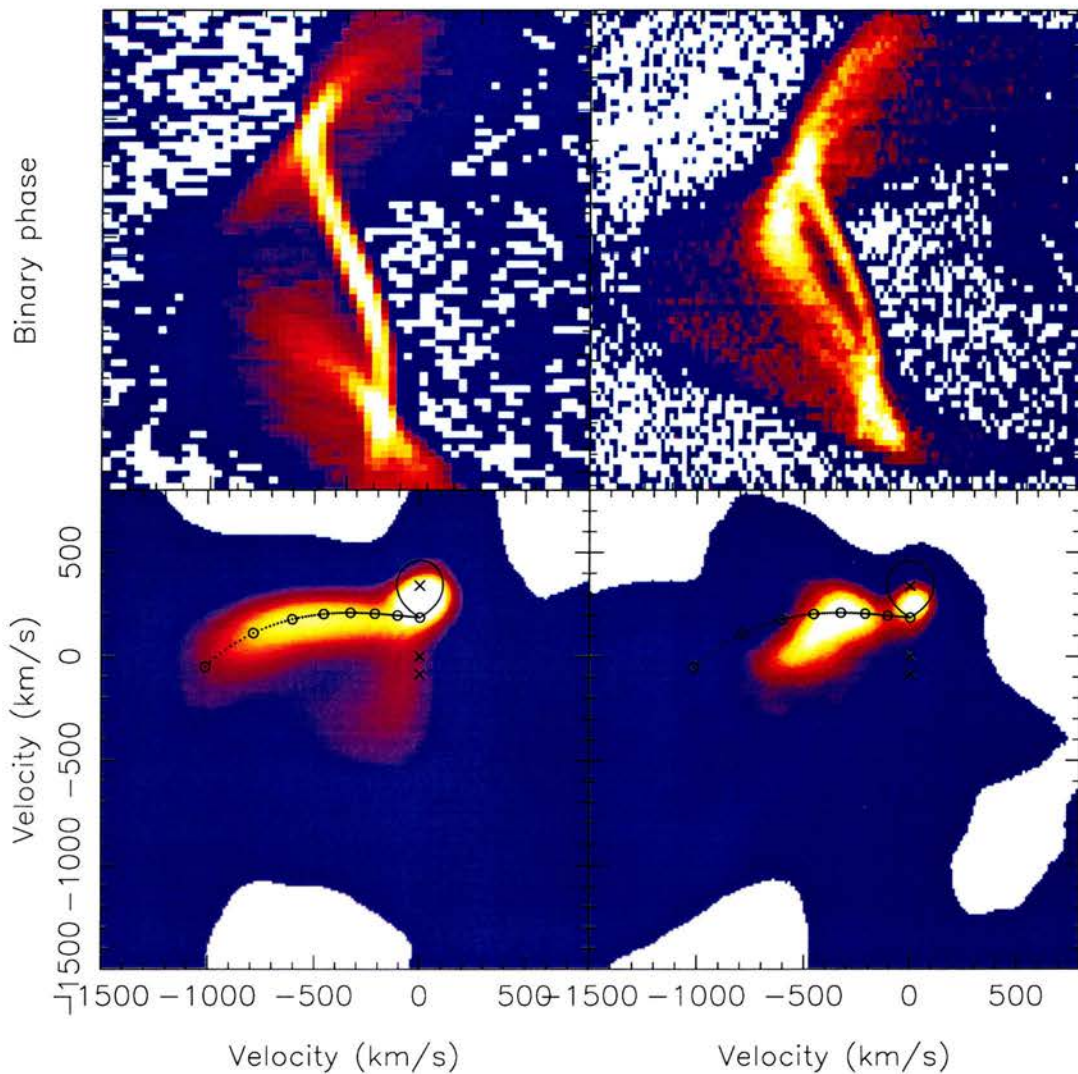


Figure 2.5: *Doppler tomography of the polar HU Aqr at two epochs. Top the observed line profiles of the HeII 4686 emission lines during a high state (left) and a low brightness state. The tomograms for both epochs demonstrate how the infalling gas enters the magnetosphere of the white dwarf. In the high state, a large mass transfer rate ensures that the gas can maintain a near ballistic trajectory down to $0.4R_{L_1}$ before magnetic forces take over. During the low mass transfer stage, magnetic forces control the flow to much larger radii due to the much lower ram pressure of the infalling gas.*

2.3 Echo tomography

The third indirect imaging method is based on the time delays that occur between emission from various regions in the system of interest due to the finite velocity of light.

In its 1D form, echo mapping attempts to reconstruct the transfer function $\Phi(\tau)$, that maps one light curve into another;

$$L(t) = \int \Phi(\tau)C(t - \tau)d\tau \quad (2.7)$$

For example the driving light curve $C(t)$ can be the continuum emission, and the delayed light curve $L(\tau)$ the line emission in response to it. Alternatively the two light curves can span two wavelength regions where, for example, an X-ray light curve is convolved with a transfer function to derive the optical light curve that is the result of photo-ionisation of the X-rays. Echo mapping has been very successfully applied to Active Galactic Nuclei, where time delays span several days (see Horne 1994 for a review). A two dimensional generalisation even allows the mapping of velocity-delay maps in order to probe the kinematic structure of the broad-line regions (Welsh & Horne 1991, Goad, O'Brien & Gondhalekar 1993).

Very recently, with the availability of high time resolution data sets, this technique has been applied to the much smaller X-ray binaries where time delays are only of the order of seconds. The strong X-ray source in the center triggers optical emission at various radii in the disc and on the surface of the companion star, each with their own time delay. The shape of the transfer function can then be fitted with a binary model in order to establish the geometry of the binary system (O'Brien 2000).

CHAPTER 3

The dwarf nova IP Pegasi

In this chapter I will present an overview of the observational evidence for a highly variable disc structure in the eclipsing dwarf nova IP Pegasi. Prominent spiral arms appear during outburst in the emission line images. Part of the outburst observations have been published in Steeghs, Harlaftis & Horne (1997,1998) and Harlaftis, Steeghs, Horne, Martin & Magazzu (1999).

3.1 An eclipsing dwarf nova above the period gap

IP Pegasi is an eclipsing dwarf novae and turns out to be a particularly promising laboratory for our understanding of accretion discs. Despite its brightness of $V=12$ in outburst, it was discovered only in 1981 by Lipovetskij & Stepanyan (Lipovetskij & Stepanyan 1981), and classified by Goranskij, Lyutyj & Shugarov (1985) as a U Gem dwarf nova. It has since been studied in detail both by analysing the eclipse using photometry as well as phase resolved spectroscopy (Wolf et al. 1998 and references therein). The bright spot produces a prominent hump in the light curves during quiescence, and its ingress/egress phases can be used to measure the radius of the accretion disc (Wood et al. 1989; Wolf et al. 1993). The accretion disc shows strong dynamical evolution during the outburst cycle, changing its radius by 45% and also develops strong asymmetries. Broad double peaked emission lines are observed at optical wavelengths in quiescence as well as outburst (Marsh 1988; Marsh & Horne 1990). The Balmer decrement is much flatter during outburst, but no absorption components from

Table 3.1: *Adopted system parameters and ephemeris.*

Parameter		Reference
conjunction, T_0 (HJD)	2445615.4156	Wolf et al. (1993)
orbital period, P (d)	0.15820616	Wolf et al. (1993)
mass ratio, $q=M_2/M_1$	$0.49 \pm .08$	Wood et al. (1989)
radial velocity, K_2 (km s^{-1})	280 ± 2	Wolf et al. (1998)
radial velocity, K_1 (km s^{-1})	137 ± 22	from q and K_2
eclipse width, $\Delta\phi_W$	0.0863	Wood & Crawford (1986)
inclination, i ($^\circ$)	81 ± 1.5	from $\Delta\phi_W$ and q
binary separation, a (R_\odot)	1.33	from i , q , K_2 and P
distance to L1 (R_\odot)	0.77	from q and a
white dwarf mass, M_1 (M_\odot)	1.02	from P , q and a
companion mass, M_2 (M_\odot)	0.50	from P , q and a
companion spectral type	M4	Szkody & Mateo (1986)
distance	130-150 pc	Szkody & Mateo (1986)
mass transfer (g/s) quiescence	$1.4 \pm 0.1 \times 10^{16}$	Marsh (1988)
mass accretion (g/s) outburst	4×10^{17}	Marsh & Horne (1990)
disc radius	$0.25 - 0.37 a$	Wolf et al. (1993), Wood et al. (1989)
	$0.49 - 0.67 R_{L1}$	from bright spot

the disc are visible due to its high inclination of $\sim 81^\circ$. This allows emission line mapping techniques to be applied to this system throughout the outburst cycle. The secondary star is visible in emission, in particular during outburst and an additional low velocity emission component becomes visible during the late outburst (Steehgs et al. 1996). Towards the infrared, the secondary star produces ellipsoidal variations across the orbit (Martin, Jones & Smith 1987). Radial velocity measurements of the narrow absorption components allow an accurate estimate of the radial velocity of the M4 companion star, as long as corrections are applied to allow for non uniform absorption across the surface (Wolf et al. 1998). Rutten & Dhillon (1996) resolved the Na absorption across the Roche lobe surface, allowing a reliable measurement of the true center of mass of the secondary.

In Table 3.1 I have collected relevant system parameters derived for this system. Of

considerable importance is the orbital ephemeris needed to calculate orbital phases for the observations. Since IP Pegasi is an eclipsing system, the orbital period can be measured reliably and accurately where mid-eclipse defines orbital phase 0. Its 3.8 hour period puts IP Pegasi above the period gap, consistent with its U Gem-type outburst behavior. It has been noted though by Wood et al. (1989) and Wolf et al. (1993) that the times of mid eclipse do not strictly follow a linear ephemeris, with a deviation of up to 95s compared to the ephemeris in Table 3.1. I will nevertheless use the linear ephemeris from now on, and note a small uncertainty in the phasing ($\sigma(\phi_0) = \pm 0.007$) may exist when comparing observations at various epochs.

The other important parameter that sets the geometry of the system is the mass ratio $q = M_2/M_1$. Marsh (1988) determined a mass ratio from radial velocity measurements of the emission lines from the accretion disc around the white dwarf. This method measures the velocity curves of the emission lines, which in principle have the amplitude of the radial velocity of the white dwarf (K_1). Together with a measurement of the radial velocity of the companion star (K_2) using absorption lines, this resulted in a mass ratio of $q = M_2/M_1 = K_1/K_2 = 0.58$. Hessman (1989) on the other hand determined $q = 0.44$ using a similar method during late decline after an outburst. If the emission line distribution is asymmetric, the motion of its centre will not coincide with that of the white dwarf. This is a common problem with determinations of the primary radial velocity curve, and significant variations occur in the apparent radial velocity over time. Using broadband light curves of many eclipses, Wood & Crawford (1986) measured the white dwarf ingress¹ and egress phases and determined a value of $q = 0.49$ and an eclipse width $\Delta\phi = 0.0863$. More recently, when fitting to a sequence of eclipse light curves, Webb & et al. (1999) also note that $q = 0.49$ allows much better fits to the light curves than the higher mass ratio value of $q = 0.58$. Since the latter value is determined from an emission line velocity, I prefer the ‘photometric’ value of $q = 0.49$, and calculate the radial velocity of the white dwarf (K_1) from q and the well defined secondary star radial velocity K_2 . Various other system parameters can then be derived from these fundamental parameters. The eclipse width $\Delta\Phi$ and q provide the orbital inclination i using the Roche geometry. Using Kepler’s law one can then calculate the binary separation a from i, q, K_2 and P since $a = \frac{(1+q)K_2}{2\pi \sin i} P$. The 16% uncertainty in q unfortunately hampers

¹This was severely hampered by the bright spot ingress occurring at the same phase.

a robust determination of the absolute geometry of IP Peg. From a one then calculates the distance to the L1 point using $R_{L_1}/a = (1.0015 + q^{0.4056})^{-1}$ (Warner 1995). Finally, by again using Kepler's third law in its more conventional form we can calculate M_1 and M_2 from P, q and a , where $P^2 = \frac{4\pi^2 a^3}{G(M_1 + M_2)}$.

3.2 The observations

Table 3.2: *Journal of spectroscopic observations*

#	telescope	date	UT interval	Phase interval	spectra	cenwave	disp	state
1	INT	20/07/93	03:49-05:31	0.38-0.78	6	6500	22	q
2	INT	28/07/93	03:50-05:24	0.91-1.32	8	6500	22	q
3	INT	19/08/93	01:11-03:09	0.28-0.80	15	6500	36	o
4	WHT	27/08/93	00:23-04:06	0.32-1.30	68	6500	17	o
5	INT	21/10/93	00:50-02:53	0.40-0.94	15	6500	36	q
6	INT	27/11/94	23:17-01:06	0.96-1.44	15	6500	36	q
7	INT	28/12/94	19:35-21:30	0.91-1.42	16	6500	36	q
8	INT	29/11/96	19:15-22:54	0.09-1.05	81	4500	25	o

Details of the observations for the 8 epochs. The column phase interval denotes the range of orbital phases covered, spectra the number of spectra obtained, cenwave the approximate central wavelength of the spectra, disp the dispersion in km/s and state is either quiescence (q) or outburst (o).

We obtained phase resolved spectroscopy of IP Pegasi during 1993-1996 using the 2.5m INT and 4.2m WHT telescopes operated by the Isaac Newton Group on La Palma. Table 3.2 details the observations. Most INT observations were obtained through service time which limits the observing window to 2 hours, providing limited orbital coverage. For comparison an AAVSO/VSNET² light curve is plotted in Figure 3.1 with our spectroscopy runs marked as vertical arrows. It shows the semi periodic outbursts when IP Pegasi reaches $V \sim 12$ compared to $V \sim 15$ in quiescence. I combined the total AAVSO and VSNET databases on IP Pegasi, ²AAVSO and VSNET are international networks of amateur variable star observers providing systematic visual magnitude estimates for many variable stars. See <http://www.aavso.org/> and <http://www.kusastro.kyoto-u.ac.jp/vsnet/> for more information.

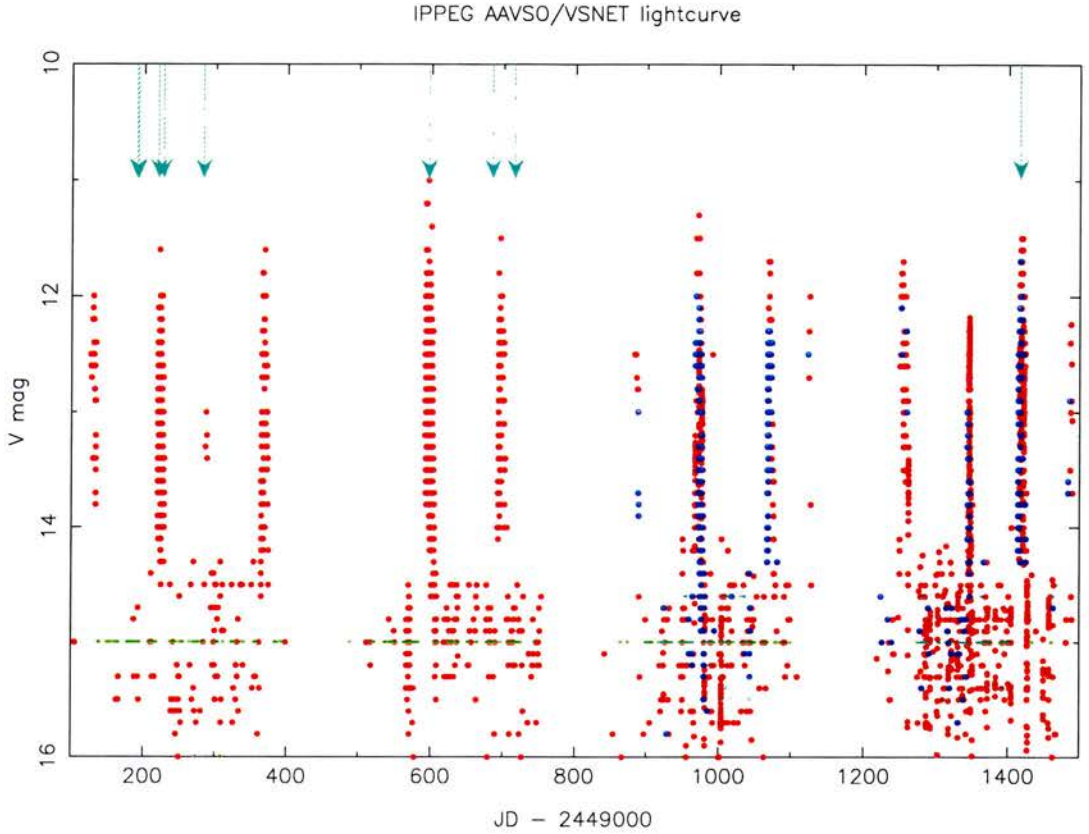


Figure 3.1: *Visual magnitude estimates from the AAVSO (red) and VSNET (blue) databases between 1993 and 1997. The green points denote upper limits to the V magnitude. Our spectroscopic observations are marked by the arrows; the dashed arrow denotes the spectroscopic study by Morales-Rueda, Marsh & Billington (1999).*

covering 14 years, in order to derive some of its outburst properties. I visually measured the start, peak, start of decline and end of all outburst that were sufficiently covered by amateur observers. Figure 3.2 plots the measured values together with histograms of the 30 outbursts that were measured. The mean outburst recurrence time is 88 days with a considerable RMS of 18 days. The mean outburst duration is 13 days with an RMS of 2 days. Rise to outburst lasts 2.0 days on average with an RMS of 0.4 days. IP Pegasi spends around 15% of its time in outburst and there is no evidence from the available observations for a correlation between the interval between outbursts and the outburst duration. All IP Pegasi outbursts therefore seem to fall into the same category.

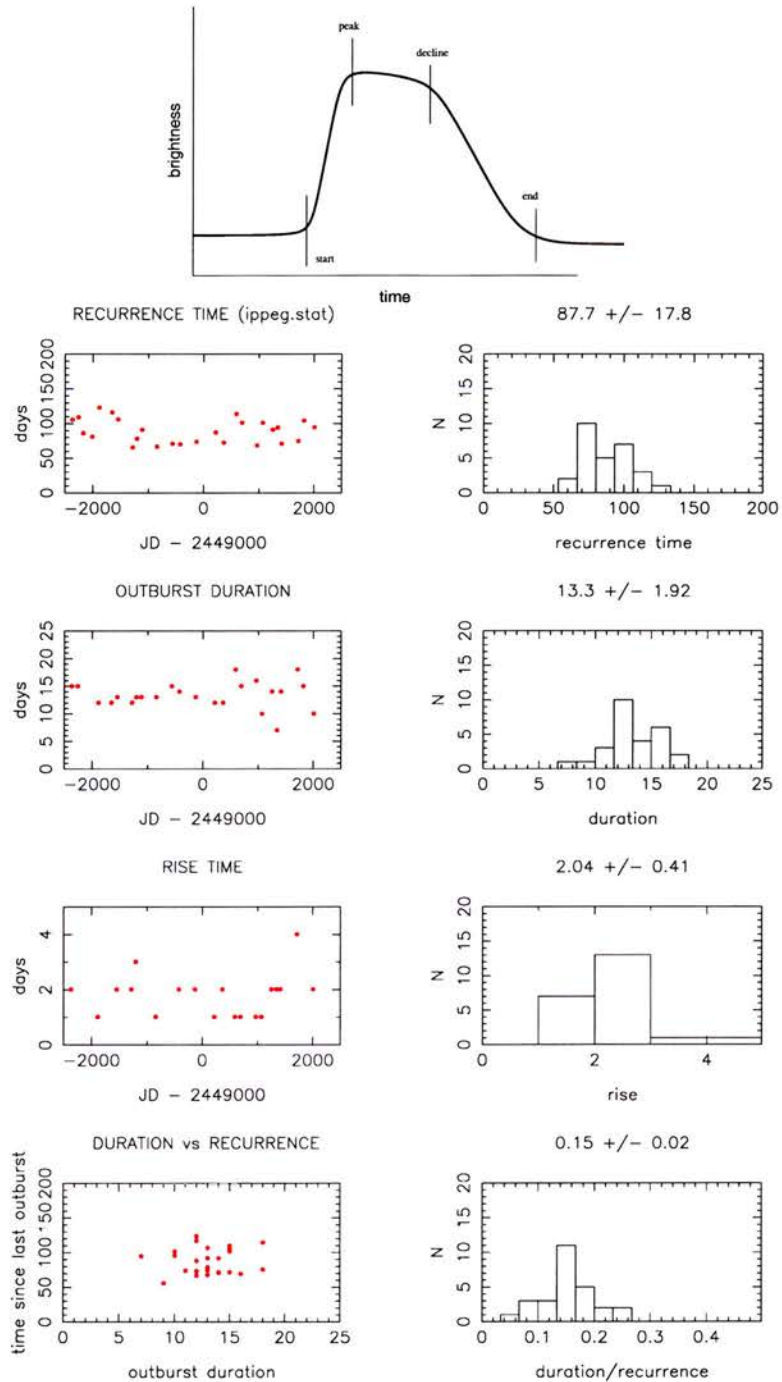


Figure 3.2: *The outburst properties of IP Pegasi. Top panel shows a typical outburst profile together with the start, end of rise, start of decline and end of the outburst marked by vertical lines. 30 outbursts were measured in this way in order to derive mean outburst properties. The left-hand panels show the individual measurements, and on the right the data is displayed in histogram format. From top to bottom are plotted; recurrence time (time between start of current and previous outburst), total outburst duration (end-start), rise time and outburst duration versus recurrence time.*

3.3 Data reduction

All spectroscopic data were obtained using long slit spectrographs equipped with CCD detectors; the intermediate dispersion spectrograph (IDS) on the INT and the dual beam ISIS on the WHT. Tungsten exposures served to construct a pixel-to-pixel flat field correction after the bias level was subtracted using the overscan regions. Arc spectra were regularly recorded for wavelength calibration and a flux standard was observed for flux calibration. The noise characteristics of the CCD chips were determined from Tungsten flat field exposures at various brightness levels together with several bias frames. A noise model consisting of a readout noise component and Poisson noise component was then fitted to the measured RMS scatter as a function of ADU, the data unit in the CCD frames. The readout noise of the chip as well as the conversion factor between ADU and photons could thus be accurately measured. With this noise model I then performed sky subtraction and optimal extraction of the object and comparison star spectrum on each target frame including properly propagated errors for each wavelength. Wide slit exposures of the comparison star and flux standards allowed us to correct each exposure for slit losses. This was achieved by dividing each comparison star spectrum that is observed simultaneously with the object by the wide slit (i.e. photometric) comparison star spectrum at airmass 1. A line was then fitted through this ratio and these fits were then multiplied with the IP Pegasi spectra to correct for wavelength dependent slit losses to first order. An absolute flux scale could thus be made for all our spectra except for the epoch 1 and 4 data, where no comparison star was in the slit³. I estimate that systematic errors introduce no more than 15% error in these fluxes between the various epochs. Polynomial fits to the arc spectra and arc interpolation over time ensured the wavelength scale was accurate to better than 0.1 pixels across the spectrum, and instrumental flexure was accounted for.

In order to calculate Doppler tomograms, the continuum was subtracted using an iterative spline fit to selected continuum regions. The continuum subtracted spectra were then binned onto a constant velocity scale. This binned data served as input for the tomography code. All orbital phases within ± 0.15 of mid-eclipse were masked as the eclipse is not modelled

³The epoch 4 data were obtained in a special observing mode that did not allow the presence of a comparison star on the slit. See Steeghs et al. (1996) for more details

by the code.

3.4 The accretion disc

The accretion disc is expected to vary dramatically across the outburst cycle as it accommodates different mass transfer rates. Marsh & Horne (1990) presented Doppler tomograms of IP Peg both in quiescence as well as outburst. Whereas the quiescent disc showed the classic ring centered on the white dwarf, as well as enhanced emission at the location of the hot spot, the disc in outburst appeared to be severely distorted, as deduced from Doppler tomograms and eclipse analysis. The hump produced by the bright spot is strong during quiescence and not visible during outburst. Bright spot emission is therefore not greatly enhanced during outburst, unlike the accretion disc which is the dominating line and continuum emission source in outburst.

Bobinger et al. (1997) derived the brightness temperature profile of the disc during decline from outburst using eclipse mapping methods. They derived very low brightness temperatures for the inner regions of the disc (7000-9000K), while the outer disc regions systematically cooled down over the course of 4 days. They suggested they were witnessing the cooling front traveling inwards at a rate of ~ 800 m/s. Such very flat temperature profiles have been reported in several high mass transfer rate systems (e.g. Rutten, Van Paradijs & Tinbergen 1992), and either shows that such discs are indeed far from the state we expect if local viscous dissipation is the dominant heating source, or that somehow the inner disc is blocked from view. Indeed if one tries to stick to steady state disc models, Webb et al. (1999) found that the light curves of IP Pegasi in outburst could only be fitted with a very thick flared disc ($\pm 15^\circ$). We are therefore forced to either accept a disc thickness far larger than expected, or accept a temperature-radius law that departs from the steady state viscous model.

In August 1993 we were able to observe IP Pegasi for half an orbit during the early phases of an outburst. The light curves show an increase at the level of 7% across our observations, which can be entirely attributed to the rising flux from the irradiated secondary, as its illuminated front side rotates into view. The system had reached the outburst maximum, and

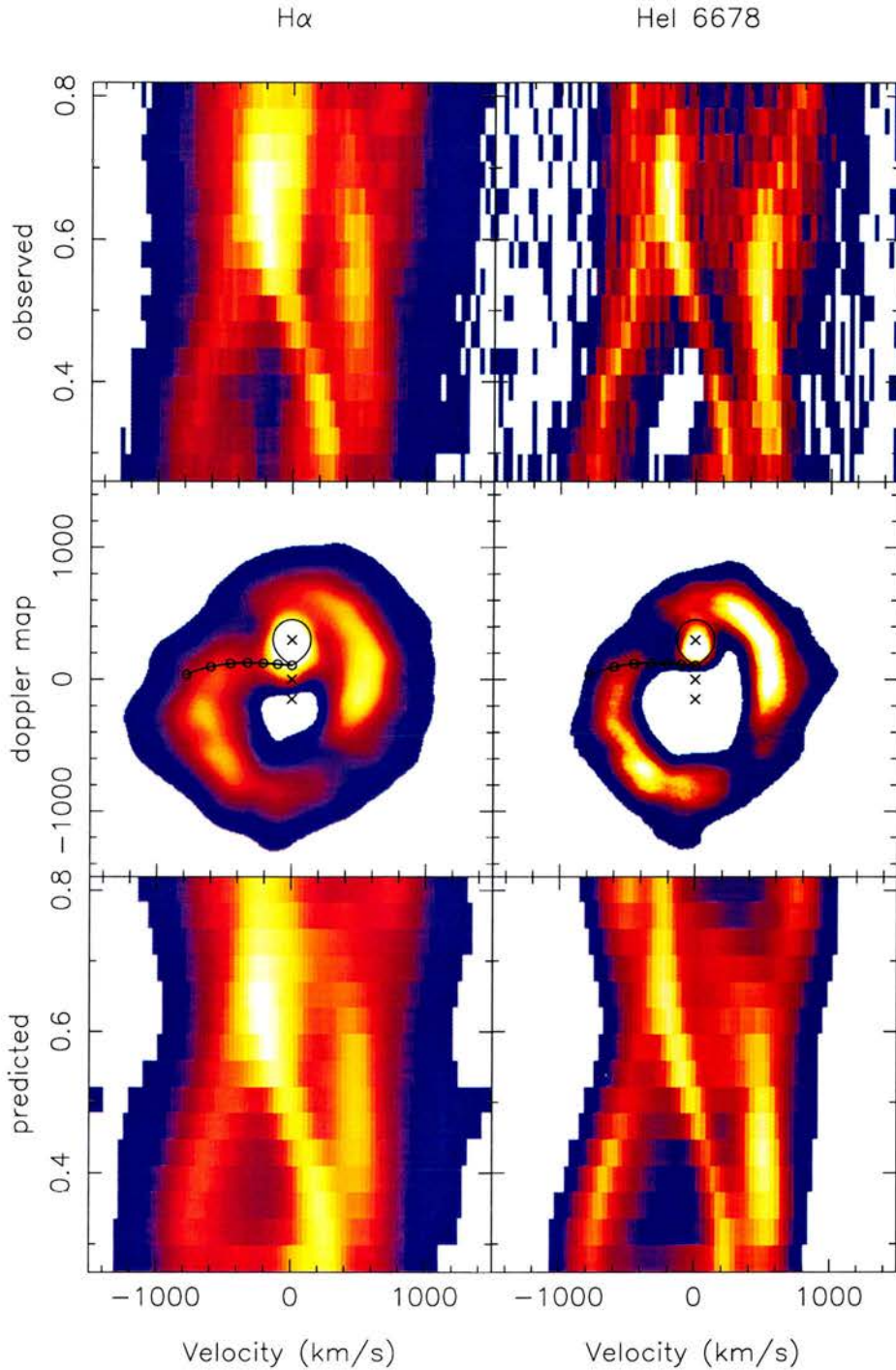


Figure 3.3: Top panels show the observed line flux from IP Pegasi as a function of binary phase with H α on the left and HeI(6678) on the right. Middle panels are constructed Doppler tomograms with theoretical gas stream and Roche lobe plotted for comparison. The bottom cross denotes the white dwarf, middle cross the system center of mass at $V=(0,0)$ and the upper cross represents the radial velocity of the secondary star. Bottom panels show predicted data constructed by projecting the Doppler image at the observed phases in order to determine how well the image fits our data.

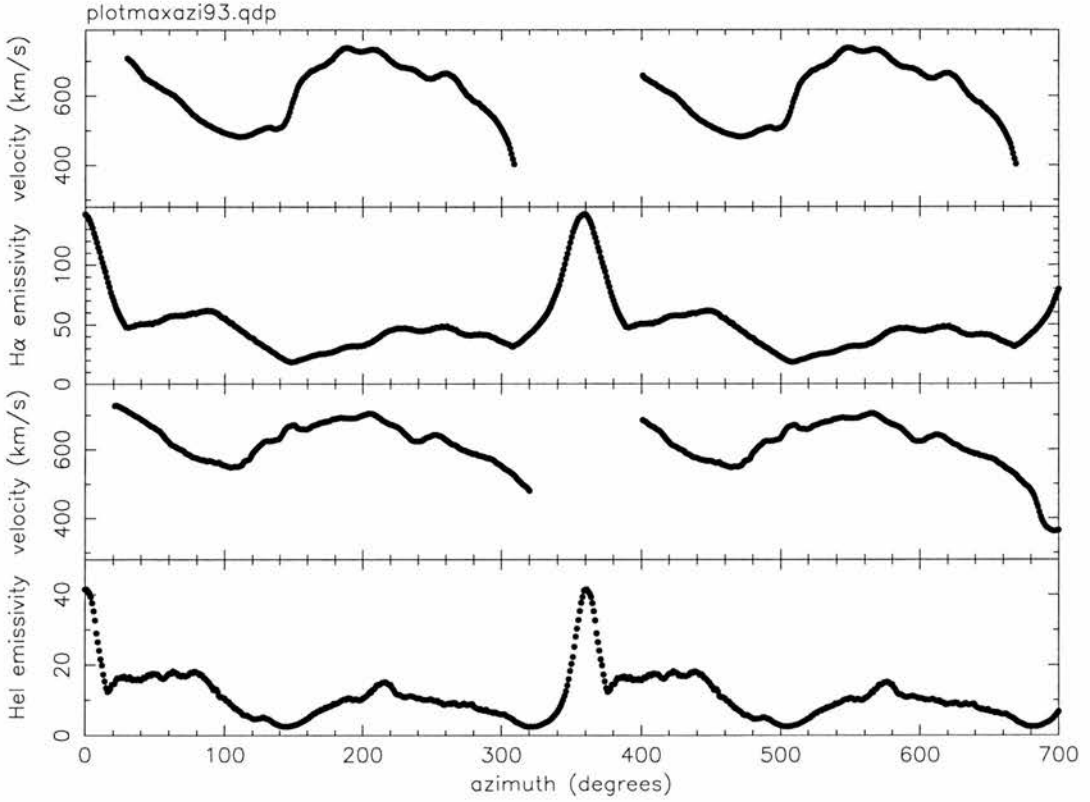


Figure 3.4: *The velocity at which maximum emission in the tomogram occurs along a radial slice as a function of azimuth. Top for $H\alpha$, followed by the intensity of the tomogram at that position. Bottom two panels are the same but now for HeI 6678. This nicely traces the two spiral arms as a function of azimuth except around $0^\circ/360^\circ$ when the component of the companion star (at low velocities) dominates.*

rose from a low brightness state in just 1-2 days. The fact that the disc contribution was not significantly changing during our observations, ensures that I can apply Doppler tomography techniques to this data set to recover the properties of the accretion flow in the co-rotating frame. Figure 3.3 shows the observed line profiles as well as Doppler images constructed from the observations for the $H\alpha$ and HeI 6678 profiles.

The disc images display a striking two armed spiral pattern, as opposed to the circular ring expected from an axisymmetric accretion disc around the white dwarf. To quantify the properties of the two spirals in the tomograms, I plot in Figure 3.4 the velocity and line emissivity of the spirals as a function of azimuth. This was achieved by making a radial slice through the image for each azimuth ($0^\circ/360^\circ$ corresponding to the positive V_Y axis and rotating clockwise) and measuring the velocity at which maximum emission was reached as

well as the image value at that maximum. A median filter was first applied with FWHM set to the instrumental resolution to avoid oversampling the image. The line emissivity in the spirals is about a factor of ~ 3 stronger than that of the disc emission outside the spirals in $H\alpha$ and a factor of ~ 5 in HeI 6678, pointing to considerable additional local heating and/or density enhancement. The velocities of the disc material in the two arms decrease from ~ 700 km s^{-1} down to ~ 500 km s^{-1} with increasing azimuth. No evidence for a bright spot is visible, and the spiral structure extends to the azimuth at which the ballistic stream would hit the disc ($\sim 300^\circ$). Such low disc velocities imply a very large disc, indeed larger than the Roche lobe if the velocity field is Keplerian. The arm in the top right of the tomogram (between azimuths 20° and 140°) is stronger compared to the arm near the gas stream covering azimuth 200° - 300° , though I am not able to check if this persists throughout the orbit.

Such a spiral pattern resembles closely the tidal density waves that are thought to be generated by the tidal forces of the companion star (Chapter 1). To confirm whether a two armed spiral can indeed produce the observed line profiles, I constructed a Doppler map of a model disc containing two symmetric trailing spiral arms, as shown in Figure 3.5. This model assumes a two-armed trailing spiral pattern in the spatial line emissivity of the disc, covering the outer part of the disc between 0.4 and $0.9 R_{L_1}$ (Figure 3.5, right). The velocity coordinates conserve its azimuthal shape but translate small radii to large velocities and vice versa, resulting in a model Doppler image with two spirals folded inside-out (Figure 3.5, bottom right). Note that the model was optimised to resemble the velocities of the observed spirals but in no way attempts to fit the observations in detail. The arms span $\sim 110^\circ$ in azimuth, and appear to be very open. The quoted radii corresponding to this are the Kepler orbits that limit the spirals. The predicted line profiles of this model are shown in the top panel and demonstrates a close resemblance to the observed data of Figure 3.3. A key signature is the modulation of the double peak separation as a function of orbital phase. The two peaks measure the radial velocity of material on either side of the disc moving almost directly towards and away from the observer. Their separation would be constant as a function of binary phase for an axisymmetric (Keplerian) disc. Figure 3.6 plots the azimuthal dependence of the model spiral pattern in terms of its position in velocity as a function of azimuth/phase. It nicely demonstrates the double-humped feature that was observed in the IP Pegasi data, though is not a match in detail as this depends on the assumed distribution of

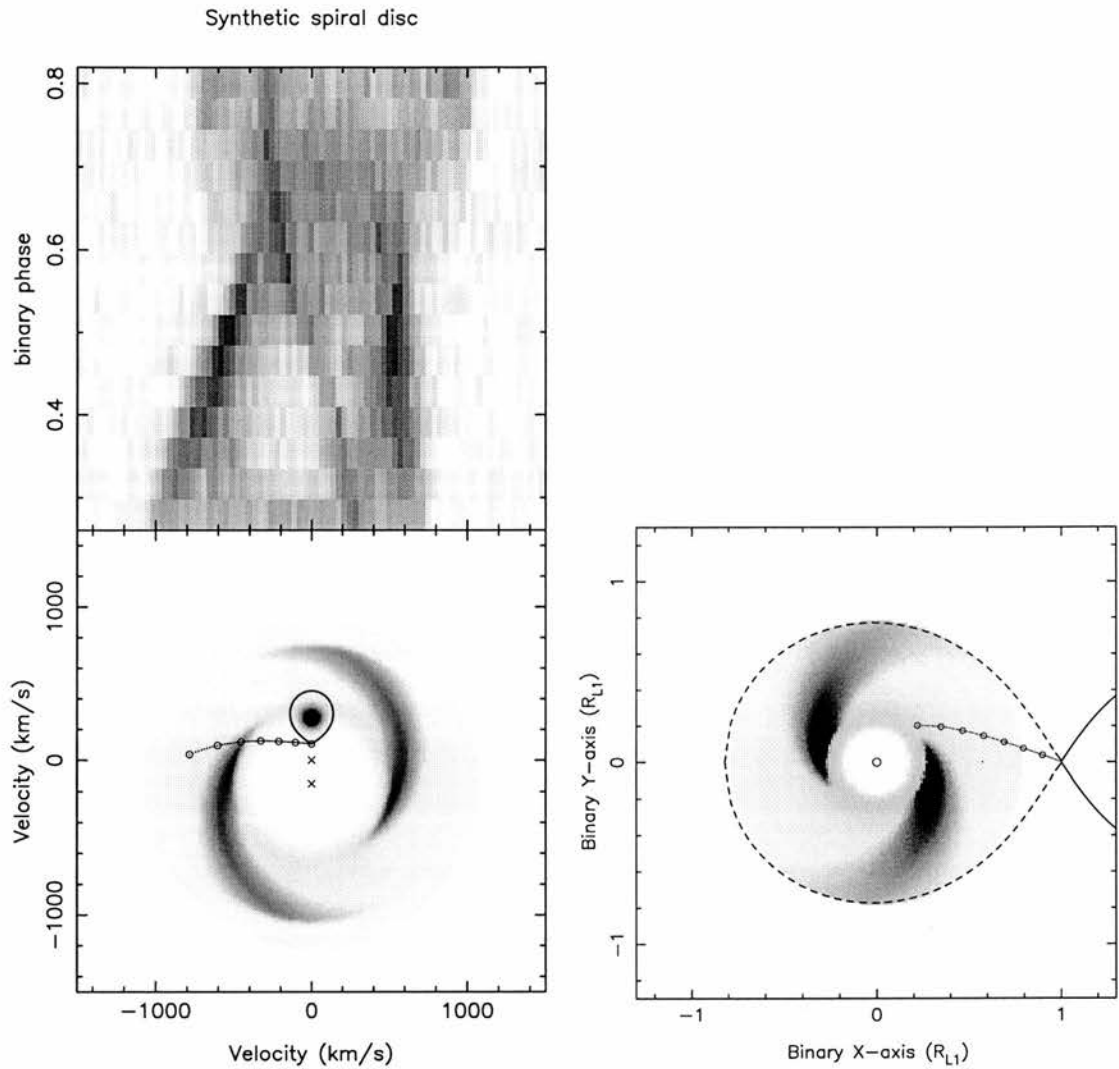


Figure 3.5: *A model Doppler tomogram containing a two armed trailing spiral superposed on symmetric disc emission. A Gaussian spot at the secondary is added to simulate its contribution to the data. The top panel shows the predicted data from such a system with the same signal-to-noise as our observations (compare with the top panels of Figure 3.3). Bottom left panel is the model tomogram and the bottom-right panel shows a spatial image of the disc emissivity pattern.*

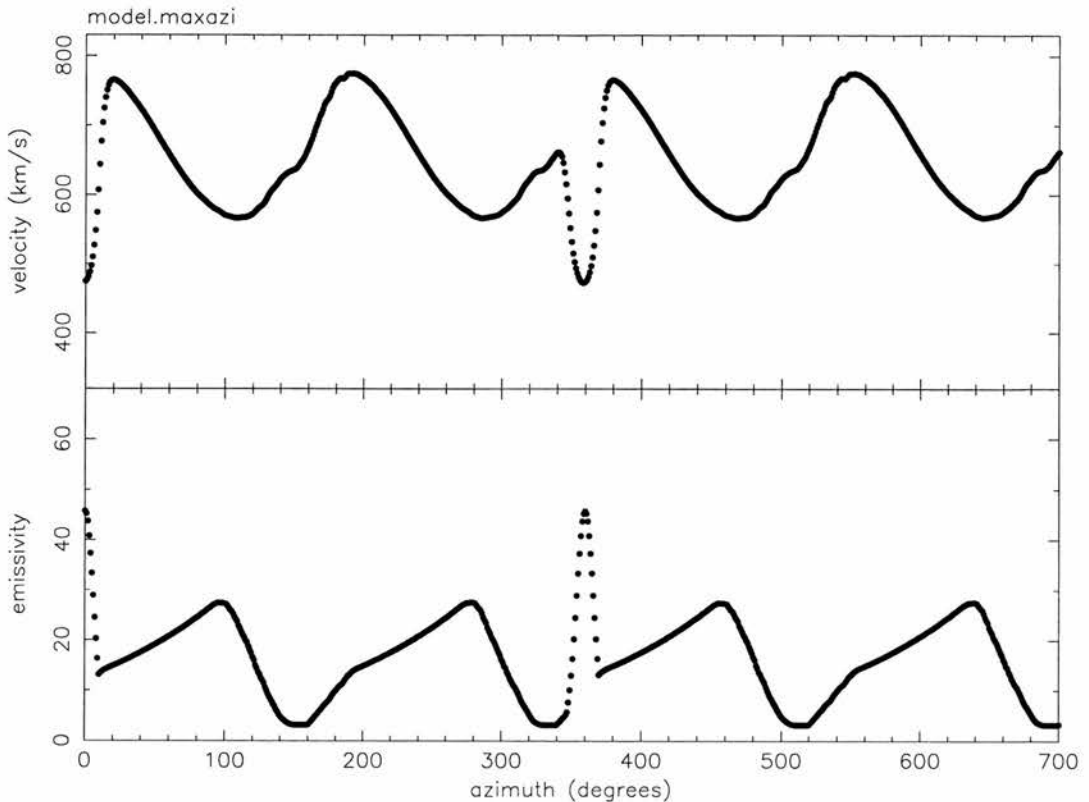


Figure 3.6: *The azimuthal dependence of a two armed spiral pattern produces a periodic variation in their velocity (top) and emissivity across the disc. This can be identified in the IP Pegasi observations in both the line profiles and the disc tomogram (Figure 3.3).*

line emission along the spirals. Note also the jump in the trailed spectrogram around phase 0.7 (azimuth 50°) where one crosses from one arm to the other.

A week later, when the system was still at maximum brightness we observed IP Pegasi on the WHT and although the contribution of the companion star was much stronger, and a curious low velocity component was visible in the $H\alpha$ line, the disc was still dominated by a two armed pattern (Figure 3.7). *This asymmetry is therefore able to persist throughout the outburst.* Again the right arm is stronger, and appears not as extended in azimuth compared to the arm connecting to the gas stream.

Since the Doppler images are a balance between fitting the data and maximising the entropy, the strong secondary star component may bias the disc structure, as it is an important contribution towards the χ^2 statistic used to evaluate the fit. Its strong phase dependence as the irradiated front side of the secondary rotates into view cannot be fit in detail by a

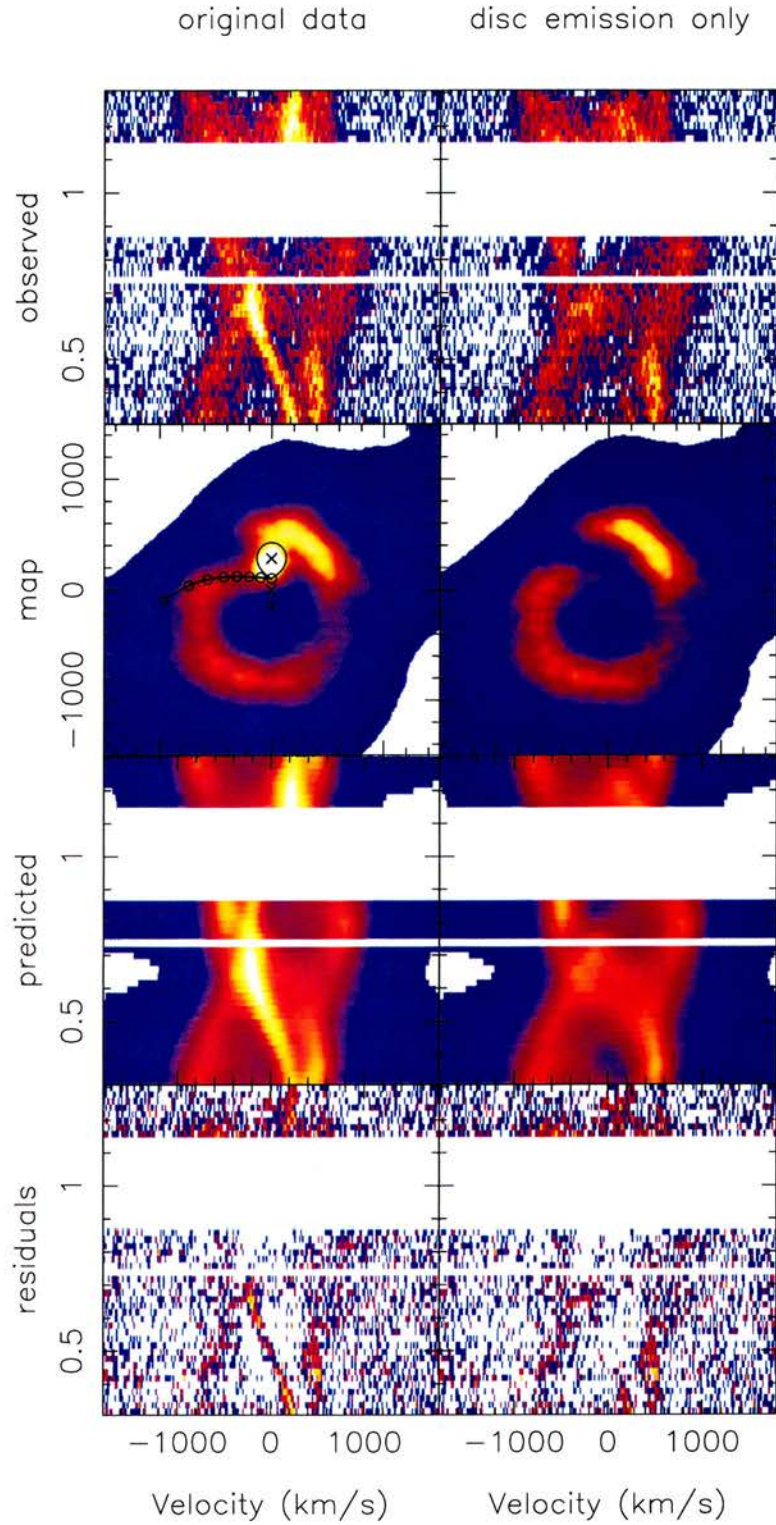


Figure 3.7: *HeI 66678 emission towards the end of the August 1993 outburst. The secondary star contribution has been subtracted to investigate its effect on the reconstructed disc structure. Left the original observed data followed by the tomogram, predicted data and residuals. The right panels show, in the same order, the data with the red star component subtracted (see text for details).*

spot in the Doppler tomogram and so will limit the χ^2 that can be achieved. We therefore attempted to remove the contribution of the companion star and produce an Doppler image of the accretion disc only. I first calculated a Doppler image using the observed emission line profiles (Figure 3.7, left). The regions outside the Roche lobe were then masked off and this masked map, containing only the image values within the Roche lobe, was projected at the original observed orbital phases to produce the phase resolved emission from the companion star. Because of image smoothing, the emission is not strictly confined to the Roche lobe, but fills a slightly larger area. I therefore increased the mask to also include emission up to 10%, in terms of radius, outside the predicted Roche lobe. This secondary star contribution was then subtracted from the data. The resulting line profiles (Figure 3.7, right) were then used to construct a new Doppler image, free from secondary star emission. The spiral pattern is clearly visible and identical to the original image which was a fit to both disc and companion star emission. It shows that the disc structure is reliably reconstructed even if a strong secondary star component is present.

A few months later when the system was back in quiescence we obtained the epoch 5 data. The Doppler image from this data is plotted in Figure 3.8. Phase coverage is very similar to the early outburst data and the disc has changed radically. The open spirals are no longer visible. The disc is however still clearly asymmetric and one can identify enhanced emission on both sides of the white dwarf along the V_x direction. After subtracting the symmetric part of the image, defined as the median of all images values at each radius as measured from the white dwarf, the asymmetric part nicely separates the sites of enhanced emission. I will discuss the secondary star line emission in the next section. There is some excess disc emission between the ballistic velocities of the gas stream trajectory and the corresponding velocities in the disc as it impacts on the outer disc near $R \sim 0.4 - 0.5R_{L1}$. However, the strongest asymmetries appear below the gas stream trajectory and on the opposite side. Marsh & Horne (1990) recover similar asymmetries, however the bright spot in their $H\beta$ tomogram appears to be much stronger. AAVSO observations indicate a brightening of the system roughly 5 days after these observations (Figure 3.1), however the number of magnitude estimates available are too small to allow a comparison of this brightening to the more typical larger amplitude outbursts that IP Pegasi exhibits. As we shall see, the disc is now much smaller than during outburst, so tidal forces are greatly reduced and we would not expect an open spiral pattern

21/10/93 H α

asymmetric part

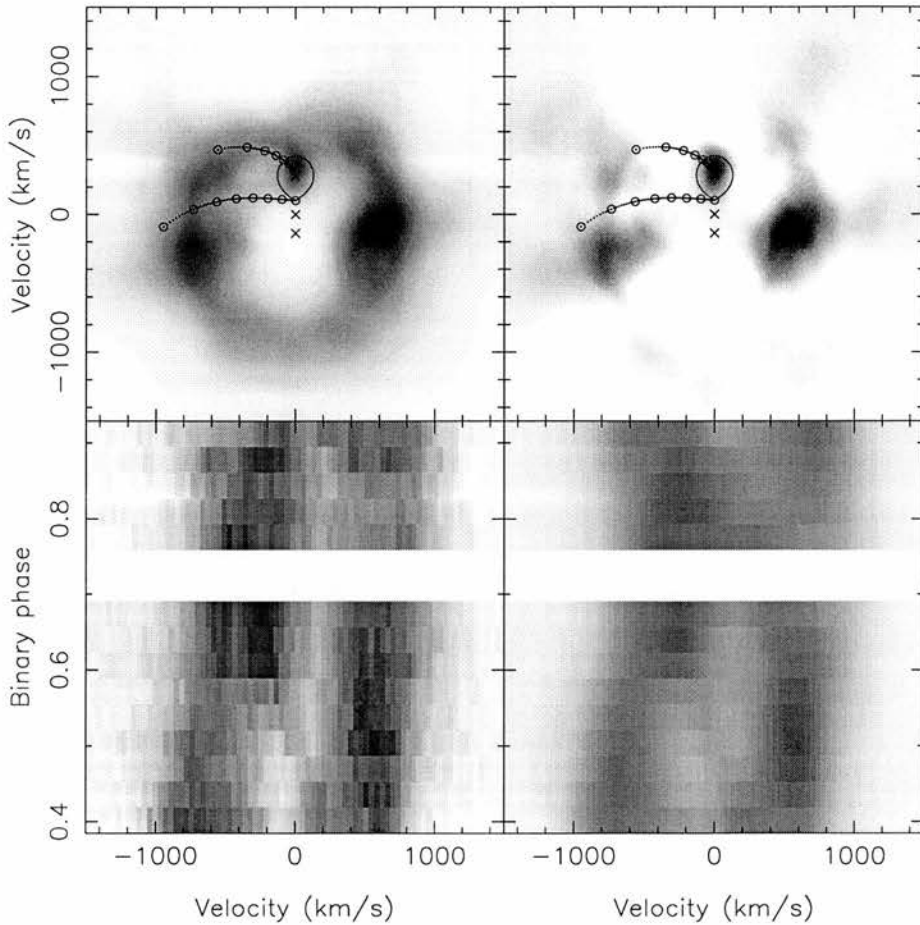


Figure 3.8: *The H α emission on 21st October 1993, two months after the outburst observations. Top left: the H α tomogram constructed from the data in the bottom left. Top right: the asymmetric part of the tomogram. Bottom right: the predicted data.*

like we observe in outburst. Whether more tightly wrapped spiral waves could produce disc asymmetries in quiescence will be explored in Chapter 4.

To confirm that the spiral pattern observed during the 1993 outburst is visible during other outbursts, we obtained a full orbit 2 days into the November 1996 outburst. The region surrounding the HeII 4686 emission line was chosen this time as opposed to H α to see if the spirals are also visible in this high ionisation line. We covered a full orbit including the eclipse, achieving an orbital phase resolution of 0.012 and spectral resolution of 55 km/s at HeII4686. This ensures that artifacts due to restricted phase sampling are avoided, and optimal image structure can be resolved. Figure 3.9 shows 4 spectra derived from averaging all spectra in

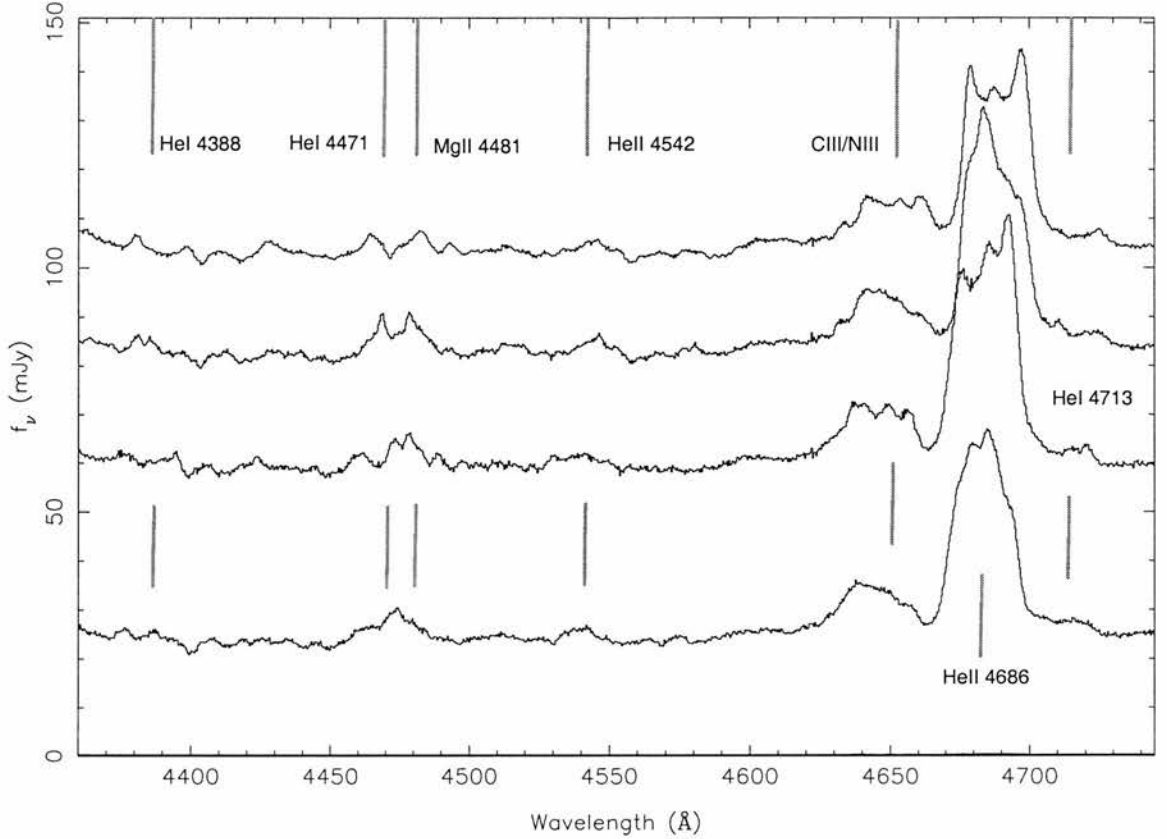


Figure 3.9: *IP Pegasi* on 29/11/1996. Four spectra are shown in the rest frame near phase (from bottom to top) 0.15, 0.4, 0.65 and 0.9. Each spectrum is offset by 25 mJy, and is the weighted average of all spectra within 0.12 of the 4 orbital phases.

4 phase bins across the orbit. Apart from HeII 4686, the strongest line in our wavelength range, there is a strong Bowen blend visible as well as many faint emission lines towards bluer wavelengths. These can be identified as HeI, HeII and MgII transitions, and both disc and secondary star components are present. In the next section I will show that the sharp peaks visible at phase 0.6 can be attributed to the front side of the companion star. Just before eclipse, the double peaks from the outer edge of the disc are visible as well as a low velocity component that fills in the center of the HeII line profile.

Continuum and emission line light curves are presented in Figure 3.10. Significant out-of-eclipse structure is visible as well as a typical broad V-shaped eclipse. Unfortunately we were not able to cover the eclipse egress completely. The phase of mid-eclipse in the emission line light curves is considerably earlier (0.989 ± 0.001) compared to the continuum

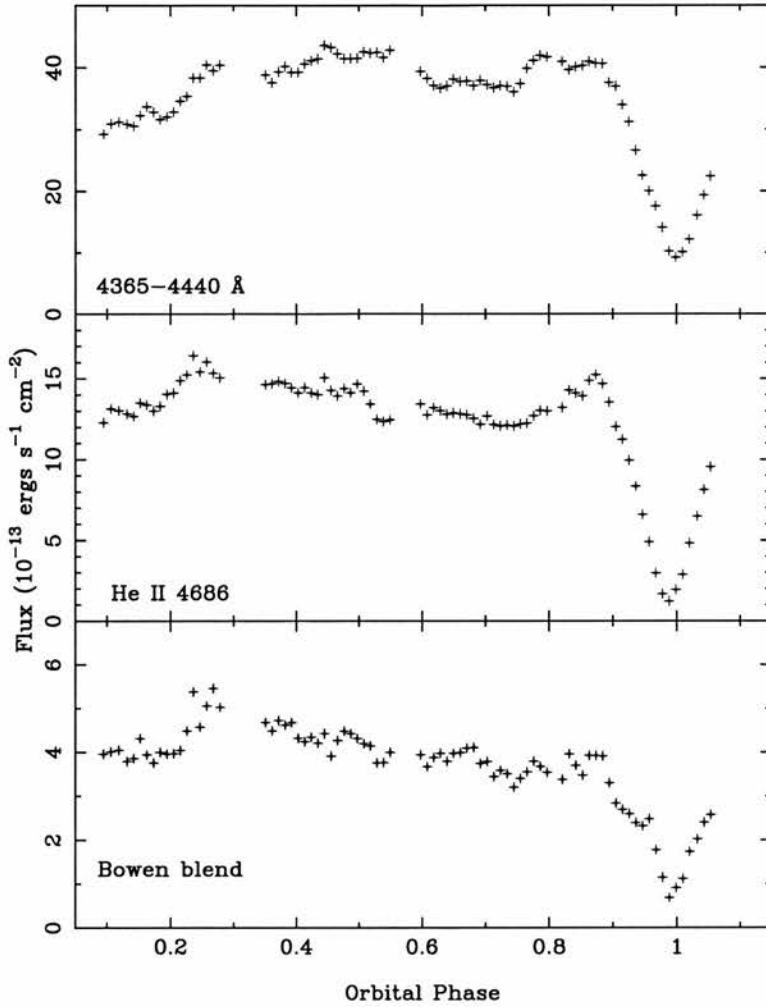


Figure 3.10: *Orbital light curves for the continuum between 4365 and 4440Å, the HeII line and the Bowen blend near 4640Å (all emission within ± 2000 km/s).*

(1.002 ± 0.001), which requires a severe asymmetry in the distribution of line emission across the accretion disc.

If we look at the trailed spectrogram of the HeII line profiles (Figure 3.11), we can identify a narrow component from the secondary star as well as double peaked emission from the disc. Note the radical variation of the double peak separations across the orbit, like we saw earlier in the 1993 outburst data. At some phases, a narrow low velocity component can be traced as well, reminiscent of the low velocity emission in H α (Steeghs et al. 1996). During eclipse, the rotational disturbance due to the eclipse of gas orbiting a white dwarf in a prograde direction is evident. I constructed light curves around primary eclipse for each velocity bin covering ± 1500 km/s in 50 km/s bins. For each of these light curves I measured

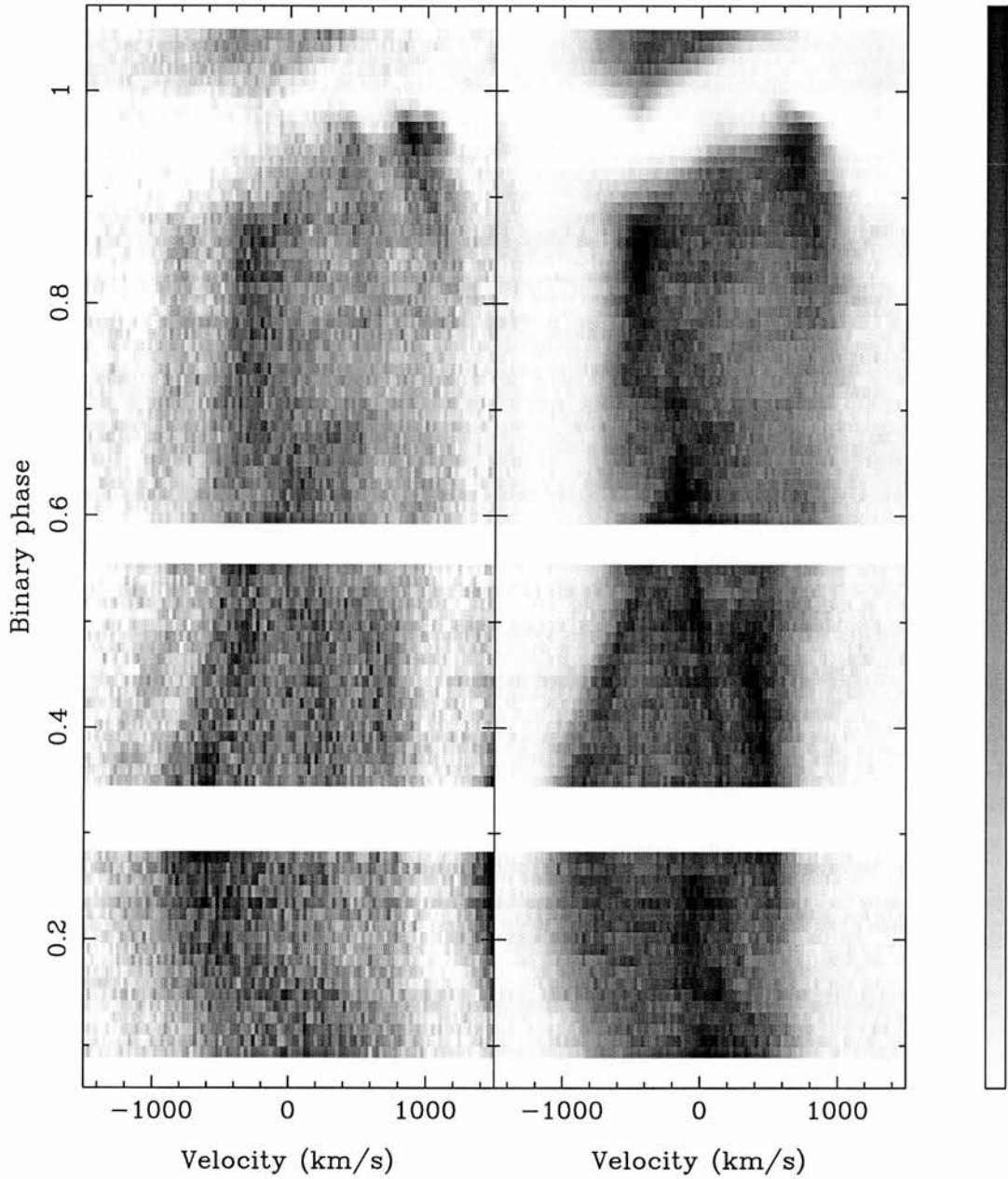


Figure 3.11: *The trailed spectrogram of the Bowen blend (left) compared to the HeII4686 emission. The eclipse shapes clearly show the prograde rotation in the disc, with the blue shifted side being eclipsed before the red shifted side.*

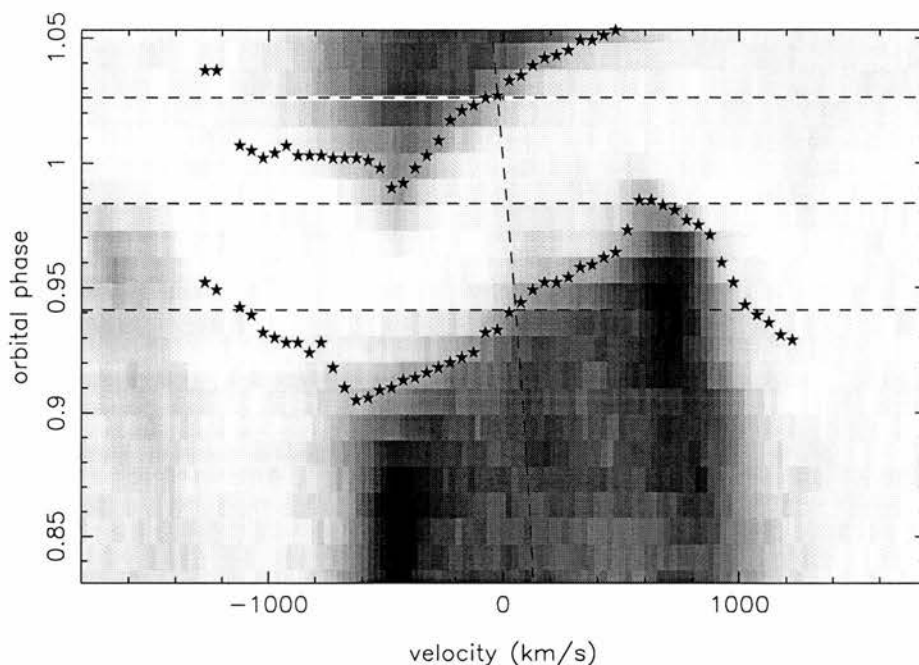


Figure 3.12: Measurements of the phases of half depth across the HeII eclipse are denoted by asterisks. Horizontal dashed lines are the average post eclipse half depth (top), the pre-eclipse half-depth (bottom), and the average mid eclipse phase. The vertical dashed curve denotes the velocity of the white dwarf.

the half depth phases (Figure 3.12). The pairs of measurements were averaged (if both ingress and egress could be measured) to measure the average eclipse width of the He II rotational disturbance giving $\Delta\phi = 0.0851 \pm 0.008$ compatible with the $\Delta\phi_{wd}=0.0863$ measured by Wood & Crawford (1986). On average, half depth was reached at phase $\phi_{1/2} = 0.941 \pm 0.008$, well before the white dwarf ingress at $\phi = 0.957$. A considerable fraction of the HeII emission is therefore coming from the outer regions of the disc, rather than its center.

The Bowen blend near 4640\AA consists of many CII/NIII and OIII components and is a blend typically found in the magnetic polars (e.g. Schachter et al. 1991). It appears from Figure 3.11 that only two components are contributing to the line flux on IP Pegasi, sharing the same features as the HeII emission. By back-projecting these line profiles at the various expected rest wavelengths of the Bowen components onto a $V_x V_y$ plane, I identified these two to be CIII $\lambda 4694$ and NIII $\lambda 4641$.

The He II Doppler image displays the locations of the various emission components; the inner face of the red star, a low-velocity component and the dominant accretion disc

He II 4686

Doppler image

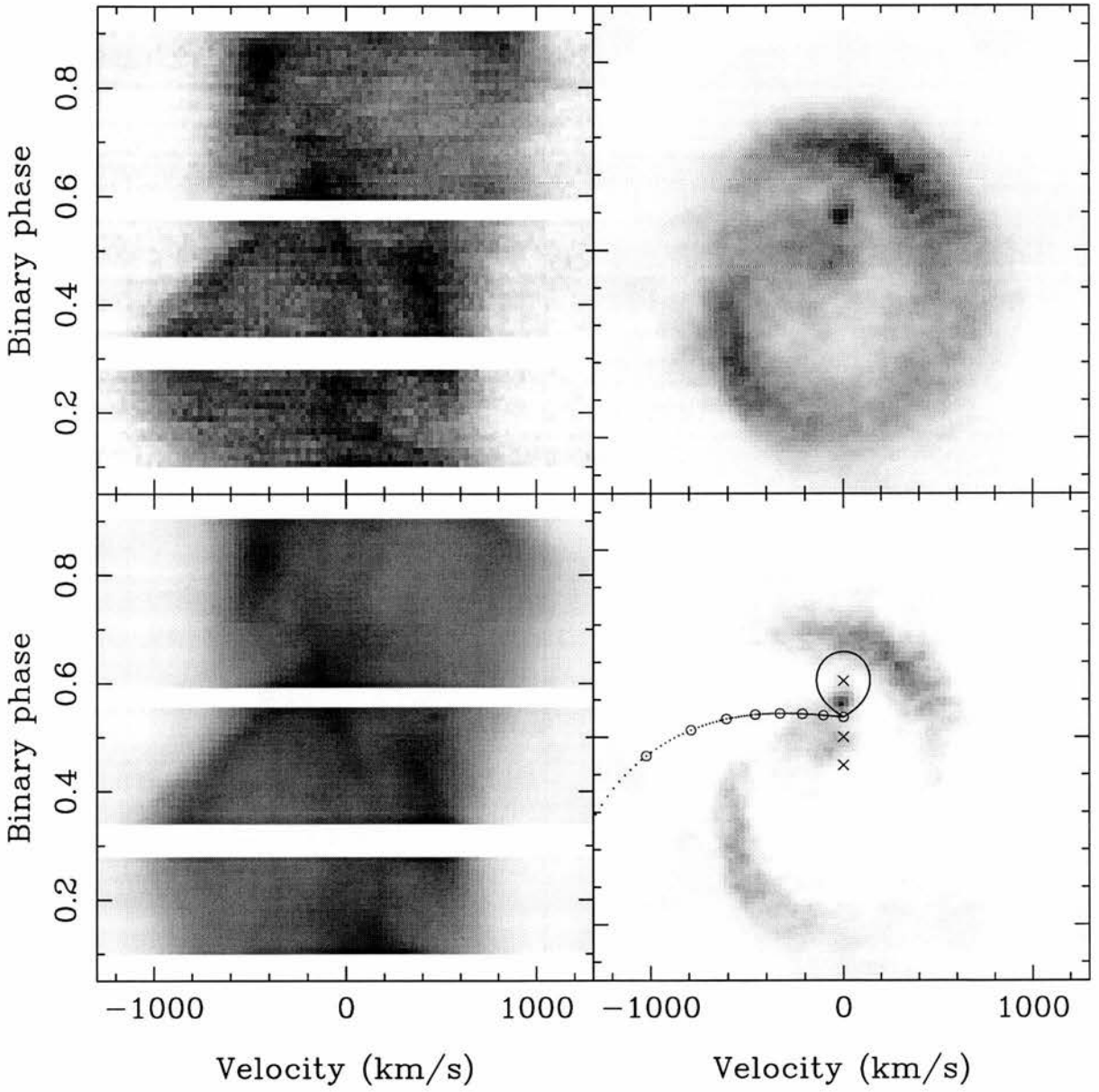


Figure 3.13: *The HeII λ 686 Doppler tomogram (top right) calculated from the observed out of eclipse line profiles (top left), its asymmetric part (bottom right) and the predicted data.*

with its extended spiral arms (Figure 3.13). The low-velocity component is centered at $(V_x, V_y) = (-100 \pm 50, -20 \pm 70)$ km s⁻¹ and has a FWHM of 270 km s⁻¹. The non axisymmetric part is calculated by subtracting the median, calculated along circles centered on the white dwarf, at each radius, to bring out the prominent spirals from the background disc emission. The spiral pattern initially discovered in the early August 1993 observations is again recovered here in the light of HeII. The two arms are very similar to the arms observed in 1993, with the same asymmetry between the two arms; the top right arm being stronger. The positioning in phase again conforms to the azimuths where tidally driven spiral arms are expected. The fact that this structure is now observed in the same position in the co-rotating frame during several epochs furthermore supports a tidal origin.

Unfortunately, phase coverage was not sufficient at all epochs to construct Doppler images without introducing strong artifacts in the image. However one can infer some of the disc properties from the emission line profile shapes. I therefore shifted all spectra into the frame of the white dwarf and produced an average spectrum for each epoch, avoiding the profiles near eclipse. The profiles were normalised compared to the continuum using a spline fit to allow a robust comparison between the epochs (Figure 3.14). The H α equivalent width and its formal uncertainty was calculated based on this average out of eclipse line profile and the full width at half maximum was measured using a digital cursor. Read off errors are estimated to be ~ 50 km/s. The velocities of the double peaks were then measured and averaged to give the velocity of disc material near the outer edge, V_{peak} . Assuming Keplerian velocities, the the disc size can be estimated using Kepler's law ; $R_{disc}/a = [(K_1 + K_2)/V_{peak}]^2$. Obviously as the disc becomes large one expects considerable deviations from Keplerian flow in the outer regions where tidal forces perturb the flow. There is another complication that makes the disc radius estimate uncertain during outburst. As can be seen in Figure 3.14, the strong secondary star contribution and low velocity emission fills in the double peaks, making the average line profile single peaked. The peak velocities in this case were measured near eclipse, where the secondary star contribution is small, and the double peak can be measured.

Finally, power laws were fitted to the wings of the profiles. To reduce the error in the fitted coefficients, I averaged the values obtained from the blue and red wings. I selected two velocity regions, from 700 to 1100 km/s (or 0.25-0.61 R_{L1}) and from 1100-1500 km/s

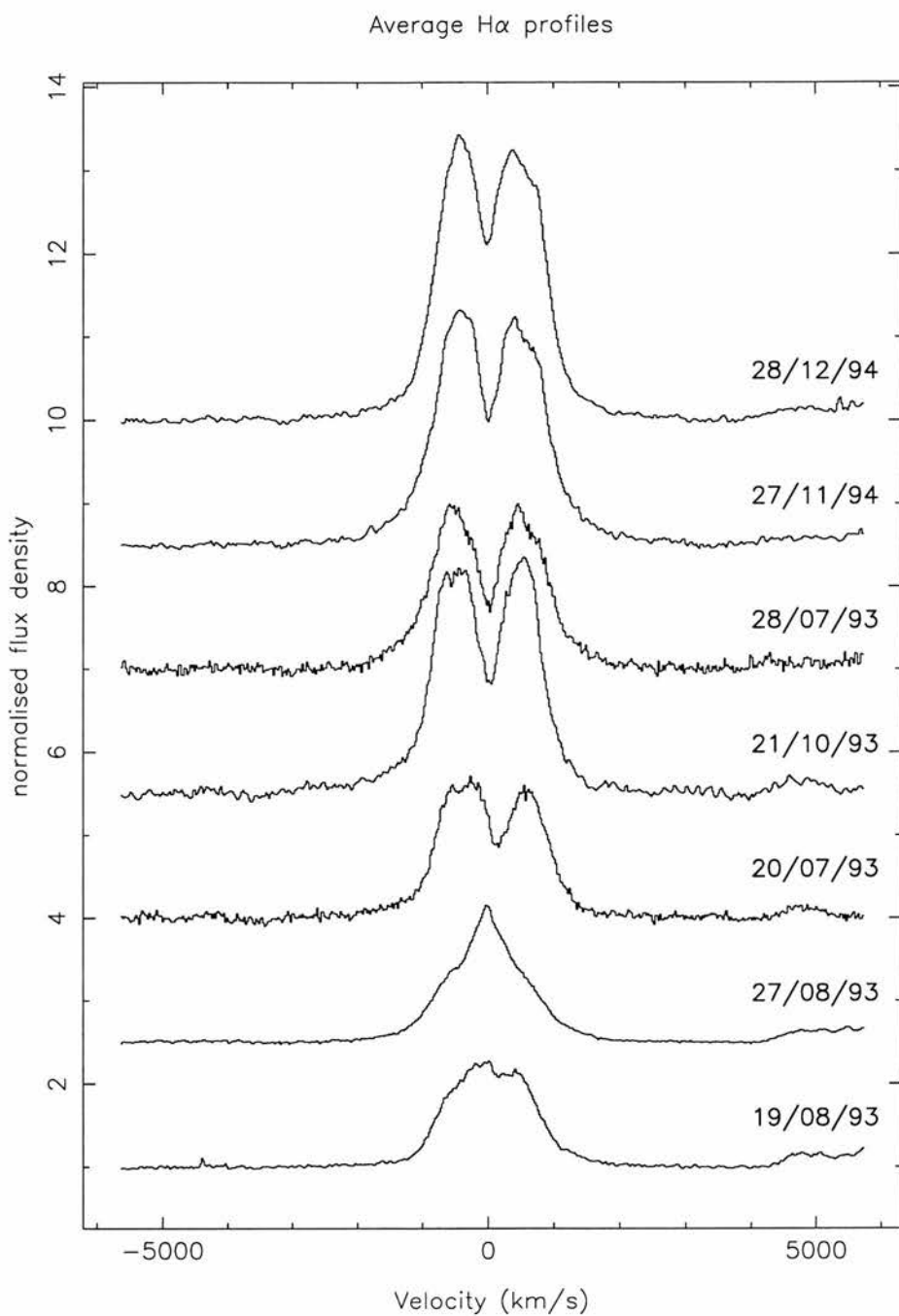


Figure 3.14: *The average out of eclipse H α profile in the frame of the white dwarf. Each is normalised to the continuum using a spline fit. An offset of 1.5 is applied between each epoch, plotted such that line EW is highest at top and decreases monotonically (from top to bottom, epoch 7,6,2,5,1,4 and 3).*

Table 3.3: *Disc properties from the H α profiles*

#	HJD	ΔT	FWHM	EW	V_{peak}	R_{disc}	α_1	α_2	β_1	β_2
		days	km/s	\AA	km/s	R_{L_1}				
1	2449189.71	61 \pm 1	1819	60.01 \pm 0.28	630 \pm 25	0.77 \pm 0.06	2.67	3.90	1.17	0.55
2	2449197.71	68 \pm 1	1871	87.16 \pm 0.43	705 \pm 15	0.59 \pm 0.04	2.14	2.86	1.43	1.07
3	2449219.60	0 \pm 1	1557	43.10 \pm 0.06	515 \pm 25	1.12 \pm 0.08	2.74	2.93	1.13	1.04
4	2449226.60	7 \pm 1	1467	45.8 \pm 0.04	560 \pm 25	0.95 \pm 0.06	2.28	2.97	1.36	1.02
5	2449282.58	63 \pm 1	1749	81.11 \pm 0.40	690 \pm 25	0.65 \pm 0.06	3.13	3.31	0.94	0.85
6	2449684.52	92 \pm 1	1801	138.43 \pm 0.23	680 \pm 40	0.66 \pm 0.11	2.27	3.18	1.37	0.91
7	2449715.37	21 \pm 1	1748	150.55 \pm 0.27	660 \pm 25	0.70 \pm 0.07	2.75	3.84	1.13	0.59

(0.13-0.25 R_{L_1}) and fitted separate power laws of the form $f(v) = A * v^{-\alpha}$ to each section. The split at 1100 km/s was chosen since a single power law does not fit the wings properly. We choose not to fit to velocities larger than 1500 km/s because of low signal to noise in the extreme wings. Again if one assumes the disc velocity field to be Keplerian, the coefficient $\beta = (5 - \alpha)/2$ can be calculated where $j(r) = B * r^{-\beta}$. Table 3.3 lists all derived values. Subscript one denote fits between 700-1100 km/s , subscript two the fits between 1100 and 1500 km/s. ΔT denoted the number of days since the start of the last outburst. Note that the epoch 8 spectra did not cover the H α line so no profile data are listed.

From these figures one can discern a few general trends. The H α EW is smallest at the start of the outburst and increases by a factor of up to 3 in quiescence. However, no strictly systematic growth occurs as a function of time since the last outburst. Considerable EW variations on a short timescale were also noted by Harlaftis et al. (1994). The disc size as estimated from the velocity of the double peaks is plotted in Figure 3.15. It follows the trend established by photometric studies of the disc radius using the bright spot phases; a very large disc during outburst, rapidly shrinking from then on to a much smaller disc in quiescence. The large values in Table 3.3 for the outburst data show that disc velocities are so low in the outer disc, that they can no longer be Keplerian as it would push the disc outside the Roche lobe. Interestingly, the disc is already very large \sim 2 days into the outburst. While an exponential decrease in radius towards the later phases of the outbursts is predicted by

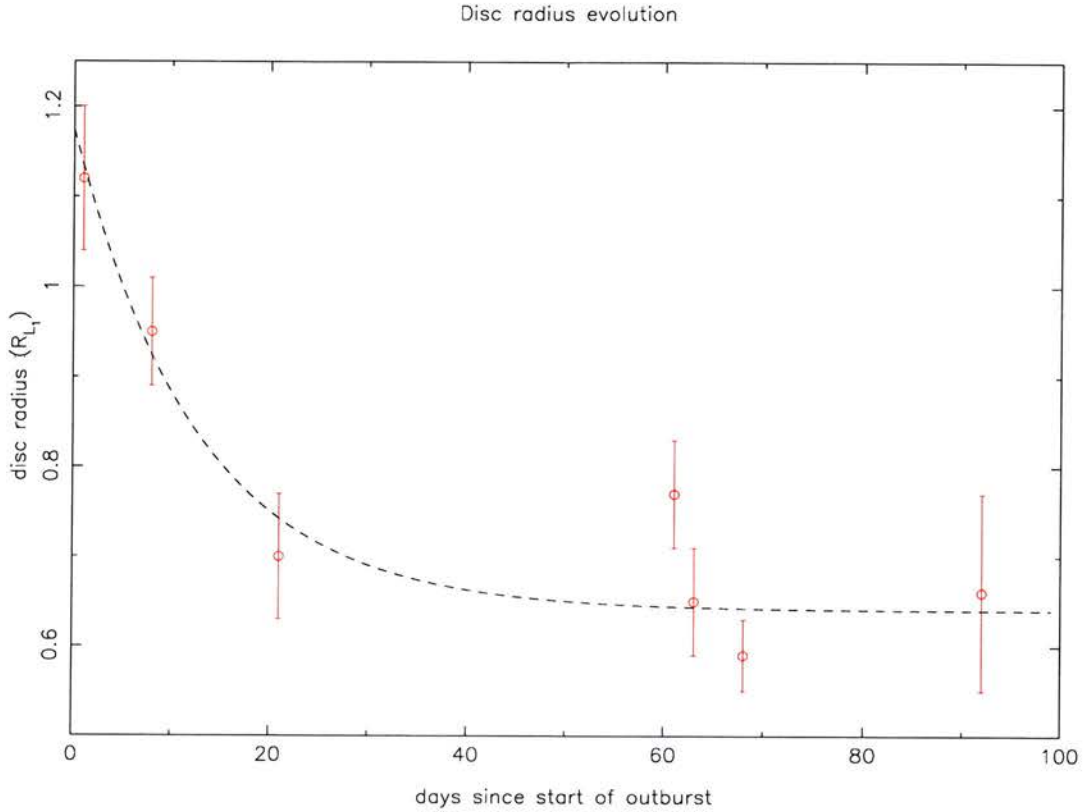


Figure 3.15: *The disc radius as a function of the number of days since the start of outburst as inferred from the velocity of the $H\alpha$ double peaks under the assumption of Keplerian velocities. The dashed line is a model fit of an exponentially decaying disc radius with an e-folding time of 12.7 days.*

both a disc instability as well as a mass transfer instability event, the latter would initially make the disc smaller since considerable amount of low angular momentum material is added. There appears to be no evidence that such a shrinkage occurs, neither is there any evidence for enhanced hot spot emission at that point. This favours the disc instability mechanism as the cause of the outburst. The inferred $H\alpha$ disc sizes in quiescence are larger than those derived from hot spot measurements ($R_{disc} \sim 0.6R_{L_1}$ compared to $0.5R_{L_1}$). Again this assumes Keplerian velocities, which is expected to be a reasonable assumption when the disc is small compared to its tidal radius ($R_{tidal} \sim 0.85R_{L_1}$). The disc size as defined in the photometric studies is the radius at which the bright spot continuum source is eclipsed. How far the stream penetrates the disc before the bright spot is produced is not clear. In some systems the velocity of the spot material is strictly ballistic, whereas in others it shares some of the disc velocities. It appears that $H\alpha$ line emission in IP Pegasi extends to larger radii

than the impact site of the stream. This disc radius is an average over all azimuths, so a non circular disc could indeed have a smaller radius near the bright spot azimuth compared to other azimuths. Alternatively, the low density material in the outer regions is still able to produce $H\alpha$ emission, whereas its continuum contribution is very small. Although following this trend of shrinkage, I refrain from interpreting the erratic disc size variations from epoch to epoch. Though these appear to be significant, more detailed observations are required to check for disc size variations that are not correlated with the outbursts. Note that Cook & Warner (1984) also found large changes in the position and shape of the bright spot in Z Cha on short timescales.

The power law indices show that the inner regions have a systematically less steep radial profile compared to the disc at larger radii and both are close to the typical exponent of 1.2 observed in many CVs (e.g. Horne & Saar 1991). This reminds us of the flat temperature profiles in the inner disc regions as derived from eclipse mapping. Also the line emission shows a flattening distribution towards the inner disc. There is a considerable variation from epoch to epoch, though it does not appear to be correlated with time since the outburst. A changing contribution of the bright spot and/or secondary star could easily influence the outer disc regions. However, it appears also to be true for the inner regions, where one does not expect much contamination of non-disc emission. Since our epochs are only snapshots and we do not have continuous coverage of the disc evolution, it is difficult to interpret these results, other than concluding that these variations are significant.

A strong spiral pattern exists in the disc of IP Pegasi in outburst, which radically changes the line emission compared to its structure in quiescence. This pattern is persistent throughout the outburst and appears to conform to the properties of tidally driven spirals. In the next chapter I will pursue a more detailed comparison of realistic hydrodynamic simulations of CV discs and the emission line properties one can observe. It is clear that even during quiescent periods, the accretion disc is far from symmetric, and its structure varies significantly from epoch to epoch. The simple picture of two accretion states, outburst and quiescence, clearly does not suffice, and a detailed study of the disc evolution throughout the outburst cycle is required to appreciate the complicated disc dynamics of unstable accretion discs. Such a project would be an extremely versatile testing bed for our understanding of

accretion discs.

3.5 The companion star and disc thickness

The late type companion star is typically observed in the optical-infrared, where its Roche lobe shape produces ellipsoidal variations across the orbit. Narrow atmospheric absorption components can usually be found during quiescent periods, provided the contribution of the secondary to the total flux is not too small, which allows spectral classification. During outburst, the disc emission dominates, however the secondary star in this case produces narrow emission lines, which can amount to a significant fraction of the line flux as we will see later in this section. Most of the energy of the hot inner disc and boundary layer regions is radiated shortward of the Lyman limit, so considerable photoionisation in the atmosphere of the companion star is expected. The accretion flow shadows some of the equatorial regions of the companion star from direct exposure to the inner disc regions, and optical recombination emission can be expected at higher latitudes on the front side of the companion. Some fraction of the deposited energy will be able to heat the red star's atmosphere, but the full implication of irradiation on the properties of the companion are not clear (e.g. King 1989; Brett & Smith 1993). Possible implications for the mass transfer rate through its L1 point have obvious relevance to both the short term and long term evolution of these systems.

In Doppler tomograms this emission can be easily identified since the star is in solid body rotation so its Roche lobe surface maps to a Roche lobe shaped area in the tomogram, at velocities lower than the disc. In IP Pegasi, emission from the red star in the Balmer lines has been reported by e.g. Marsh & Horne (1990), Harlaftis et al. (1994) and Wolf et al. (1998). In the Doppler tomograms I have presented so far in this chapter, red star emission is readily identified, in particular during outburst, but also during the epoch 5 quiescent observations (Figure 3.8). I reconstructed Doppler images for epochs 2-7. Figure 3.16 shows the $H\alpha$ emission near the Roche lobe after the symmetric ('disc') component has been subtracted.

In order to calculate the level of secondary star line flux at the various epochs, I summed up all of the emission found within 1.1 times the expected radius of the Roche lobe of the secondary and divided this by the total $H\alpha$ emission across the whole tomogram to

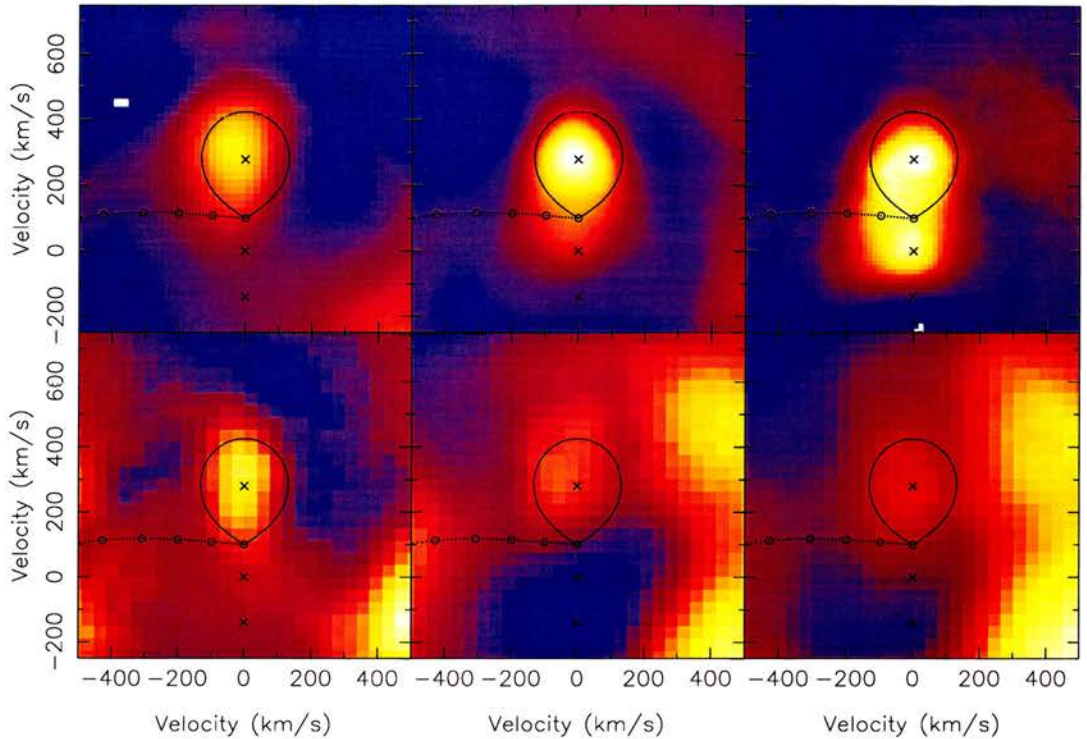


Figure 3.16: Red star emission in $H\alpha$. Plotted is a closeup of the region around the Roche lobe of the red star of the asymmetric part of the tomogram, calculated for 6 epochs. Each panel has its own colour scale, spanning the full range of the asymmetric image. Top panels from left to right are epoch 2,3,4 with epochs 5,6,7 plotted below.

derive the relative contribution of the red star to the line flux. Since tomogram values cannot be negative, a small positive bias in the image values occur. I corrected this by measuring the image values in an area at the edges of the image, where disc emission is negligible, and subtracted the derived bias from the image. This correction was always less than 0.1%. The integrated $H\alpha$ line flux for the epochs was measured by summing up the flux between ± 3500 km/s after subtracting the continuum from the average out of eclipse spectrum for each epoch. This allowed us to estimate the absolute line flux coming from the secondary by multiplying the total line flux by the derived red star fraction.

Table 3.4 lists these numbers as well as the times since previous (ΔT_1) and till next (ΔT_1) outburst. In general, Balmer emission from the red star appears to decline after the outburst, and is strong right from the start of the outburst, though its contribution still grows considerably during the first week of the outburst. Harlaftis et al. (1994) noted Balmer emission from the red star a few days before an outburst, and indeed red star emission is

Table 3.4: *Red star contribution to the H α line flux*

Epoch	ΔT_1 days	ΔT_2 days	bias corrected red star fraction (%)	total H α flux $10^{-13} \text{erg cm}^{-2} \text{s}^{-1}$	red star flux $10^{-15} \text{erg cm}^{-2} \text{s}^{-1}$
2	68 \pm 1	22 \pm 1	2.1	1.48	3.11
3	0 \pm 1	68 \pm 1	7.0	11.25	78.75
4	7 \pm 1	61 \pm 1	10.0	11.75	117.5
5	63 \pm 1	5 \pm 1	2.9	0.830	2.41
6	92 \pm 1	9 \pm 1	1.6	2.61	4.16
7	21 \pm 1	-	2.2	2.21	4.86

always detectable during our observations at the level of a few percent. I find that just before the December 1994 outburst, the red star contribution is 1.6%. Whether intrinsic emission coming from an active secondary is responsible for this, or whether irradiation during quiescence is still able to produce red star emission is not clear. What we do see is an increase by a factor of ~ 50 in the line flux from the secondary during outburst, whereas the disc flux increases by a factor of 5-10. Since the bright spot is not contributing significantly to the ionising flux during outburst, most of this must be powered by the boundary layer and sufficiently hot areas in the disc.

The curious low velocity components discussed in Steeghs et al. (1996) are clearly visible in the late outburst data (Epoch 4), but already at the start of the outburst (Epoch 3), red star emission extends to low velocities. In the picture of a slingshot prominence attached to the red star, this could be the start of the prominence being filled with gas while irradiated by the bright disc. Note that this component was not included in the red star emission fluxes detailed in Table 3.4. We saw earlier that a similar component was visible in the HeII 4686 line, just like in the dwarf nova SS Cyg, which exhibits very similar components. Again, I refer to the Steeghs et al. (1996) paper for a more thorough discussion of the interpretation of such emission sources.

During outbursts, secondary star emission is not just visible in the Balmer lines, but also in HeI and even HeII (Figure 3.13). On closer inspection, the outburst spectrum contains many faint emission line components that move in phase with the secondary. Figure 3.17

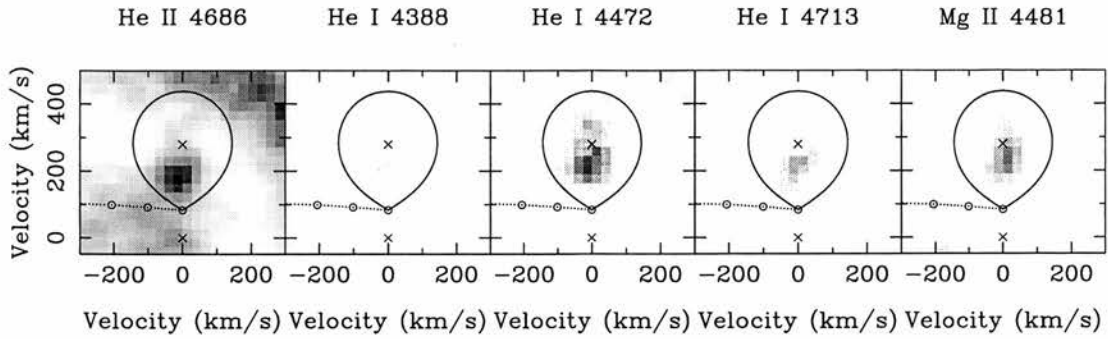


Figure 3.17: Line emission from the red star during outburst. Shown is a close up of the regions around the Roche lobe for a range of high excitation potential transitions. Instrumental resolution is good enough to resolve the emission across the red star’s atmosphere.

Table 3.5: The red star emission across the Roche lobe

	He II 4686	He I 4388	He I 4472	He I 4713	Mg II 4481
V_y (km/s)	185	216	213	218	240
FWHM (km/s)	125	75	92	103	127

maps the distribution across the Roche lobe for various lines, starting from high-excitation to low-excitation lines (He II 4686, He I 4388, He I 4472, He I 4713, Mg II 4481). The scale of all panels are identical to conserve the relative strengths.

I measured the velocity locations of the peak intensities on the Doppler images using Gaussian fitting, with respect to the center of mass. Table 3.5 lists the measured positions and FWHM of the secondary star emission for the 5 transitions. There is a systematic shift towards the L_1 point with higher-excitation potential. The rotational broadening of the companion star, $v \sin i = 163 \text{ km s}^{-1}$, can be obtained from the relation

$$\frac{v \sin i}{K_2} = 0.462 \left[(1 + q)^2 q \right]^{1/3}.$$

The width (FWHM) of the spot emission on the Roche lobe as given from the Gaussian fits is consistently larger than the instrumental resolution of 55 km/s, yet smaller than $v \sin i$, confirming that we are indeed resolving emission regions smaller than the Roche lobe radius. All emission spots are significantly removed back from the L_1 point. The Roche lobe maps may suggest that the shadow cast by the disc on the companion star decreases with higher energy photons (Mg II, He I, He II). Taking the parameters for IP Pegasi, the maximal allowed

disc opening angle θ_{disc} is 17.4° as derived from a numerical Roche lobe model. Thicker discs would prevent any UV radiation from hitting the Roche lobe. Using the observed velocities of the HeII component, and correcting for the fact that finite instrumental resolution will blur the recovered emission to lower (and higher) velocities compared to the true distribution, I can set a lower limit to the velocity of the HeII component of 150 km/s, leading to an upper limit of the disc opening angle of $\theta_{disc} \leq 12^\circ$. For comparison, the velocity of the L1 point is 102 km/s. Note that this value does not assume a constant opening angle disc, but states that the relative disc thickness H/R cannot exceed the value $H/R = \tan^{-1}(\theta_{disc}) = 0.21$ at any radius R in the disc. Strictly speaking, it is the optical depth τ between the UV source and the Roche lobe that has to be large enough to prevent the photons from hitting the companion:

$$\tau = \int \kappa(s)\rho(s) ds = \int N a_\nu ds \quad (3.1)$$

where the integral over s integrates along the line between the UV source and the Roche lobe surface. For neutral hydrogen the photo-ionisation cross section is $a_\nu \sim 6.3 \times 10^{-18} \text{ cm}^2$ (Verner et al. 1996), requiring a column density of $\int N ds \sim 10^{17} \text{ cm}^{-2}$ in neutral hydrogen to shield the Roche lobe from the UV source. Accordingly, the average density of neutral hydrogen in the upper layers of the disc has to drop below $\sim 10^7 \text{ cm}^{-3}$ in order to allow photo-ionisation of the companion star.

The effective disc thickness H_{eff} is the height z below which photons are absorbed, $H_{eff} = z(\tau = 2/3)$, and will be a function of wavelength depending on the dominant opacity source $\kappa(\rho, T)$. Conventional wisdom states that H/R in CV discs should be a few percent, and although no emission at low velocities is observed, it does not necessarily imply the disc is as thick as 12° . The fact that different lines form at different areas across the surface is also partly due to intrinsic ionisation structure across the Roche lobe, since the incident angle of the impending UV/X-ray photons changes considerably as a function of position along the Roche lobe. Thus only an upper limit to the disc thickness can be derived. High resolution data on the emission components could improve this limit further, combined with a more realistic irradiation model to study the properties of the red star's atmosphere and, indirectly, the intervening disc structure.

CHAPTER 4

Simulating tidal spiral waves

Despite the firm prediction of shocks in accretion discs, two armed spiral signatures have only recently been found by Steeghs, Harlaftis & Horne (1997,1998) and Harlaftis et al. (1999) in the eclipsing CV IP Pegasi during outburst (Chapter 3). Doppler tomograms revealed a strong two-armed spiral pattern in the outer disc. Even though Doppler tomography is ideally suited to detect asymmetric disc structures (see e.g. Robinson, Marsh & Smak 1993), it is unclear if previous observations failed in reconstructing spiral arms because of insufficient data quality or because spiral arms were not present in the disc at the time of the observation. The purpose of this chapter is to clarify this question and to predict observational signatures of tidal density waves in high and low Mach number (M) accretion discs, the latter appropriate for accretion discs during dwarf nova outbursts. I used the emission line model of Horne (1995) to calculate emission line profiles for various binary configurations, using the grid of full hydrodynamic disc calculations by Stehle (1999) as underlying models. Part of this chapter is published in Steeghs & Stehle (1999).

4.1 The grid of hydrodynamic disc models

As our underlying disc models I used the grid of geometrically thin 2D-disc calculations by Stehle (1999). These disc simulations were performed using a new model for the hydrodynamics of thin discs as presented by Stehle & Spruit (1999). In the orbital plane, full hydrodynamics is taken into account using a two dimensional (r, ϕ) cylindrical grid centered on the

primary star, co-rotating with the binary. Additional equations for the time evolution of the disc thickness $H(r, \phi, t)$ are included to study the response of the disc to tidal and thermal disturbances. Vertical disc oscillations can be excited by various mechanisms; cooling/heating waves, surface waves such as generated by the impact of the gas stream and vertical motions due to the tidal forces of the companion star. The last mechanism is particularly important since resonances can occur as the fundamental mode of vertical disc oscillation is close to the Keplerian frequency. In the one-zone treatment used by Stehle & Spruit (1999), vertical motions are restricted to symmetric compressions and expansions. This correctly reproduces the vertical motions of thin discs to first order. These disc simulations can thus be viewed as an intermediate step between 2D and full 3D calculations.

The spatial and temporal evolution of the disc temperature follows tidal and viscous heating, the latter in the α -ansatz of Shakura & Sunyaev (1973). As the origin of the viscosity is not known, any radial viscous forces were neglected and thus a maximum amplitude for the shocks was derived. Whether or not this is a sensible assumption is one of the main questions to be answered by comparing accretion disc models with detailed observations. The energy loss rate by radiation from the disc surface is related to the mid-plane temperature by a standard radiative diffusion model using Rosseland mean opacities. The equation of state is that of an ideal gas of constant ratio of specific heats ($\gamma = 1.4$). Although not strictly 3D, the one zone model treatment of the vertical motions allows us to evaluate self occultation effects by the vertically extended disc.

Our time dependent calculations were time averaged over at least one binary orbit in the co-rotating frame of the binary, i.e.

$$\bar{f} = \frac{1}{t_f - t_i} \int_{t_i}^{t_f} f(t) dt \quad (4.1)$$

where f is any conservative physical quantity, like the momentum in radial direction p_r , the angular momentum p_ϕ , the vertical momentum p_z , the surface density Σ or the internal energy density e . Other quantities, such as the disc gas velocity, are derived from the time averaged values. For the remainder of this Chapter, I will deal only with time-averaged values and thus we subsequently drop the bar in our notation for convenience. By averaging our models in time, only those disc features which are reasonably stable over a dynamical time scale will still be visible. This ensures that the remaining disc structure can be recovered

using Doppler tomography.

I will be presenting the results of two model simulations. Both models are simulations of the accretion disc in a binary with mass ratio $q = M_2/M_1 = 0.3$ and orbital period $P = 2.3$ hours. The α -type Shakura & Sunyaev viscosity in model I (Figure 4.1) is 0.01 and I time-averaged over ~ 1.5 binary orbits. Model II (Figure 4.2) represents a typical dwarf nova outburst disc with $\alpha = 0.3$, time averaged over ~ 1 orbital period. I also calculated model predictions for various other mass ratios and different averaging times. These all shared the same qualitative features as Model I and II since the spiral arms are very stable in the binary frame and mainly depend on the disc temperature (see also Stehle 1999), and so are not shown here. Unfortunately, no disc simulations were available using the system parameters of IP Pegasi. However, we expect no qualitative differences between the simulations presented here and the disc structure in a binary with a slightly higher mass ratio. These two models in particular were selected as a typical comparison between a small, cool disc (I) versus a large, hot viscous disc (II). I show in Fig. 4.3 the run of T_{eff} with disc radius r in units of the distance to the L_1 point. In both cases $T_{\text{eff}} \propto r^{-3/4}$ in the inner parts of the disc, as expected from stationary viscous accretion discs. Close to the outer disc edge though, tidal heating and non-axisymmetry result in a large spread of T_{eff} .

4.2 Emission lines from spiral shocks

4.2.1 Doppler tomograms and line profiles

For our analysis I use a right-handed Cartesian coordinate system $(\vec{e}_x, \vec{e}_y, \vec{e}_z)$ centred on the white dwarf, with the positive X-axis in the direction of the secondary star and \vec{e}_z parallel to the rotation vector of the accretion disc. The disc gas velocities are transferred to inertial velocities corresponding to the centre of mass of the binary. To calculate the line emissivity for each disc grid cell, I follow the analysis of Horne & Marsh (1986) and Horne (1995). The emission line surface brightness J is obtained by integrating over the local line profile times the foreshortening due to the orbital inclination i ;

$$J = \cos i \int S_L(1 - \exp(-\tau_\nu)) d\nu \quad (4.2)$$

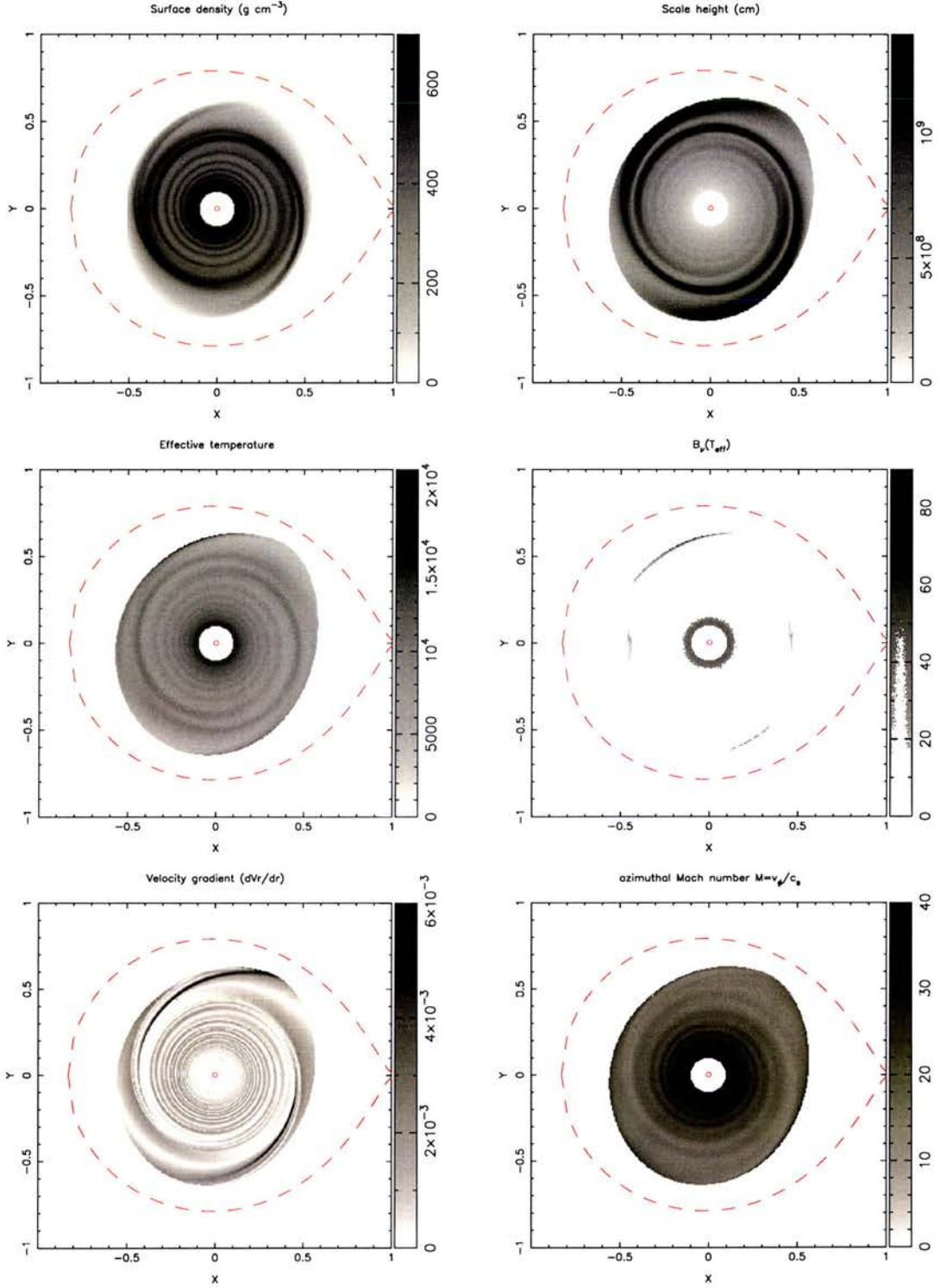


Figure 4.1: *Some of the properties of disc Model I. Plotted are the distributions of surface density (Σ), effective temperature (T_{eff}), the Planck function $B_\nu(T_{eff}, \lambda = 4861\text{\AA})$, one component of the velocity gradient tensor ($\frac{\partial v_r}{\partial r}$) and the azimuthal Mach number $M = v_\phi/c_s$ in the orbital plane of the binary.*

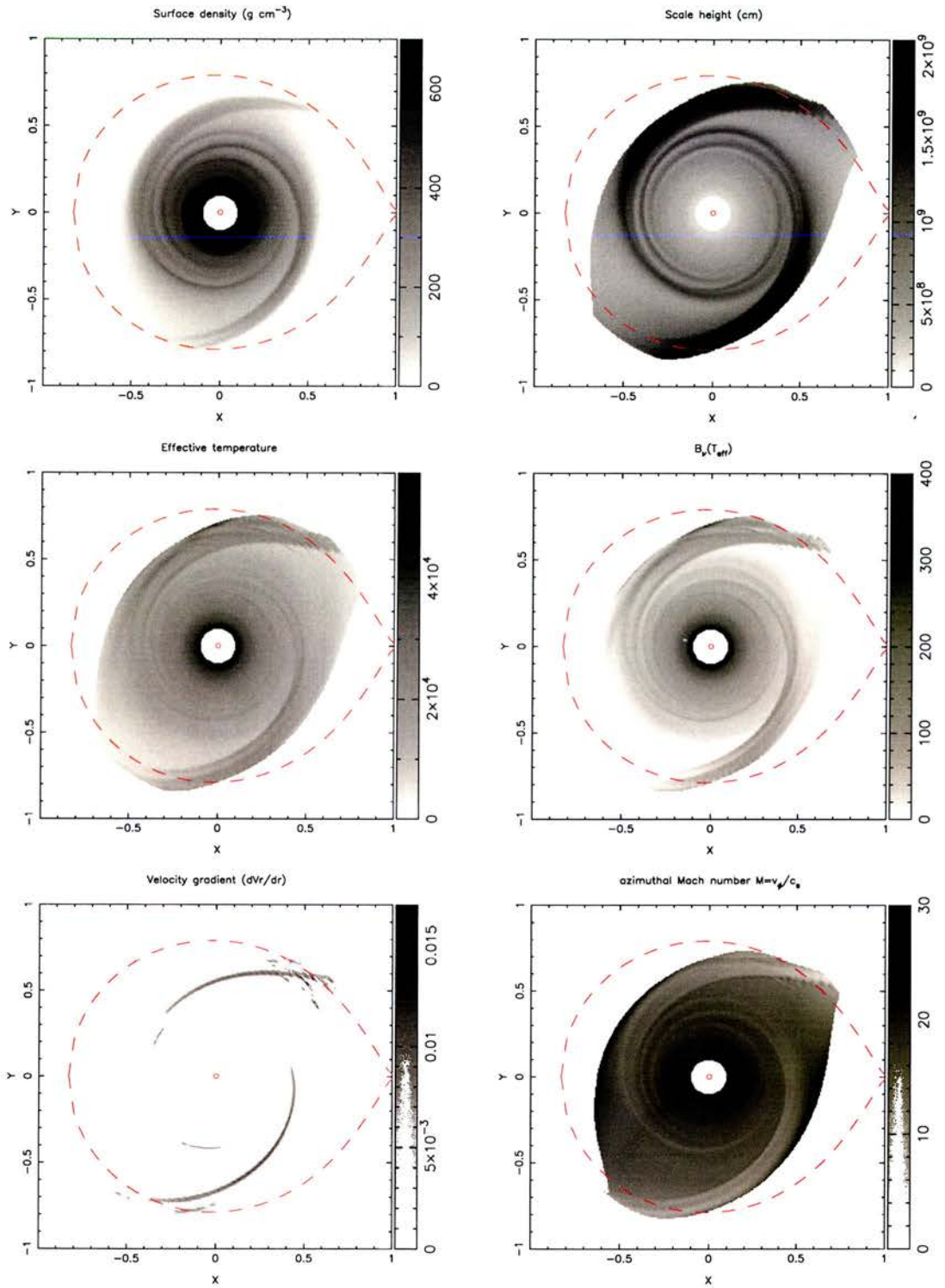


Figure 4.2: Same as figure 4.1, now for Model II.

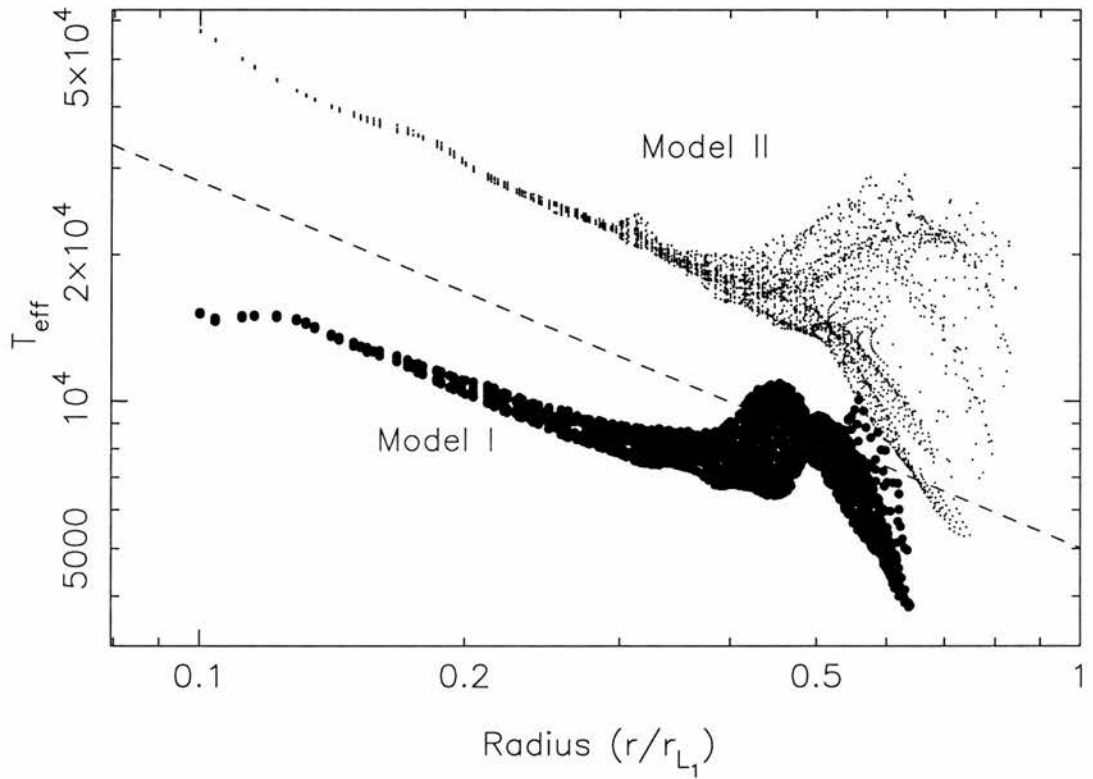


Figure 4.3: *The effective temperature $T_{\text{eff}}(r)$ versus the disc radius r/r_{L_1} for models I ($\alpha = 0.01$, lower data) and II ($\alpha=0.3$, upper data). $T_{\text{eff}}(r)$ follows closely the power $r^{-3/4}$ (dashed line), as expected for hot, stationary accretion discs. Near the outer disc edge, the effects of tidal heating and non-axisymmetry result in a wide range of disc temperatures.*

In the case of optically thin line emission, $J(x, y)$ is proportional to the surface density $\Sigma(x, y)$ and the local line source function $S_L(\lambda)$. However, most strong emission lines such as the hydrogen Balmer series are optically thick and saturated (e.g. Ferguson 1997). The area under the profile is then well approximated by the product of S_L and the frequency interval over which the optical depth exceeds unity. Using eq. (15) from Horne (1995), the local line emissivity of a saturated emission line with rest wavelength λ_0 is in that case given by:

$$J(x, y) = S_L \frac{\Delta V}{\lambda_0} \cos i \sqrt{8 \ln \tau_0} \quad (4.3)$$

ΔV is the total velocity dispersion along the line of sight, τ_0 the optical depth of the centre of the emission line. If we furthermore assume local thermodynamic equilibrium, S_L equals the Planck function. The velocity dispersion consists of a thermal component $V_{\text{th}} = \sqrt{kT/m_{\text{H}}A}$, with m_{H} the mass of a hydrogen atom and A the atomic weight, and a shear term V_{shear} , derived from the full, non-Keplerian, velocity field. ΔV is evaluated for each grid cell and viewing angle according to

$$\Delta V^2 = V_{\text{th}}^2 + V_{\text{shear}}^2 \quad (4.4)$$

where

$$V_{\text{shear}} = \frac{\Delta Z}{\cos i} \vec{e} \cdot \vec{\nabla} \vec{V} \cdot \vec{e} \quad (4.5)$$

$$= \frac{\Delta Z}{\cos i} \vec{e} \cdot \begin{pmatrix} \frac{\partial V_x}{\partial x} & \frac{\partial V_y}{\partial x} & \frac{\partial V_z}{\partial x} \\ \frac{\partial V_x}{\partial y} & \frac{\partial V_y}{\partial y} & \frac{\partial V_z}{\partial y} \\ \frac{\partial V_x}{\partial z} & \frac{\partial V_y}{\partial z} & \frac{\partial V_z}{\partial z} \end{pmatrix} \cdot \vec{e} \quad (4.6)$$

\vec{e} denotes the earth vector pointing from the grid cell towards the observer, and $\vec{\nabla} \vec{V}$ is the tensor of the local velocity gradient including all anisotropic terms. In this way the velocity field of our simulations self consistently provides the total velocity dispersion along each line of sight. ΔZ denotes the vertical extent of the emission line layer and is assumed to be $0 \leq \Delta Z \leq H$.

Since $\tau_0 \propto \Sigma/\Delta V$ we derive:

$$J(x, y, \phi, i) \propto B_\nu(T_{\text{eff}}) \Delta V(x, y, \phi, i) \sqrt{\ln\left(\frac{\Sigma(x, y)}{\Delta V(x, y, \phi, i)}\right)} \quad (4.7)$$

The line emissivity is then proportional to the local velocity dispersion ΔV . The large gradients across the spiral shocks will therefore enhance the local emissivity of saturated lines

significantly at the location of the spiral arms. This will produce anisotropic emission from the spiral arms, producing maximum line emission when the line of sight crosses perpendicular through the shock.

In order to calculate the line emissivity at a particular velocity (V_x, V_y) , we multiply $J(x, y)$ with the Jacobian of the coordinate transformation, i.e.

$$J(V_x, V_y) = \left| \begin{array}{cc} \frac{\partial V_x}{\partial x} & \frac{\partial V_x}{\partial y} \\ \frac{\partial V_y}{\partial x} & \frac{\partial V_y}{\partial y} \end{array} \right|^{-1} J(x, y). \quad (4.8)$$

For each binary phase ϕ the line profile $f(V, \phi)$ is synthesised by adding up the individual contributions of the grid cells where the emission line contribution is Doppler shifted according to the local gas velocity along the line of sight, $V_{dop} = -\vec{V} \cdot \vec{e}$. I adopt the usual convention that phase 0.0 corresponds to inferior conjunction of the companion star, i.e. mid-eclipse in high inclination systems. The visible area $A(x, y)$ of each grid cell is tested for eclipses by the companion star which I assume to fill its critical Roche volume;

$$f(V, \phi) = \frac{\cos i}{d^2} \iint J(x, y, i, \phi) \frac{1}{\sqrt{2\pi\Delta V}} e^{-\frac{1}{2}\left(\frac{V-V_{dop}}{\Delta V}\right)^2} A(x, y) dx dy \quad (4.9)$$

with d the distance to the system.

The above description to construct emission line profiles holds principally for all *saturated* emission lines. I choose the H β line at 4861Å as our reference line for most calculations. The Balmer lines are the most prominent lines in CV spectra and allow disc reconstructions at a high signal to noise. It serves as a typical representative line observed in optical emission line studies of CVs. Since I am concerned with the dynamical properties of the line profiles rather than calculating absolute line strengths, this particular choice does not affect our subsequent analysis. To illustrate the effects of saturation I will calculate both the case of no shear and maximum shear broadening as well as compare with the properties of an emission line from a heavy element such as calcium.

4.3 Model predictions

In this section I present predicted emission line profiles and Doppler tomograms for the disc models limited only by the finite grid resolution of our hydro-dynamical calculations. As

we will see in Sec. 4.4, the limits set by the instrumentation will dominate over our limited numerical grid resolution and it is thus appropriate to call our tomograms in this section “ideal”. We identify the signatures of spiral waves in the emission lines of accretion discs. As the global shape of the spiral shocks is characterised by the Mach number of the disc, I present the model predictions in descending order of M .

4.3.1 Axisymmetric discs

The properties of emission lines from axisymmetric accretion discs have been investigated by several authors (e.g. Smak 1981, Horne & Marsh 1986), of which I summarise a few relevant features. The large Keplerian velocities of a few thousand km s^{-1} in the inner disc down to several hundreds km s^{-1} in the outer disc, produce very broad emission line profiles, decoupling the global shape of the line from the local line radiative transfer. A double peaked shape results, where the peak velocities reflect the motion of the gas at the outer disc edge, which in turn can be used to estimate the size of the disc if a velocity field, such as Keplerian, is assumed (cf. Figure 2.2).

The orbital velocity of the white dwarf is sometimes estimated by measuring the centroid of the observed line profile, which should show a sinusoidal dependence with orbital phase as the white dwarf orbits around the binary center of mass. While the line profile as a whole thus moves, the separation between the double peaks is constant with phase. In the velocity coordinate space of Doppler tomograms, axisymmetric discs will produce axisymmetric circular images, centered on the radial velocity of the white dwarf ($V_x = 0, V_y = -K_1$, with K_1 the projected orbital velocity of the white dwarf). For each radius, a corresponding ring at the local disc velocity is produced, with the smallest velocities corresponding to the outer edge.

4.3.2 Model I: High Mach number disc

In Fig. 4.4 I show the model predictions for the high Mach number CV disc of model I, viewed at an inclination of 80° . The spatial distribution of the line emission is plotted in the top left panel and displays a rather small disc, varying in radius between $r_{\text{out}}(\phi) \simeq 0.55 - 0.65 r_{L_1}$.

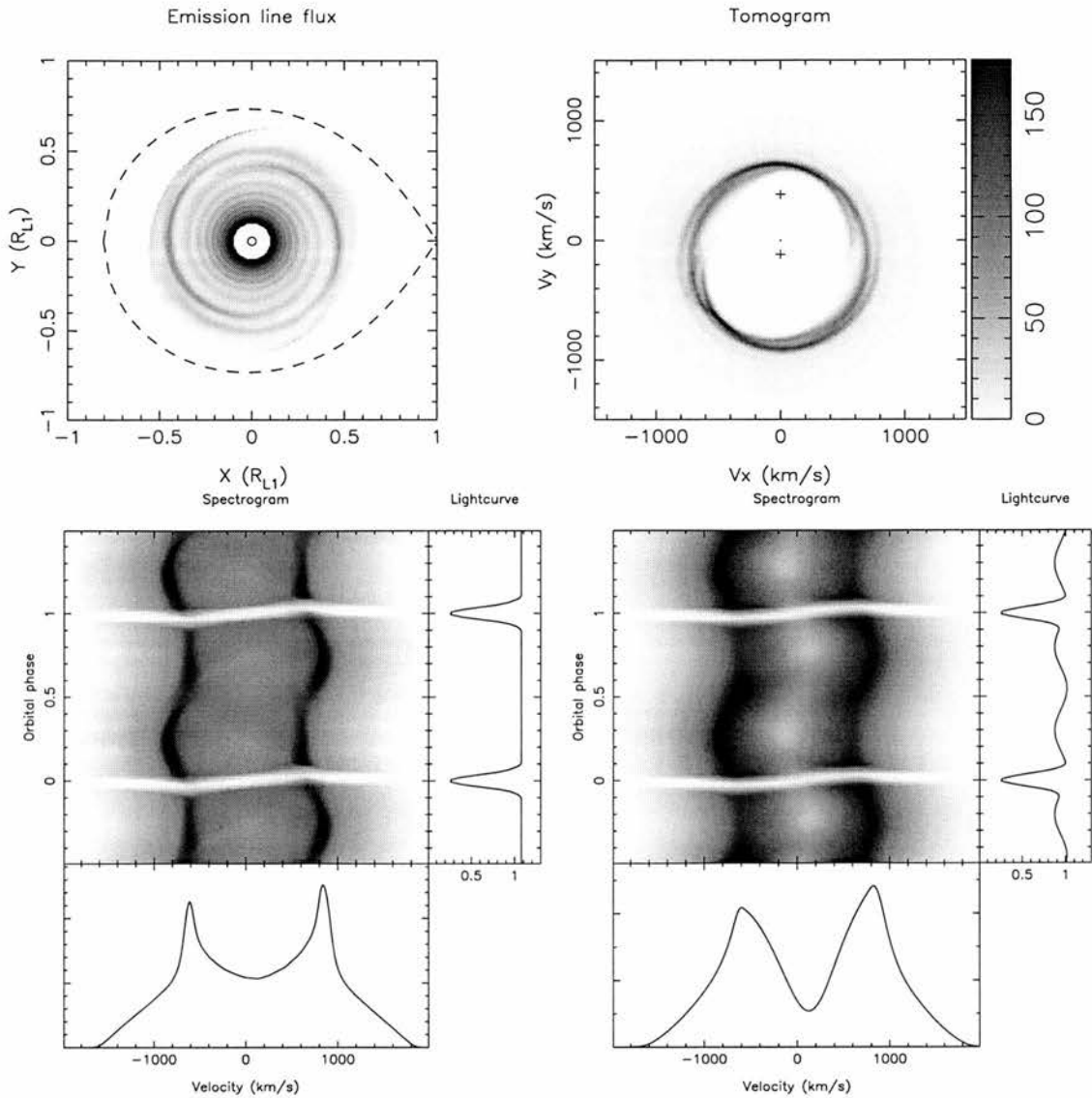


Figure 4.4: *Model I: an $\alpha = 0.01$ disc in a binary with $q = M_2/M_1 = 0.3$. Top panels show the distribution of line emission in both spatial coordinates (left) as well as in the $V_x V_y$ -plane in the limit of a thin emission line layer. The crosses in the tomogram denote the projected radial velocity of the white dwarf (lower cross) and secondary star. Bottom panels display the calculated emission line profiles for hydrogen-like lines at an inclination of 80° . Bottom left with no shear broadening (i.e. a thin emission line layer), right with maximum shear broadening when line emission is produced across the whole disc height. To the right of each trailed spectrogram is the total line flux light curve, and below it the emission line profile at orbital phase 0.75.*

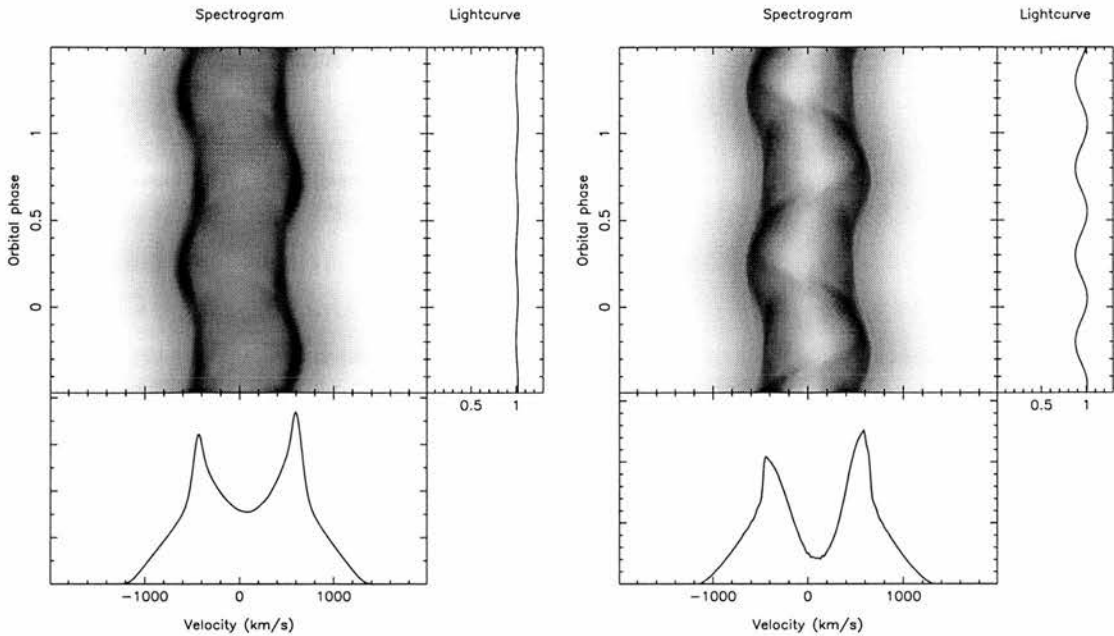


Figure 4.5: *The effect of atomic weight on the shear broadened profiles. On the left are the line profiles for Model I viewed at an inclination of $i = 45^\circ$ for a hydrogen line ($A=1$). The right panel is for a saturated calcium line ($A=40$). Because of the much smaller thermal velocity in the case of calcium, the shear broadening is much stronger than for hydrogen lines. This results in a stronger signature of spiral waves in the emission lines.*

Tightly wound spiral shock arms cover the disc down to small radii. Note that since the shear broadening effect is orbital phase dependent, the plotted line distribution is in the limit of a geometrically thin emission line layer ($\Delta Z = 0$) where shear broadening vanishes. If we plot the same distribution in velocity coordinates (top right), the typical ring shape appears, with the two shock arms visible as sharp arcs of enhanced line emissivity in the top and bottom regions. The outer disc edge provides a cut off of any emission with velocities lower than $\sim 600 \text{ km s}^{-1}$ while at high velocities, the inner disc, the tomogram becomes more symmetrical. The emission line profiles in the corresponding trailed spectrograms (Fig. 4.4, bottom panels) feature two sharp peaks, reflecting the velocities of the outer disc gas. Two cases are plotted to illustrate the effect of shear broadening due to the finite thickness of the emission line region (Horne & Marsh 1986). In the bottom left panels, the emission line layer is assumed to be very thin ($\Delta Z/H \simeq 0$), so that shear broadening effects vanish and sharp and narrow double peaks are formed. This is very similar to the optically thin case. On the right is the case of maximum shear broadening, assuming the emission lines are formed across the full

disc thickness such that $\Delta Z = H$ in eq. (4.5). Broad peaks with a V-shaped, rather than U-shaped, valley between the peaks are formed.

The presence of spiral arms slightly distorts the velocity of the peaks as a function of binary phase, varying between $v_{\text{peak}}(\phi) = 690 - 750 \text{ km s}^{-1}$ with respect to the white dwarf. On average, the double peak separation is $\langle v_{\text{peak}} \rangle = 725 \text{ km s}^{-1}$. This corresponds to a disc radius of $r_{\text{out}} \simeq GM_1 / \langle v_{\text{peak}} \rangle^2 = 0.61 r_{L_1}$, assuming Keplerian velocities. While the disc is slightly tidally distorted and elongated along the Y -direction, the assumption of Keplerian velocities still provides a reliable estimate of the average disc size in this case.

Shear broadening can be particularly important for heavy elements. Their low thermal velocity results in a stronger local enhancement of the line flux due to velocity gradients. To illustrate this, Figure 4.5 shows the line profiles of a light element ($A=1$) versus that of calcium ($A=40$) at an inclination of 45° . While for hydrogen like lines the shear broadening is no longer important due to foreshortening, the calcium line displays strong anisotropic components originating along the spiral arms. I again measured the position of the double peaks by fitting two Gaussians to the line profiles and measuring the double peak separation (Figure 4.6). The amplitude of the variation is now 13% as opposed to 8% in the case of a hydrogen line. Interestingly, the center of the two peaks still follows the radial velocity of the white dwarf quite accurately, even though the positioning of the individual peaks have a strong phase dependence.

The orbital variation in the separation of the double peaks is the predominant signature that the disc is asymmetric and that the emissivity is not uniform. In the case of considerable shear broadening, the line emission from the spiral shocks is additionally non-isotropic, resulting in a binary phase dependent variation of the peak strengths with a maximum at phases 0.25 and 0.75, as is visible in the emission line flux light curves to the right of the spectrograms. Such non-isotropic line emission cannot be modeled by Doppler tomography, since only the average line flux at a given velocity is provided, but can be identified in the emission line profiles directly as a signature of shocks in the outer disc. While saturated emission lines from heavy elements are thus good indicators of large velocity gradients, they are unfortunately usually weak lines and it will be demanding to achieve sufficient signal-to-noise for Doppler imaging.

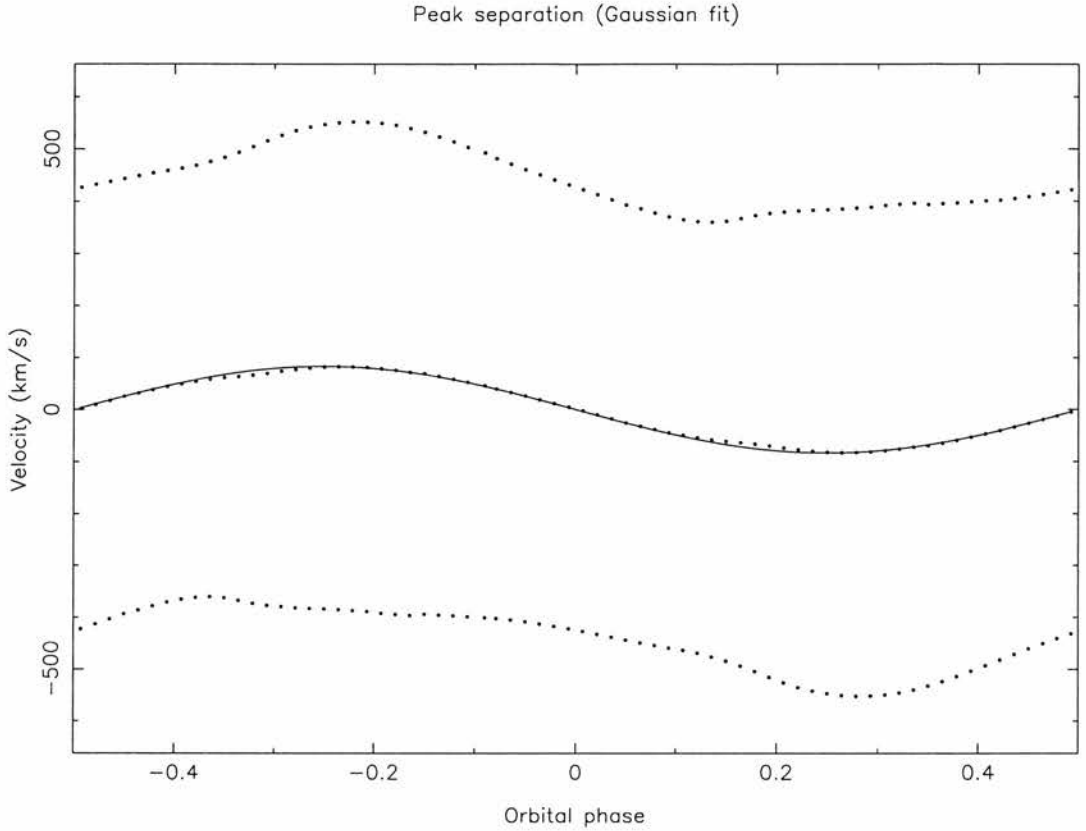


Figure 4.6: *The velocities of the double peaks as measured through Gaussian fitting for the calcium data in Figure 4.5. The top curve represents the velocity of the red wing, the lowest curve that of the blue wing. The middle curve plots the center of the two wings together with a sinusoidal curve denoting the radial velocity of the white dwarf.*

4.3.3 Model II: dwarf nova outbursts

By increasing the parameter of the small scale viscosity to $\alpha = 0.3$ in Model II, viscous spreading becomes more efficient in pushing the accretion disc towards larger radii of $r_{\text{out}}(\phi) \simeq 0.6 - 0.8 r_{L_1}$ (see Fig. 4.7, top left panel). The increased local viscous heating additionally produces higher disc temperatures, and thus lower Mach numbers, now of the order $M \sim 5-20$. This is reflected in the open geometry of the two spiral shock arms in the outer disc. In Fig. 4.7 I present the calculated emission line properties for model II, again at an inclination of $i = 80^\circ$.

It is difficult to assign a meaningful disc radius as the line emissivity is predominantly localized at the two spiral arms. The strong two-armed spiral wave pattern in the outer disc

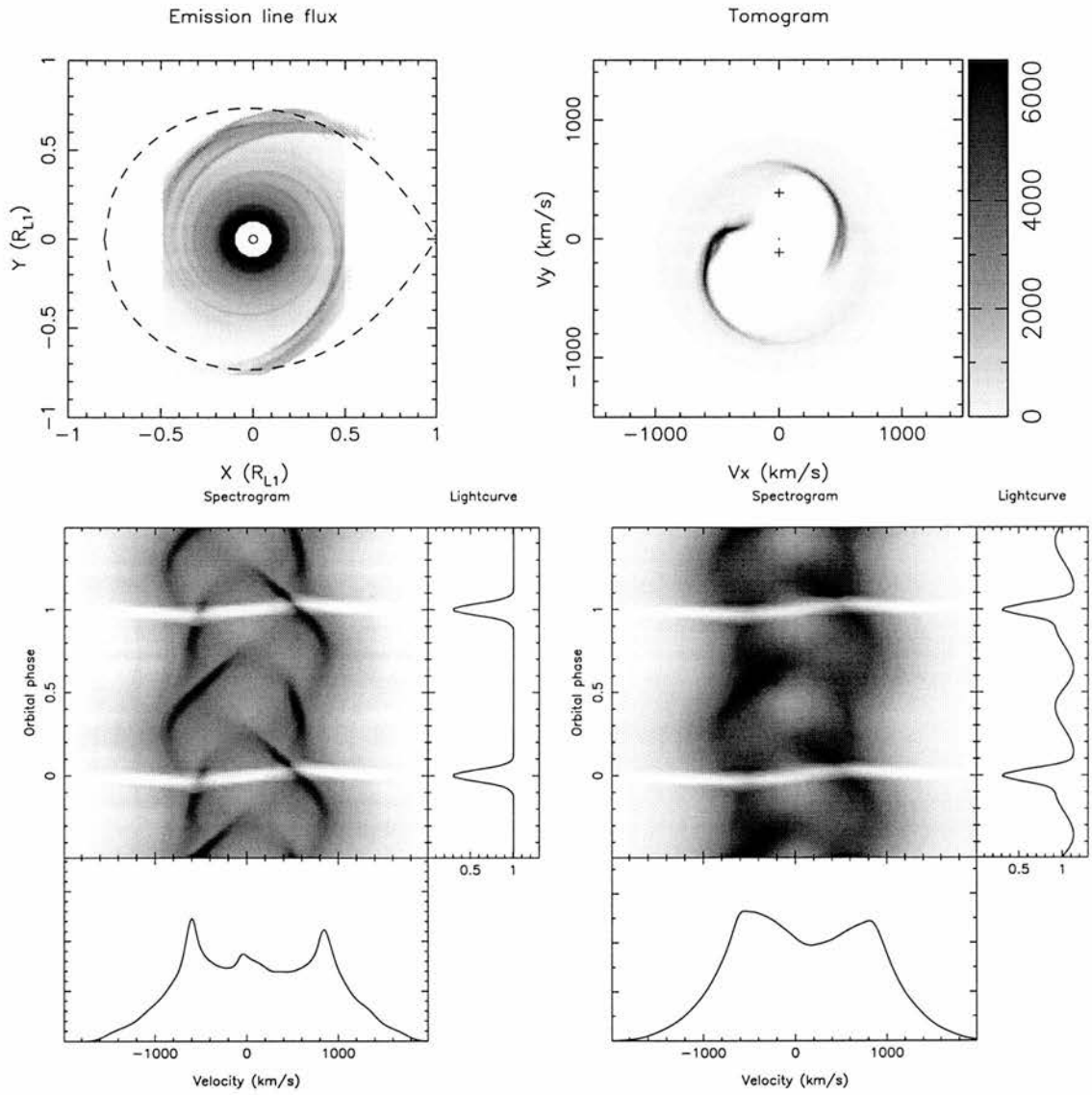


Figure 4.7: As Fig. 4.4 but now for the low Mach number disc of model II.

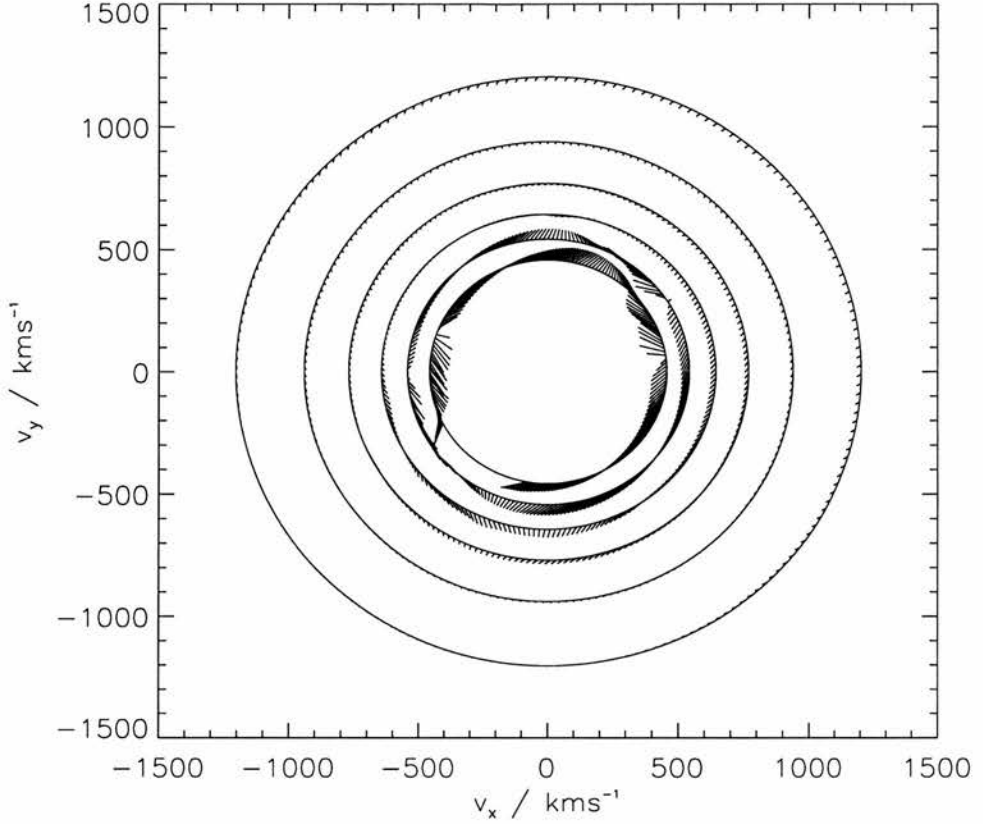


Figure 4.8: *Non-Keplerian velocities in Model II. The circles denote the Keplerian velocity at a few radii in the disc. The small ticks point to the actual disc velocity at that radius and azimuth. The tidal distortions become prominent in the outer disc, i.e. at low velocities in the inner regions of the Doppler map.*

dominates the corresponding Doppler tomograms, shown in the top right panel of Fig. 4.7. The line emission extends towards lower velocities ($\sim 500 \text{ km s}^{-1}$) than in Model I, partly because of the increased disc size, and partly because sub-Keplerian motions are significant in these outer regions. Figure 4.8 shows the deviation from Keplerian velocities at a few representative radii. While the disc is close to Keplerian in its inner regions (high velocities), the departures at the outer disc near $v \sim 500 \text{ km s}^{-1}$ are significant and of the order of $\sim 100 \text{ km s}^{-1}$.

The line profiles are easily distinguishable from an axisymmetric disc. The spiral pattern results in converging emission line peaks, with a cross over near phases 0.25 and 0.75. This contrasts with the axisymmetric case, which has a constant double peak separation, independent of orbital phase. Though a non-circular disc could also produce a variation in

the double peak separation with phase, it would not produce the existence of multiple peaks as one crosses from one spiral arm to the next, with a corresponding sudden jump in velocity of several hundred km s^{-1} , a unique signature of a spiral shock pattern. Again the large velocity gradients are important at high inclinations where shear broadening can dominate. This produces a variation in the emission line light curve (Fig. 4.7 bottom right panel) which is of considerably larger amplitude compared to Model I.

4.4 Reconstructing spiral structures using tomography

4.4.1 Realistic data quality

In the previous section I discussed the model predictions limited by the grid resolution of our hydro-dynamical models. I now include instrumental noise and finite spectral/time resolution in our predicted data to provide a realistic comparison with observed data and constrain the necessary data requirements to reconstruct tidal arms in CV discs.

Three instrumental effects play a role. First, the wavelength resolution of the individual spectra, setting a limit to the velocities that can be resolved. On the one hand, the emission lines typically span several thousands of km s^{-1} , which need to be sampled by ample numbers of pixels. On the other hand, resolutions much better than the width of the local line profile ($\sim 10 \text{ km s}^{-1}$) do not provide any additional information. A resolution of $\sim 20\text{-}80 \text{ km s}^{-1}$ is therefore usually optimal, though in practice it is limited by signal to noise requirements.

Second, the phase or time resolution has to be short enough to provide sufficient phase sampling across the binary orbit to avoid artifacts in the image reconstruction (see also Marsh & Horne 1988). The higher the spectral resolution of the input data, the more projections are required to provide sufficient sampling and exploit the available resolution. To avoid undersampling the image one typically needs at least 50 orbital phases.

Finally, the signal to noise of the individual spectra will determine how well the data will constrain the image structure. In the case of maximum entropy reconstruction, as is the case here, the reconstructed image is a balance between fitting the data using maximum likelihood statistics and selecting the simplest image using the maximum entropy criterion.

To test the importance of the above effects, I started by calculating ideal line profiles (such as presented in Section 4.3) for an inclination of 45° at 50 orbital phases equally spaced over the binary orbit. The data were then convolved with a Gaussian with FWHM equal to the desired instrumental resolution and binned in wavelength such that 2 data pixels cover the instrumental profile. Poisson noise was subsequently introduced to achieve different signal to noise levels in the line profiles as follows. We added a continuum to our line profiles such that the line strength (line - continuum) was equal to about two times the continuum level, a typical value for the strong emission lines in dwarf novae. Poisson noise was then added to achieve the desired signal to noise level in the continuum. Using the synthetic noisy data, I reconstructed maximum entropy Doppler tomograms using the same code as used for the observations ¹.

4.4.2 High M model

Figure 4.9 shows the image reconstructions based on model I, at an inclination of 45° and including maximum shear broadening. The top panels show the simulated data, the left has a 2-pixel resolution of 40 km s^{-1} , the middle and right have a resolution of 80 km s^{-1} . The signal to noise in the left and middle panels is ~ 50 in the assumed continuum, while for the right panel it is degraded to ~ 15 . Below each trailed spectrogram the reconstructed Doppler tomograms are shown, all on the same grey scale.

It is difficult to reconstruct a clear signature of the tightly wound spiral waves. Except for an enhancement of the disc emission in the top left and lower right, such discs will look very similar to axisymmetric discs, even if high quality data is available. As data quality is degraded the slight variation in the double peak separation with binary phase becomes difficult to measure. I conclude that we do not expect to see obvious evidence of spiral waves in Doppler maps of small, low α accretion discs even if tightly wound spiral waves are present.

¹DOPPLER package developed by Tom Marsh, see <http://www.astro.soton.ac.uk/~trm/software.html>

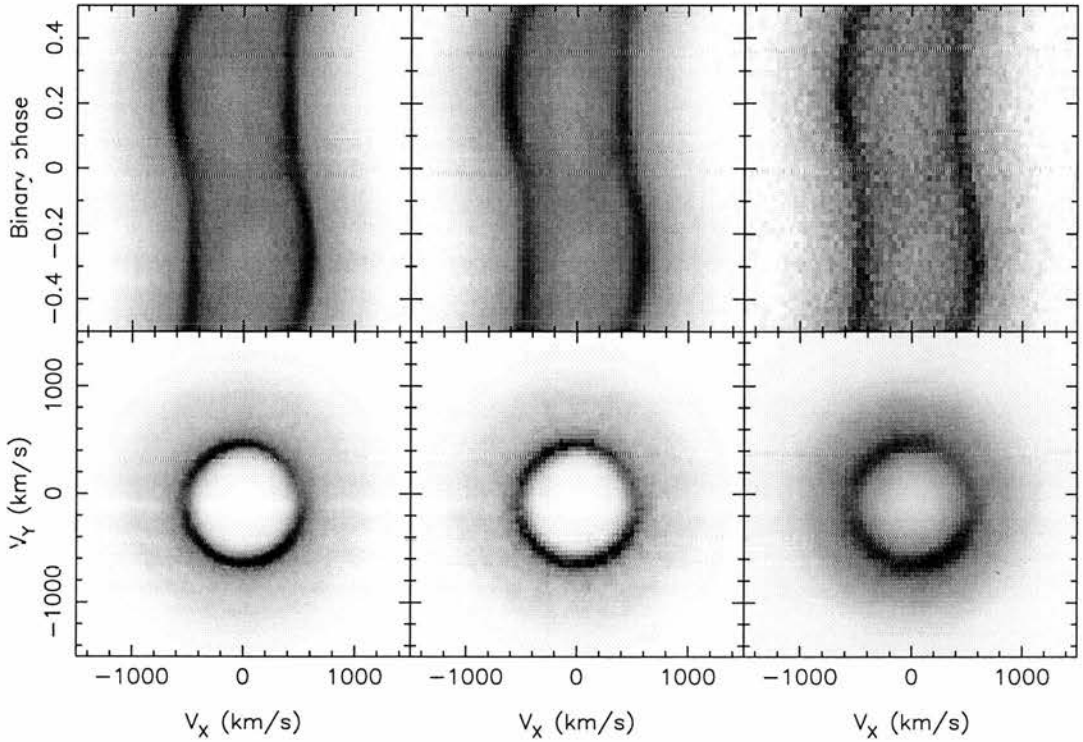


Figure 4.9: Tomograms and trailed spectra of the high Mach number simulation (model I) for a strong emission line. From left to right the 2-pixel wavelength/velocity resolution is (40, 80, 80) km s^{-1} and the ratio of signal to noise is (50, 50, 15) in the continuum.

4.4.3 Low M model

Figure 4.10 plots similar reconstructions now based on model II data. Resolution and signal to noise levels are identical to the previous model for comparison. The strong two armed spiral pattern is readily recovered even at low signal to noise and medium resolution (Fig. 4.10, right). In these large hot discs, the tidal arms dominate the emission lines and are easily visible both in the line profiles directly and in the Doppler tomograms.

To compare the two models, I show the asymmetric part of the reconstructed tomograms on the left most panels in Fig. 4.11. These are obtained by subtracting the median of the image at each velocity, measured from the white dwarf. The low Mach number case shows prominent spiral arms, whereas for model I, only a slight asymmetry is observed. Another way of quantifying this is to plot the velocity and intensity of the spirals as a function of azimuth in the Doppler tomogram. In Figure 4.12, I plot the velocity at which maximum

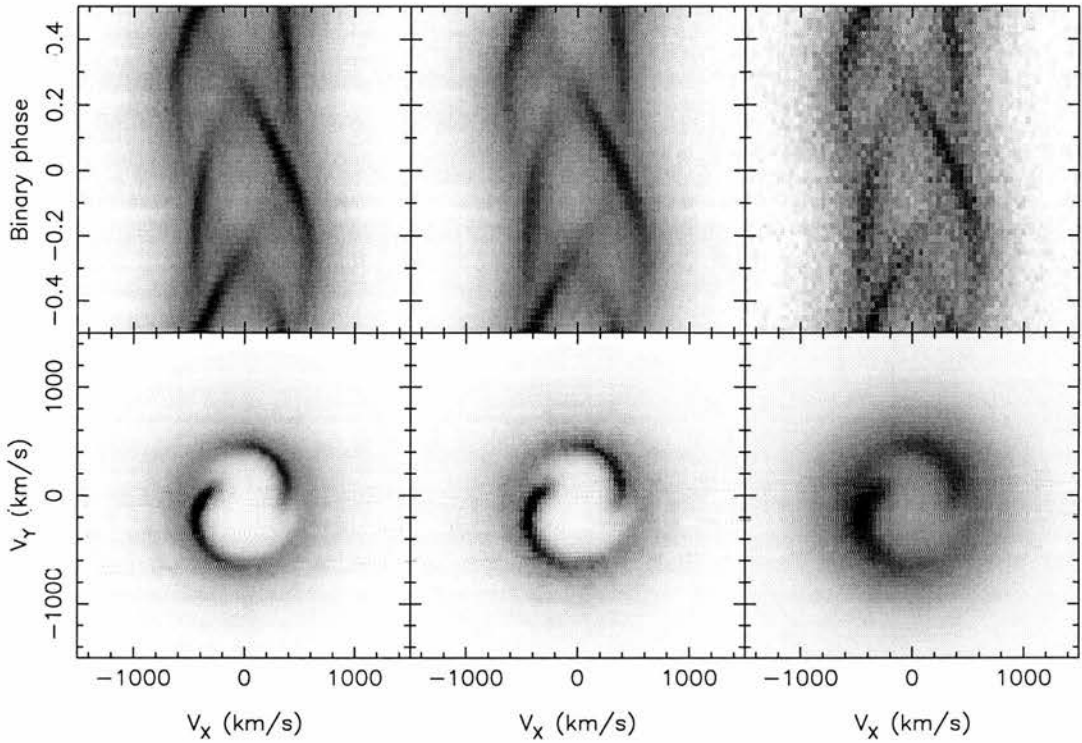


Figure 4.10: *As Fig. 4.9 but for model II*

emission occurs as well as the image value of the maximum at each azimuth, in an identical manner to Figure 3.4 used to analyse the observed tomograms in Chapter 3. The two open spirals in the Model II tomogram span a large range of velocities and emissivities, producing a distinct variation with azimuth. For Model I, this variation is of much smaller amplitude in both velocity and emissivity.

4.4.4 Instrumental requirements

I reconstructed disc images for various signal-to-noise levels, amounts of shear broadening, orbital inclinations and number of binary phases using Model II data. Based on these reconstructions, I found a signal to noise of ~ 15 in the line flux and a two pixel velocity resolution of $\sim 80 \text{ km s}^{-1}$ to be sufficient to convincingly reproduce the two armed pattern on the disc. As we mentioned earlier, to avoid artifacts ~ 50 orbital phases are desired. The instrumental requirements for reconstructing such open spirals are therefore fortunately relatively modest and imply a search for such structure in CV discs is feasible and will provide

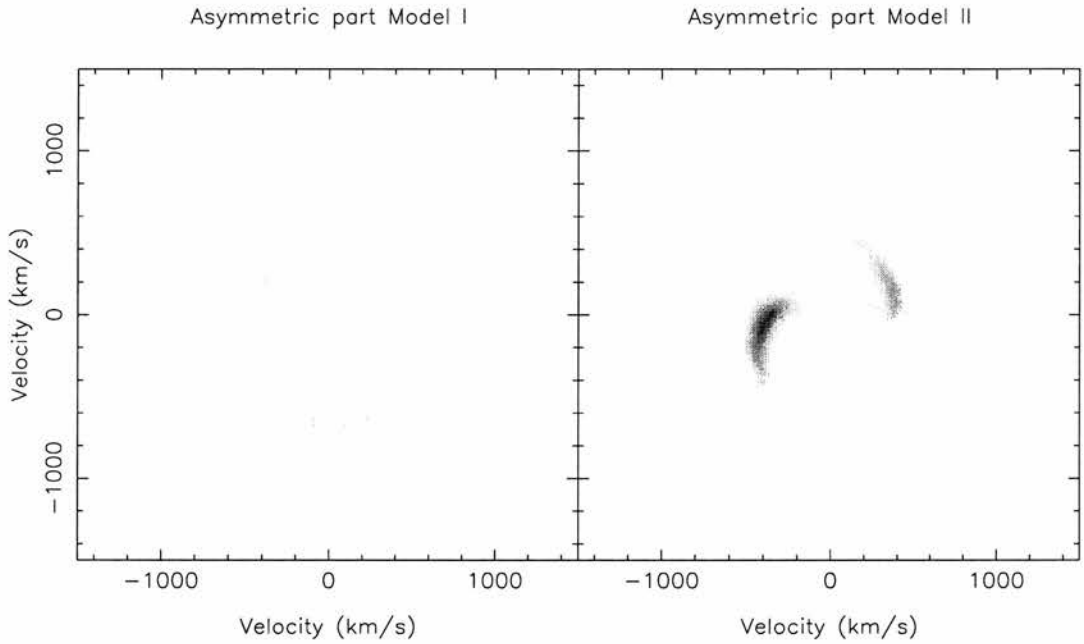


Figure 4.11: *The asymmetric parts of the reconstructed imaged for the two models. The image scales are identical to the full scale of the original Doppler maps, conserving the relative amplitude of the asymmetries. In the high M case (left), only a slight asymmetry is produced in the top left and lower right regions. In the low M case, the image is dominated by the two armed spiral structure.*

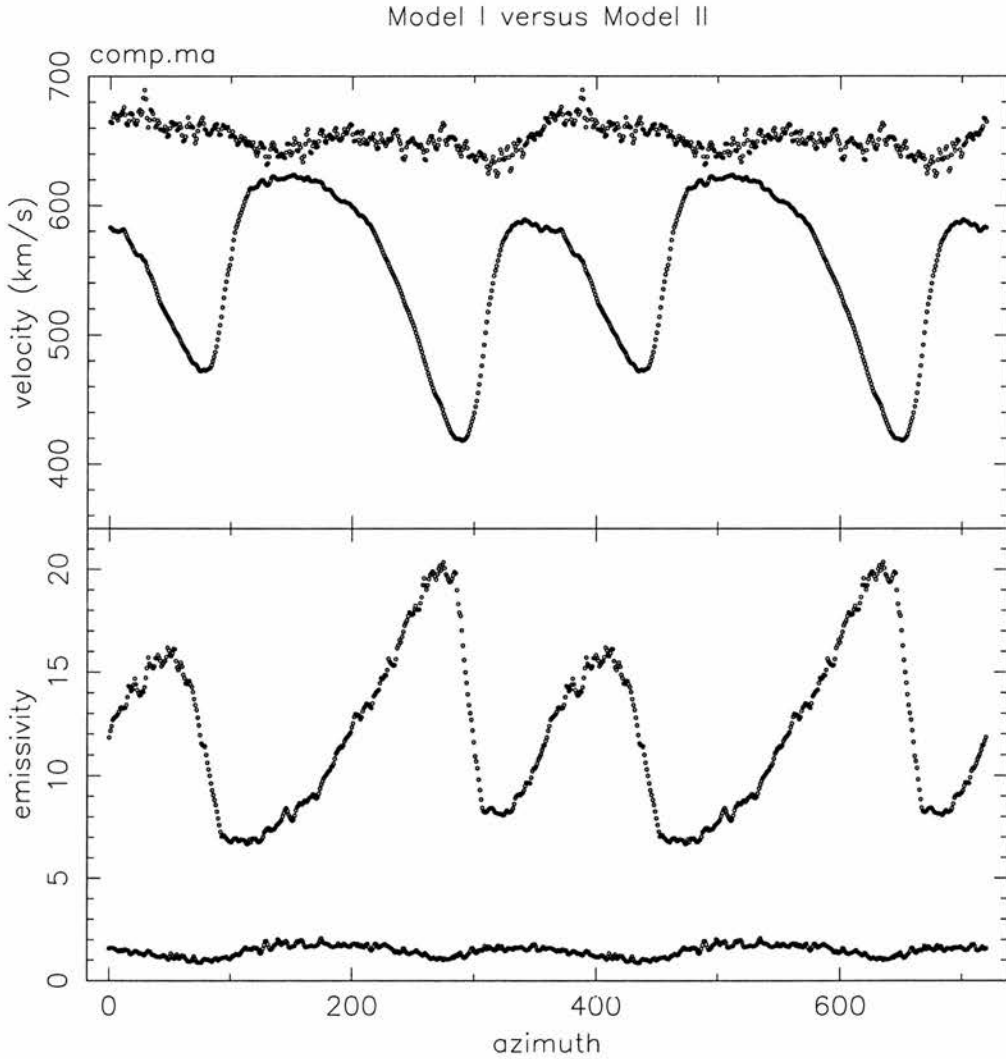


Figure 4.12: *The properties of the disc emission as a function of azimuth. Top panel plots the velocity at which maximum emission occurs (i.e. the spiral arms) for Model I (top) and II. The open spiral pattern in Model II covers a wide range of velocities. The bottom panel plots the image value at the maximum and again in the case of Model II (top curve), a strong azimuthal dependence is visible.*

strong constraints on the presence of spiral waves in these discs.

Figure 4.13 illustrates some of the reconstructions obtained. The two images on the left illustrate the effect of shear broadening on high inclination discs. The disc image is similarly broadened in the case of strong shear broadening but still carries the two armed pattern. Middle panels illustrate the effect of a strong versus weak emission line. This basically lowers the signal to noise of the data and affects the disc image in the same way. Finally the right panels show the strong artifacts due to poor phase sampling (top) or the lack of image structure due to poor spectral resolution.

To show how important the signal to noise is, I plot in Figure 4.14 the properties of the reconstructed spirals as a function of azimuth for the three reconstructions in Figure 4.10. Although the degradation in resolution from 40 to 80 km/s does not severely hamper the reconstruction, a drop in signal to noise makes the reconstructed spiral pattern appear with much lower amplitude and velocity variations across the image. One has to be careful therefore in interpreting the absolute image values in recovered Doppler tomograms in comparison to model predictions. The recovered pattern will be a function of signal to noise, so in order to make a reliable comparison, noise has to be added to the model data before any conclusions can be drawn.

4.4.5 Other emission line sources

Our reconstructed images are those of the accretion disc contribution only. The irradiated companion star, the gas stream and the hot spot are well known other contributors to the emission line flux. In the case of the companion star, its contribution is confined to a Roche lobe shape centered at the radial velocity of the companion, at velocities where no disc emission is expected. More demanding are the stream-disc interactions, which can contribute to a wider range of velocities overlapping the accretion disc, though the compact impact region is usually well defined. Complications also arise due to disc outflows, which can be responsible for the single peaked emission lines observed in some systems. These issues have to be kept in mind when interpreting emission line data sets (e.g. Steeghs, Horne, Marsh & Donati 1996).

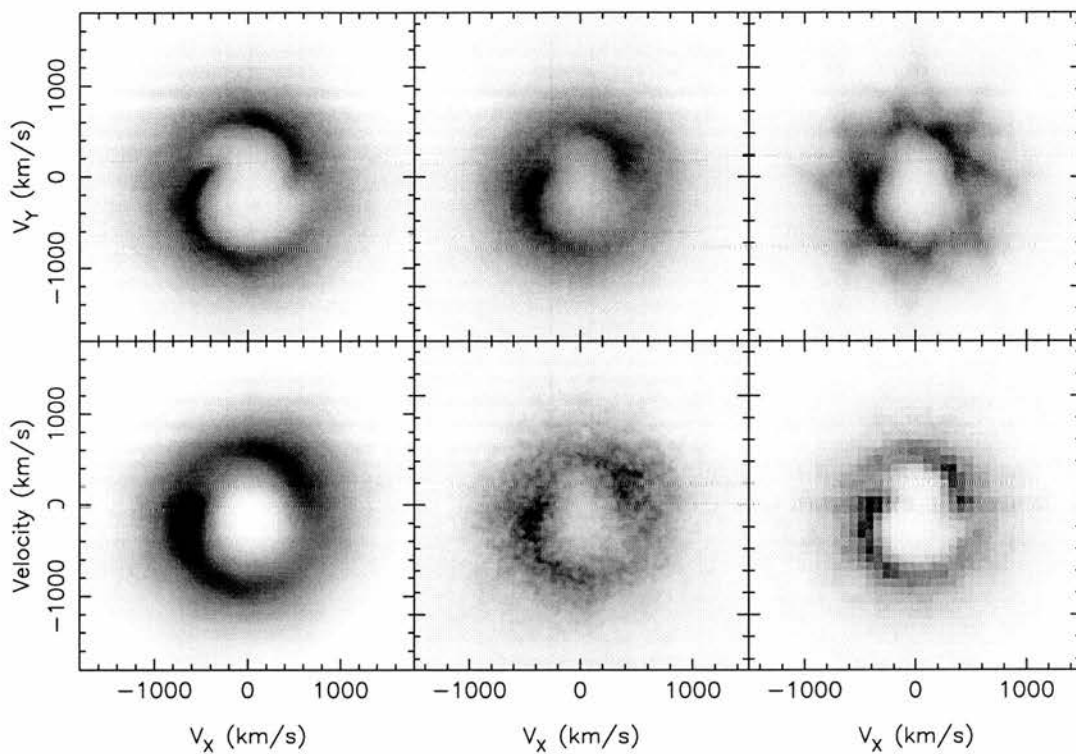


Figure 4.13: *Some example reconstructions for Model II data. Left is the case of high inclination (80°) without (top) and with maximal shear broadening. Middle a reconstruction of a strong emission line (twice the continuum) with a continuum signal to noise of 30 (top) compared to a weak line (15% above continuum) at the same S/N. Top right shows artifacts introduced by poor phase sampling, in this case 10 bins at high signal to noise (50). The bottom right panel shows the effect of insufficient spectral resolution (150 km s^{-1}) to reconstruct the disc structure.*

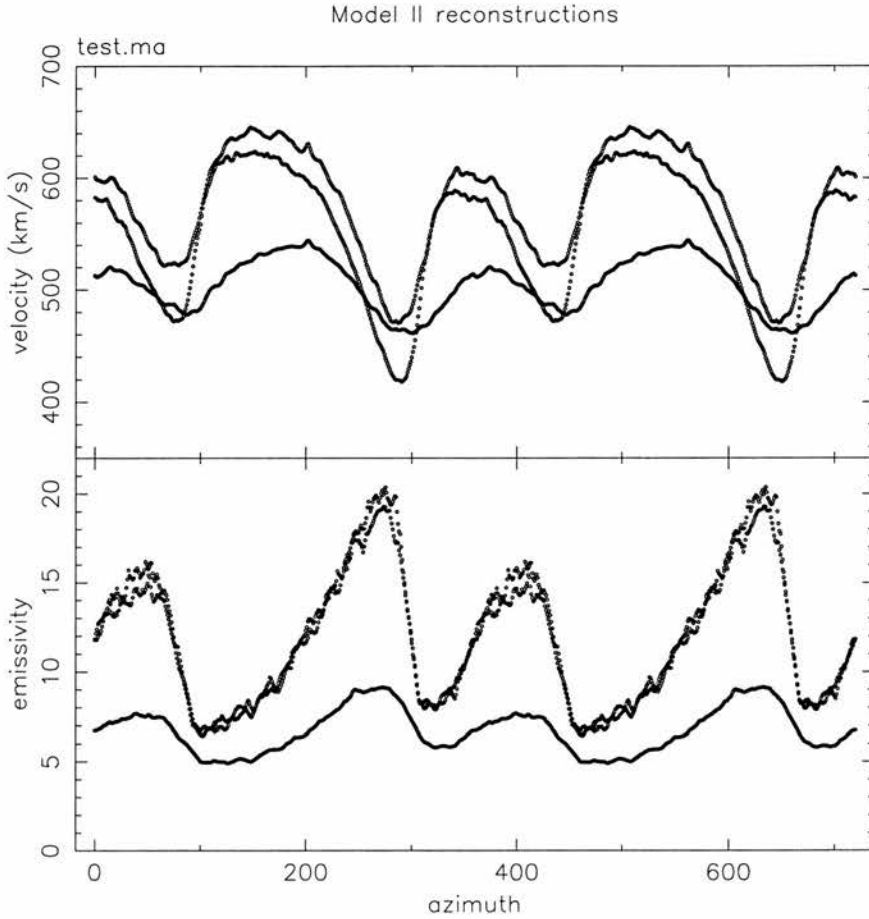


Figure 4.14: A look at the three reconstructions in Figure 4.10. In the top panel the position of the recovered spiral in the tomograms is shown, with the top curve representing the 40 km/s resolution reconstruction, followed by the 80 km/s reconstruction with identical signal to noise. The lowest curve is the reconstruction when the signal to noise was dropped. Similarly, the amplitude of the spirals (bottom panel) is not strongly affected by the resolution (top two curves), but a drop in signal to noise means that the reconstructed amplitude variations are much smaller.

4.5 The influence of spiral waves on light curves

In this chapter I have so far focused our attention on the properties of the emission lines in the presence of spiral density waves in the disc. This section concerns the orbital light curves of high inclination systems carrying spiral density waves.

Bunk, Livio & Verbunt (1990) have already explored the influence of geometric spiral patterns on the shapes of the continuum light curves in eclipsing systems for various shock strengths. I therefore calculated continuum light curves generated from our model simulations to generalise this to realistic disc geometries. Each grid cell is assumed to radiate as a black body corresponding to the local effective temperature :

$$B_{\lambda}(T_{\text{eff}}) = \frac{2 h c^2}{\lambda^5} \frac{1}{\exp(\frac{hc}{kT_{\text{eff}}\lambda}) - 1} \quad (4.10)$$

The visible area $A(x, y)$ of each grid cell is calculated, taking occultations by the companion star into account, in order to calculate the total (monochromatic) disc luminosity L_{λ} as a function of orbital phase:

$$L_{\lambda}(\phi) = \frac{\cos i}{d^2} \int \int B_{\lambda}(T_{\text{eff}}) A(x, y) dx dy \quad (4.11)$$

In Figure 4.15, I plot some eclipses at a few representative wavelengths for both model I and II. All light curves have been normalised to their out of eclipse level for comparison. The Model I light curves are more flat bottomed and narrower compared to the V-shaped eclipse shapes of Model II. This reflects the smaller radius and lower outer disc temperatures in model I. The asymmetries in the light curves are most notable in the near and far UV wavelengths.

To compare these with the light curve of an axi-symmetric, purely Keplerian disc, I plot in Figure 4.16 monochromatic lightcurves for the same wavelength (4000Å) for Model I, II and a Keplerian disc model. The Model I lightcurve is very difficult to distinguish from the Keplerian model. Model II, on the other hand, exhibits much steeper slopes near ingress and egress because of the significant amount of emission in the outer disc. Eclipse mapping

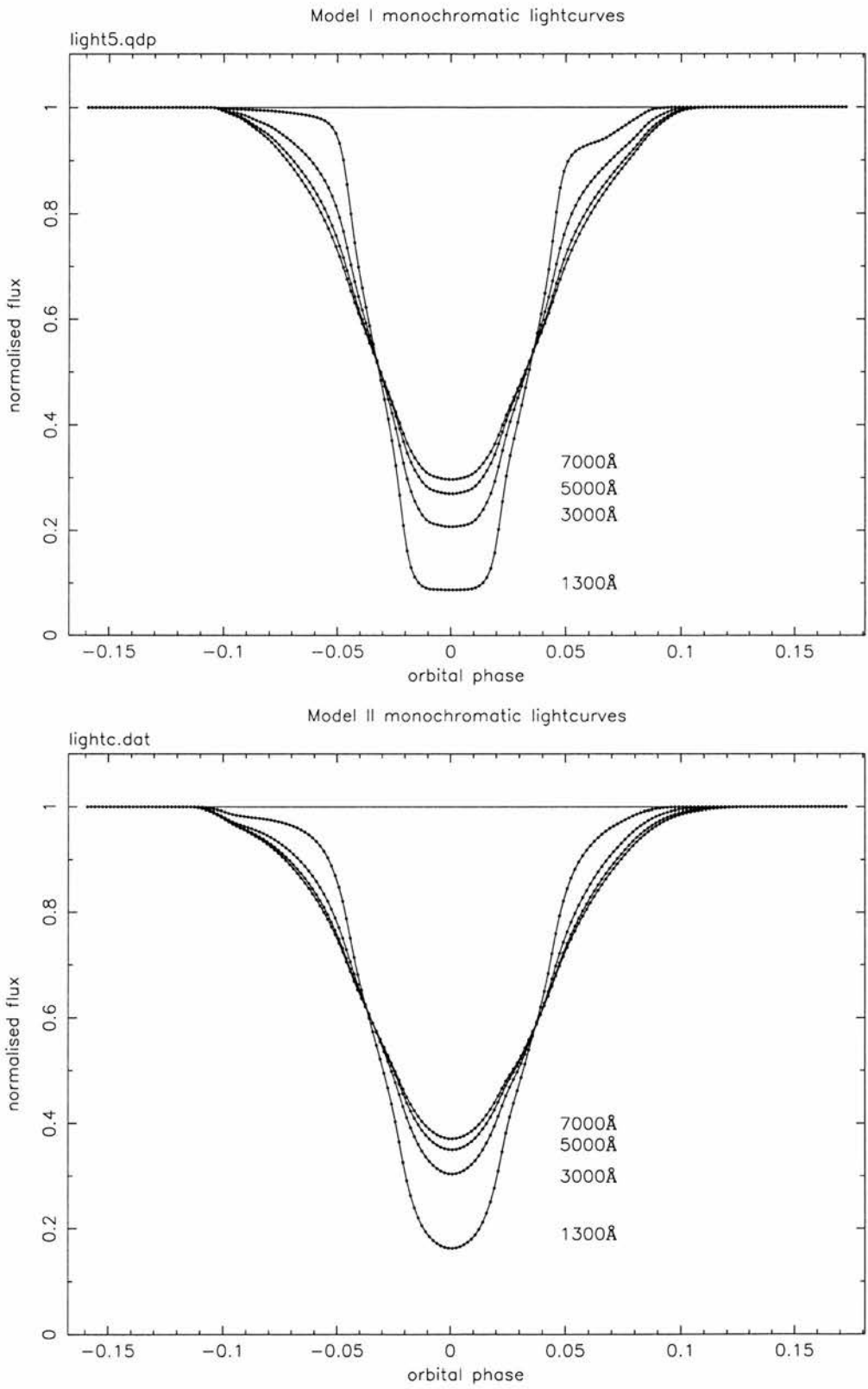


Figure 4.15: Monochromatic continuum light curves for Model I (top) and II at 1300, 3000, 5000 and 7000Å. All light curves are normalised to their out of eclipse levels.

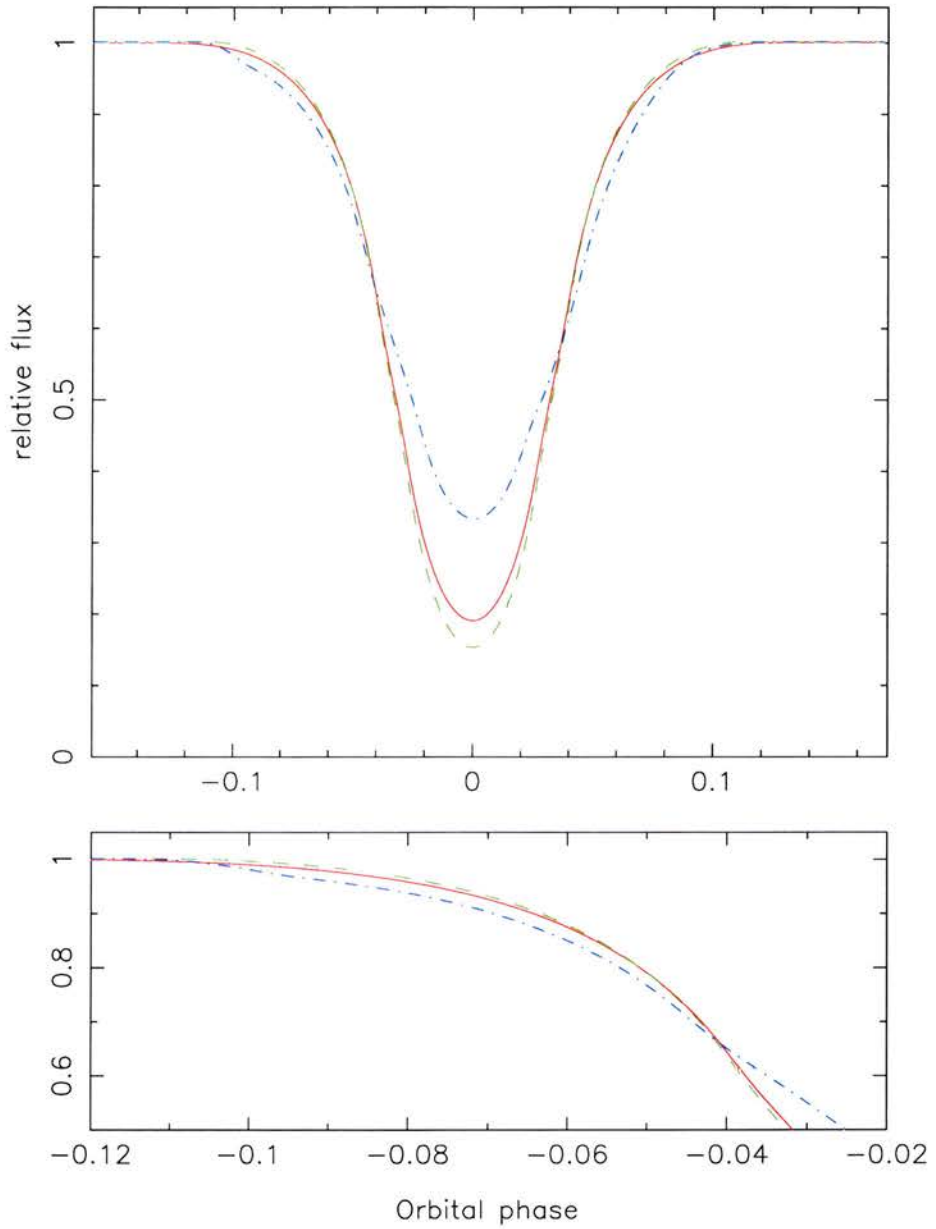


Figure 4.16: *A comparison between the two models and a steady state, Keplerian disc. The solid red curve is the eclipse of a symmetric Keplerian accretion disc. The green dashed curve is Model I and the blue dot-dash curve is Model II. The bottom panel zooms in on the ingress phases, to illustrate the shallow ingress and egress exhibited by the Model II light curve.*

can be applied to model the eclipse shapes in detail but is known to have limited azimuthal resolution to conclusively resolve spiral patterns (see also Baptista, Harlaftis & Steeghs, in press). This confirms the findings of Bunk et al., that moderately strong shocks cause no *unique* features in the optical eclipse light curves. Eclipse lightcurves can assist in the analysis of the continuum distribution across the disc, but are ideally complemented by spectroscopic data to conclusively search for spiral waves in accretion discs.

So far I have assumed that the line emitting gas is not obscured by any structure in the disc itself, only by the Roche lobe filling companion star. In the one-zone treatment of the time dependent disc height $H(x, y, t)$, we can truly assess the validity of this assumption. In the standard steady state picture, hydrostatic equilibrium dictates that the disc thickness is inversely proportional to the azimuthal Mach number. With a temperature profile that monotonically decreases outwards and an azimuthal velocity that increases inwards, this leads to a growing disc height as a function of radius. The disc can then be characterised by an opening angle determined by the disc height at the outer rim; $\theta = \tan^{-1}(H/R)$. Inclinations higher than $90 - \theta$ would then result in obscuration of the inner disc by the outer rim.

In our models, discs are highly asymmetric and the additional treatment of vertical oscillations produces scale heights that locally are significantly different from the steady state counterpart. In Figure 4.17, I plot a radial slice of Model II at azimuth 0.34 (122°). At the position of the spiral waves, the scale height is large and reaches its highest value at the outermost arm, near the disc edge. H/R slowly rises with increasing distance from the white dwarf and reaches a maximum of 0.086 at the outer edge corresponding to an angle of 5° with respect to the white dwarf (dashed line). For inclinations higher than 85° , the outer disc would therefore block the disc completely from view. In order to calculate this properly we would need to evaluate the optical depth at the particular wavelength we are interested in along the line of sight to calculate if the outer spiral blocks the inner disc from view. The effective disc height as defined by the height at which optical depth of $2/3$ is reached could in fact be higher than the scale height H provided the surface density is sufficiently high (Stehle & Steeghs, in preparation). This would cause obscuration of the inner disc by the disc rim at even lower inclinations. The azimuthal dependence of the critical angle will lead to phase dependent modulations in the orbital lightcurves for inclinations close to 85° .

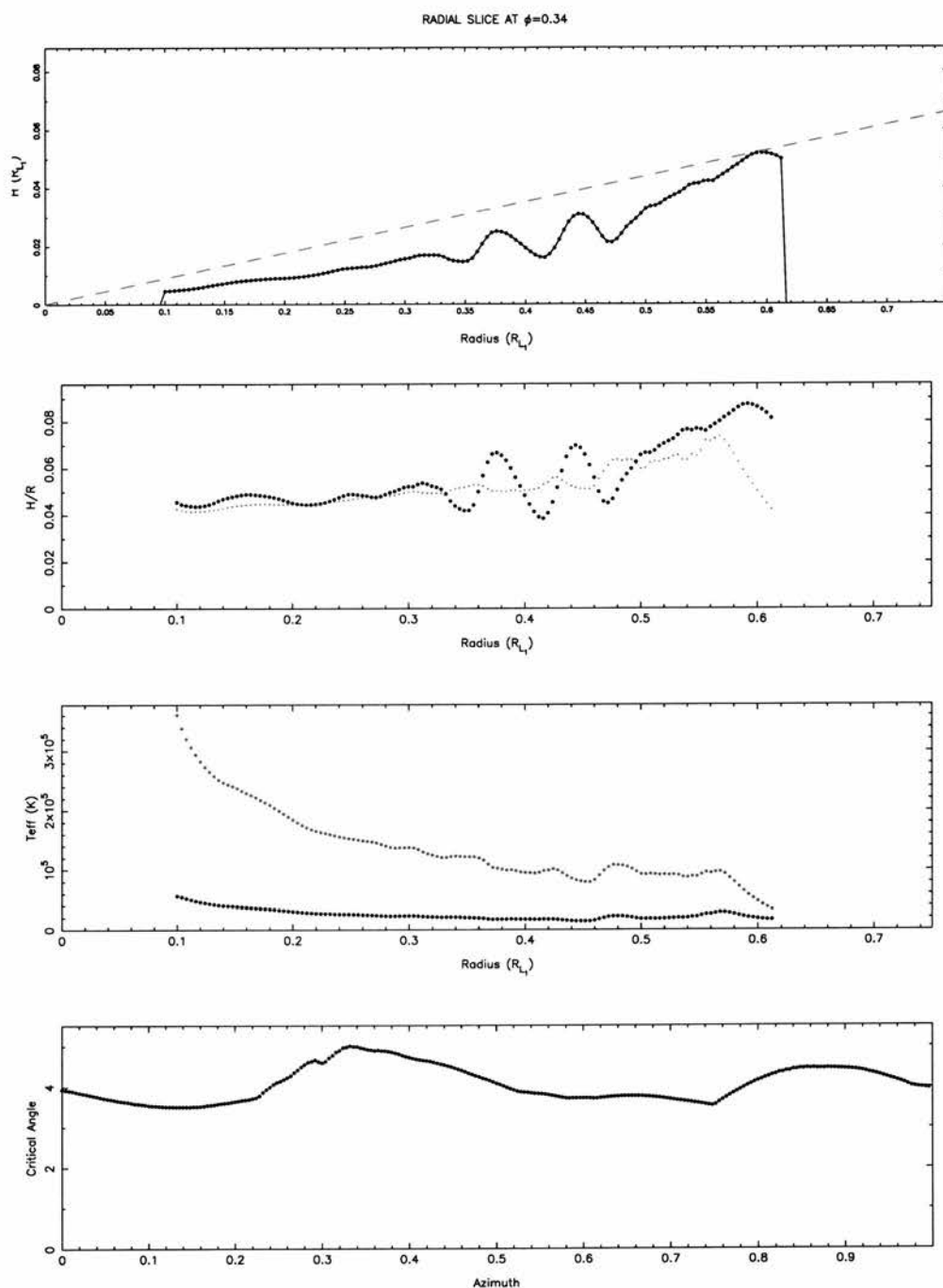


Figure 4.17: A radial slice through the Model II accretion disc at phase 0.34 (azimuth 122°). Top, the disc scale height as derived from the one zone model as a function of radius (black curve). Below it, the relative disc thickness H/R is plotted in black which reaches a maximum of 0.08 at $R=0.6$ corresponding to a critical angle of 5° . Plotted in green is the equilibrium scale height. Below that is the run of effective and central (green) temperature with radius. The bottom panel shows the critical angle (red dashed line in top panel) as a function of phase/azimuth.

Of more importance, and a specific feature due to the presence of tidal waves, is the fact that H/R is not monotonically increasing with radius. The crests of the spiral waves effectively shield part of the disc from view even if the outer rim is not high enough to block the inner disc from view. This will affect a far larger range of orbital inclinations and may provide an indirect measure of the presence of vertical structures in the inner regions of the disc. The sharper the spiral shocks, the more pronounced this effect will be. Work is in progress to perform a proper line tracing to evaluate if the optical depth along each line of sight is sufficient to block part of the disc from view and calculate a self consistent light curve that takes this fully into account (Stehle & Steeghs, in preparation).

The main comment here is that if spiral waves are present throughout the disc, self occultation can change the appearance of accretion discs even for moderately high inclinations ($i > 70$). This could be of particular importance for quiescent discs, where there is no clear signature in the emission lines, but the presence of tightly wrapped spirals can leave an observable signature through self occultation. How severe this effect will be crucially depends on the height at which the continuum and line emission we observe is formed, which is unfortunately a poorly understood process.

4.6 Summary

I have studied the emission line profiles of close binary accretion discs in cases where the disc pattern is dominated by prominent spiral shock arms excited by the tidal forces of the secondary star. As underlying disc models, I used the grid of full hydrodynamic CV disc calculations of Stehle (1999). I modelled the emission lines using the theory of Horne (1995), including the effect of shear broadening for saturated lines. Doppler tomograms and trailing spectra were constructed and instrumental effects were included to assess the data quality required to reconstruct spiral structure in CV discs.

I found that for high Mach number discs ($M = v_\phi/c_s \simeq 15 - 30$) the spiral shock arms are too tightly wound to leave significant fingerprints in the emission line structure of these small discs. As a result the peak separation of the double peaked emission line profiles varies by only $\sim 8\%$ with binary phase. I therefore do not expect to detect strong spiral arms in

quiescent CV discs. Sensitive metal lines such as Calcium may provide important insights into the properties of tightly wound spiral waves because of their sensitivity to velocity dispersion.

For low Mach number discs ($M \simeq 5 - 20$), i.e. for CV accretion discs in outburst, the line emissivity is dominated by the spiral shock arms. The two armed spiral pattern is identified by the presence of converging peaks in the line profiles. This signature in the trailed spectrum is expected to be sufficiently prominent that a signal to noise of ~ 15 per pixel, a wavelength resolution of $\sim 80 \text{ km s}^{-1}$ and a time resolution of 50 spectra per binary orbit is sufficient to verify the presence of spiral shock arms in binary accretion discs through Doppler tomography of strong emission lines.

Our simulations successfully reproduce the emission line properties of the disc structure observed in IP Pegasi. The detection of strong two armed spiral structure in outburst (Steehgs et al. 1997), but no clear disc structure in quiescence (Marsh & Horne 1990), is convincingly reproduced by tidal spiral waves in the accretion disc.

I do not expect a strong signature of spiral arms in broadband light curves unless self occultation is important. Eclipse light curves alone will not provide a unique signature that can point to spiral arms. Indirectly, however, through self occultation, the presence of spiral waves will produce out of eclipse variations and even change the apparent temperature profile of the disc as inferred from eclipses.

The prospect of a new way to probe the local physics of discs through the dynamics of these tidal spirals demands more observational efforts on the detailed properties of high-mass transfer accretion discs through indirect imaging.

CHAPTER 5

Comparing theory and observations

In this Chapter I compare the accretion disc structure as observed in IP Pegasi and other CVs to the latest theoretical efforts regarding the tidal response of accretion discs in semi-detached binaries.

5.1 The spiral wave interpretation of the disc in IP Pegasi

The presence of a highly distorted accretion disc in the CV IP Pegasi during its outburst, has been demonstrated in Chapter 3 and also in Morales & Marsh (1999). These observations covered the start, middle and end phases of the outburst maximum, indicating that the spiral pattern is persistent over at least 8 days. Eclipse mapping furthermore reveals that the spirals make a substantial contribution to the continuum light (Baptista et al., in preparation), which suggests that the physical structure responsible for the spiral pattern is not confined to a thin disc atmosphere only. Other evidence for an asymmetric disc in IP Pegasi was reported by Piché & Szkody (1989), who note that their outburst data of IP Peg is not compatible with a symmetric Keplerian disc, but no disc image is available. Similarly, Hessman (1989) reports measurements of the emission line peak velocities of IP Pegasi at the end of an outburst which shows a phase dependence that suggests a strong asymmetry in the outer disc persists well into the outburst, though is much weaker than in the initial phases.

With this spiral structure confirmed in several epochs and a wide range of emission

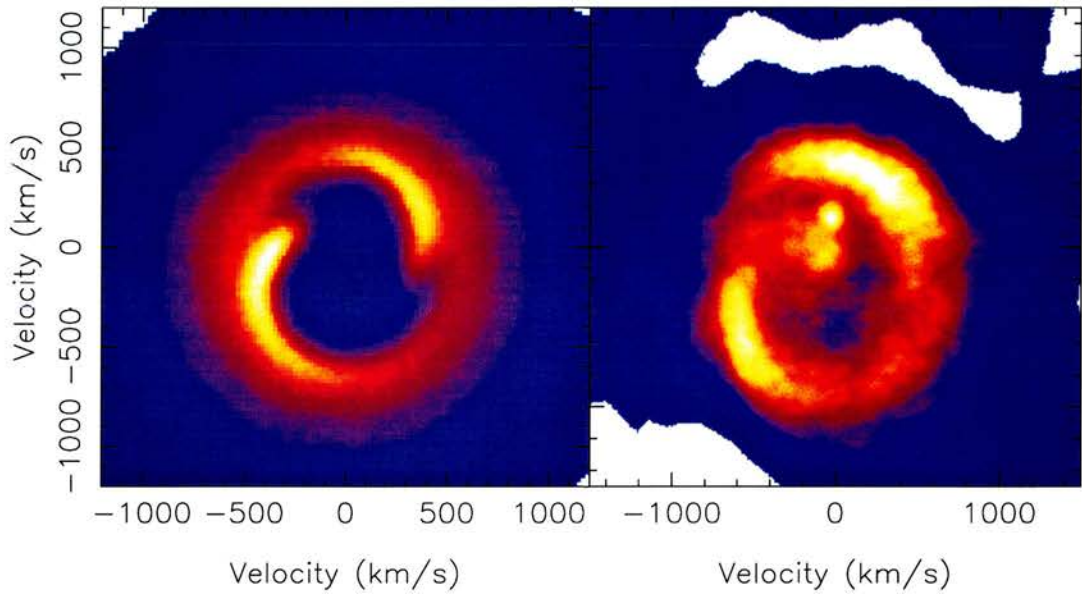


Figure 5.1: *Left is a Doppler tomogram reconstructed from emission line data calculated from a hydro-dynamical disc simulation of a large disc carrying a two armed spiral pattern. Right panel, the observed Doppler tomogram of the HeII 4686 emission from IP Pegasi in outburst. Apart from the disc emission there is also secondary star emission and low velocity emission observed in the inner regions of the tomograms that are not included in the model calculation. Doppler tomograms naturally separate the two and allows easy comparison between theory and observation.*

lines, we can now be confident that this pattern is a genuine feature of the accretion disc during outburst. Its persistence in the co-rotating frame of the binary system also indicates that it is most likely a tidally driven phenomenon that is the cause of the observed asymmetries. This is furthermore supported by observations during quiescence, when tidal forces on the smaller disc have decreased and the spiral pattern is not observed.

The simulated Doppler images and line profiles presented in Chapter 4 confirm that the observed disc structure can be reproduced by tidally excited spiral arms in the disc. The observed presence of a dominating two armed structure in outburst, when the disc is hot and large, compared to a fairly symmetric disc in quiescence matches extremely well with the model predictions presented in Chapter 4. Figure 5.1 plots the observed Doppler image of the HeII emission from IP Pegasi during outburst, together with the predicted Doppler

image of an accretion disc with a two armed spiral pattern. Whereas no attempt has been made to make a fit to the data, the spirals match in detail.

Armitage & Murray (1998) reach a similar conclusion based on 3-D smoothed particle hydrodynamics (SPH) simulations of the disc flow in IP Pegasi. A spiral density pattern, matching the kinematics of the observations, is formed when the shear viscosity is increased and the disc expands. However, these arms appear to be transient on a viscous time scale in their simulations. In the models of Stehle (1999) used in Chapter 4, the spiral pattern is stable in the co rotating frame, though its properties will change as the outburst progresses and especially when the cooling wave propagates through the disc and changes its temperature structure. Since the pattern is observed to be persistent up to at least 8 days into the outburst, we are already in a position to test the predictions of such numerical simulations on a long time scale and conclude that some adjustments need to be made to the work by Armitage & Murray (1998) to produce a persistent spiral structure.

Godon, Livio & Lubow (1998) presented 2-D disc simulations using Fourier–Chebyshev spectral methods. They attempted to reproduce the observations of IP Pegasi. They found, however, that the spiral pattern resembles the observations only for very high temperatures since the opening angle of the spiral pattern grows with increasing temperature. The α values used were rather low ($\alpha = 0.1$ at most) and thus viscous spreading was less efficient compared to our simulations. As a consequence, their discs were smaller by up to $\sim 50\%$ compared to our model II simulation. Their results thus support our calculations in Chapter 4, that small discs produce tightly wound spiral arms and that it is essential to push the disc to large radii to produce an open spiral pattern as observed.

Matsuda et al. (1999) presented both 2D finite difference as well as SPH simulations and compared the results with the IP Pegasi observations. Both types of simulations produced identical results and the density distributions corresponded well with the observations, provided the disc was fairly hot (Figure 5.2). Boffin, Haraguchi & Matsuda (1998) performed 3D SPH simulations with and without mass inflow to examine the properties of the spiral arms as a function of disc temperature (i.e. the polytropic index γ). In the inner parts of the disc, the $\gamma = 1.2$ (hotter) simulation results in more openly wound spirals compared to, for example, $\gamma = 1.01$, a familiar result from previous studies. However, no clear distinction in

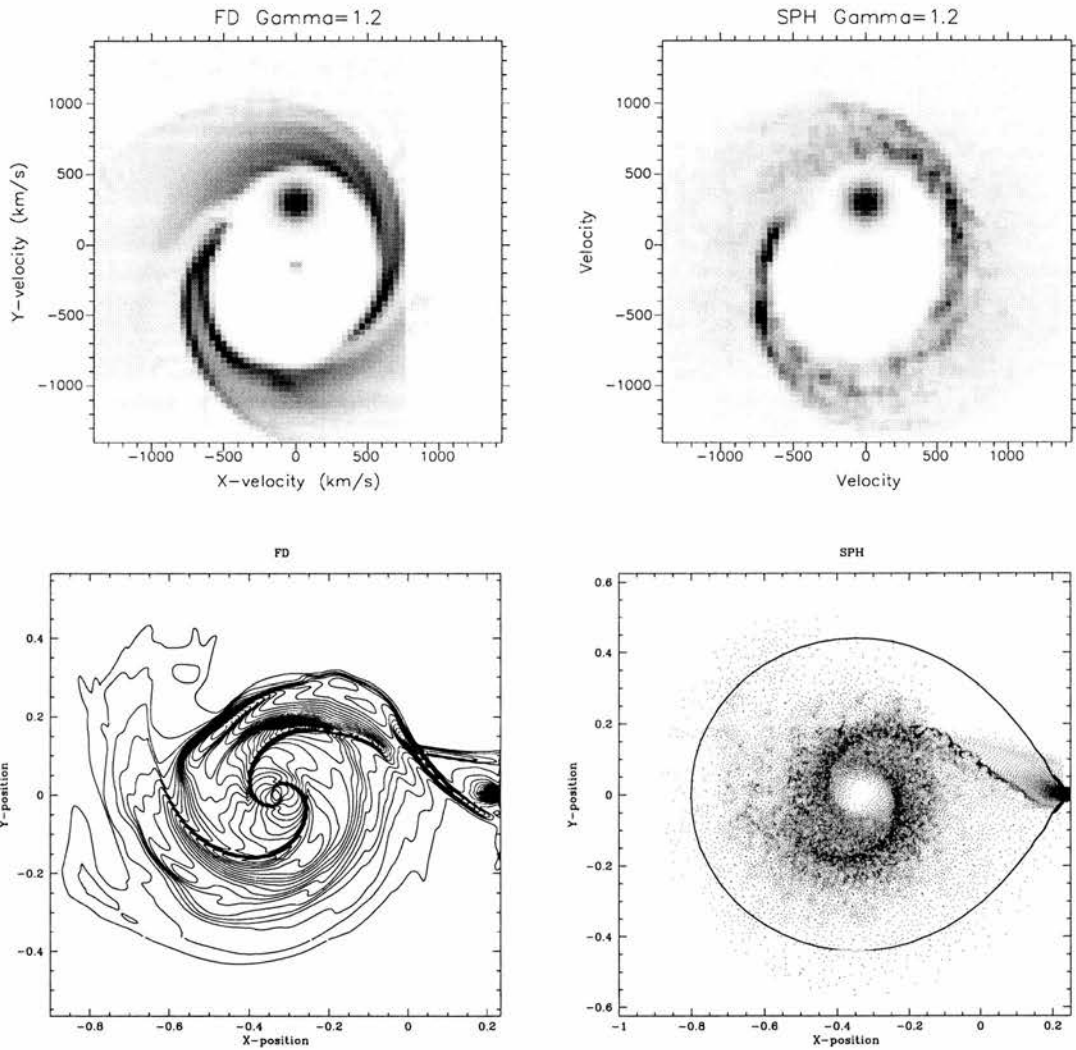


Figure 5.2: Comparison of finite difference and SPH simulations by Matsuda et al. (1998). Bottom left, the density distribution of the finite difference result, with the corresponding Doppler tomogram above it. On the right the particle plot of the SPH result, and its tomogram.

the opening angle is apparent in the outer parts of the disc, indicating that the Mach number is not the only factor determining the geometry of the spiral waves, particularly in the outer disc.

A consistent picture can be drawn from these recent theoretical efforts in understanding the observed disc structure in IP Pegasi. A spiral pattern that fits the properties of the observed spirals in detail is produced, provided the accretion disc is large enough to trigger a sufficiently strong tidal response. For small, cool discs, tightly wrapped spiral waves are expected, that unfortunately leave no strong fingerprints in the emission lines of CVs. We therefore expect the properties of the spirals to change radically across the outburst cycle as the disc expands/contracts and heats up/cool. Doppler tomography across the outburst cycles of dwarf novae will allow us to construct a movie of the accretion disc structure. This would be a unique way to witness the effects of density waves in real-time.

In the standard thermal disc instability scenario, it is the heating wave that switches the disc from a low to a high viscosity state. The larger local shear viscosity pushes the disc to larger radii as angular momentum transport is enhanced. In the model of Armitage & Murray (1998), the spiral arms are then generated as a transient phenomena *after* the viscosity has switched to a higher level. In the models of Stehle (1999) spiral waves are always present but the tightly wrapped spiral waves open up and grow in strength as the disc expands when the shear viscosity is increased. Although spiral waves can transport angular momentum, it appears *there is still a need for a second, co-existing angular momentum transport mechanism which increases its efficiency during outburst and pushes the disc to sufficiently large radii.*

It is not yet established from observations if the spiral waves are only confined to the outer disc, or travel all the way inwards, which has large implications for the relevance of spiral waves to the overall angular momentum transport throughout the disc. The presence of tidally driven spiral waves and associated density wave angular momentum transport does therefor not rule out the presence of local α -type viscosity mechanisms, or the disc instability mechanism. It is the interplay between local viscous processes and tidally driven waves that determines the global dynamics of the accretion disc. In this way spiral waves are not only a diagnostic of the importance of density waves in accretion discs, they can also help us to constrain the properties of the local disc viscosity. Comparison of disc simulations for various

prescriptions of the shear viscosity with the observed disc evolution during the outburst cycle, can in this way yield a more workable treatment of the local shear viscosity and even rule out some viscosity mechanisms. This is an exciting prospect as the theoretical modeling of the structure of accretion discs matures in realism. It does mean that in order to appreciate the structure of time dependent accretion discs, a 2 or 3 dimensional treatment is essential.

The crucial question remains how much of the angular momentum transport is driven by such tidal waves. We discussed in Chapter 1 the difficulties in quantifying this. It is promising that as simulations become more realistic, they produce more efficient wave angular momentum transport (e.g. Stehle 1998). Since the magnitude of the tidal forces are a strong function of radius (e.g. Ichikawa & Osaki 1994), the associated angular momentum transport by tidally driven waves will similarly depend strongly on radius (e.g. Savonije et al. 1994). The relative contribution of spiral wave angular momentum transport and viscous angular momentum transport will therefore be a function of disc radius, i.e. it will vary dramatically across the outburst cycle in dwarf novae. Chapters 3 and 4 have demonstrated that we now have for the first time the prospect of directly testing model predictions versus observations of the spiral waves in CVs. Using hydro-dynamical simulations on the one hand, where we can control the contribution of the various processes to the ongoing mass accretion, and disc images from observed spirals on the other hand we will be able to address this question more conclusively in the near future.

I have so far focused on the dwarf nova IP Pegasi, where strong observational evidence for spiral waves is available. However, the formation of tidally driven waves is a generic feature of accretion discs in binary potentials. I concluded that it is essential that the disc is large enough to trigger an open spiral pattern that can be observed using the strong emission lines. This situation applies to all dwarf novae during outburst and the nova-like systems, whose high mass transfer rate discs are thought to resemble the discs of dwarf novae in outburst. As long as the inclination is high enough to ensure that double-peaked emission lines are produced during outburst, a large number of objects are expected to show signs of tidal waves in their emission line profiles similar to IP Pegasi. Qualitative differences are expected though for low mass ratio systems ($q < 0.3$), where an $m = 1$ mode can be excited as the 3:2 Lindblad resonance enters the disc (Lubow 1991a). Simulations have been performed

that lead to precessing, elliptical discs that can then be interpreted as the cause of the super-humps observed only in these low mass ratio systems (Whitehurst 1988, Lubow 1981b, Murray 1996,1998). However other simulations (e.g. Heemskerk 1994, Larwood 1997, Stehle 1999), find that the disc is unable to excite this elliptical mode. In many of these latter simulations, spirals are formed instead. Again this is an area where better observational inputs are required to constrain the interplay between tidal and viscous forces in CV discs.

5.2 Is IP Pegasi alone?

In this section I will review observational evidence for the presence of spiral arms in systems other than IP Pegasi. I will focus on data sets where phase resolved data with sufficient quality is available to compare the observed emission line properties with the simulation predictions explored in Chapter 4. I do not intend to provide a complete overview of previous spectroscopic studies of CVs, but aim to cover those that are relevant to the issue of spiral density waves in CV discs. For obvious reasons, phase resolved spectroscopy data sets during outbursts are rare. Most data sets that cover the outburst only provide snapshot spectra which allows one to track the spectral transitions across the cycle (e.g. Hessman et al. 1984).

The first class of systems where spiral patterns are expected are the dwarf novae during outburst, and in particular those above the period gap. Marsh et al. (1990) present Doppler tomograms of the dwarf nova *U Gem* in quiescence, which features a symmetric disc and an extended bright spot. This is similar to the IP Pegasi case, where no evidence is visible for spiral waves during quiescence because they are too tightly wrapped in the cool, small disc. Kaitchuck et al. (1994) present two additional $H\beta$ Doppler tomograms for *U Gem* at quiescent epochs. Bright spot emission is absent and the disc emission is non-uniform. Good quality phase resolved optical data in outburst is unfortunately lacking for this well studied system.

Martinez-Pais et al. (1994, 1996) discuss quiescent and outburst observations of the dwarf nova *SS Cygni*. The emission line trailed spectrograms show a strong S-wave from the secondary as well as double peaked disc emission. The disc emission is not uniform, the two peaks show a strong phase dependence indicating a large asymmetry in the disc, even in

quiescence. The low velocity of the double peaks in the emission lines indicates sub-Keplerian velocities in the outer disc. This was also noted by Echevarria et al. (1989) just after decline from outburst.

Doppler tomography of SS Cyg during outburst maximum (Steeeghs et al. 1996) shows a highly non-axisymmetric disc, with enhanced emission in the top right and lower left quadrants of the tomograms. We have recomputed the Doppler maps from this data set using a maximum entropy reconstruction as compared to the filtered back-projection that was presented in the paper. Figure 5.3 plots the HeII 4686 and HeI 6678 trailed spectrograms together with the tomograms. We first note that there are no major differences between the back-projected maps and those reconstructed using maximum entropy regularisation exist, as expected. The disc emission is clearly non-uniform producing emission line peaks that vary in velocity and intensity across the orbit. The emission line behaviour resembles the two prominent arcs observed in IP Pegasi, but it is however not a close match (see for example Figure 4.5 for a predicted trailed spectrogram of an intermediate inclination disc with spiral arms). Two areas of enhanced emission are visible, but they do not form clear extended arms like in IP Pegasi. Perhaps a more realistic model for the formation of the emission line is needed in order to compare the emission lines from a high inclination disc (IP Pegasi) with that of a low inclination system such as SS Cyg. In the low inclination case, we are looking deeper into the disc atmosphere. One example of this are the broad absorption wings present in the Balmer lines of SS Cyg arising from the optically thick inner disc, whereas in IP Pegasi the Balmer lines are pure emission lines. Doppler tomography of quiescent data can reveal how much of this asymmetry persists into quiescence. As mentioned before, we expect the tidally driven spiral waves to wrap up when the disc shrinks back to its quiescent size.

Billington, Marsh & Dhillon (1996) present phase resolved spectroscopy of the eclipsing dwarf nova *EX Dra* (HS1804+6753). *EX Dra* and *IP Peg* are the only known eclipsing dwarf novae above the period gap. The $H\alpha$ spectrogram is unusual for a high inclination system, as it is difficult to identify the double peaks from the disc at all phases due to a broad bright spot. The tomogram resolves an extended spot along the ballistic trajectory of the gas stream as well as extended emission from the secondary star and weak emission from a small disc. Doppler tomography of the system during outburst reveals the presence of spiral

SS CYG HeII 4686

SS CYG HeI 6678

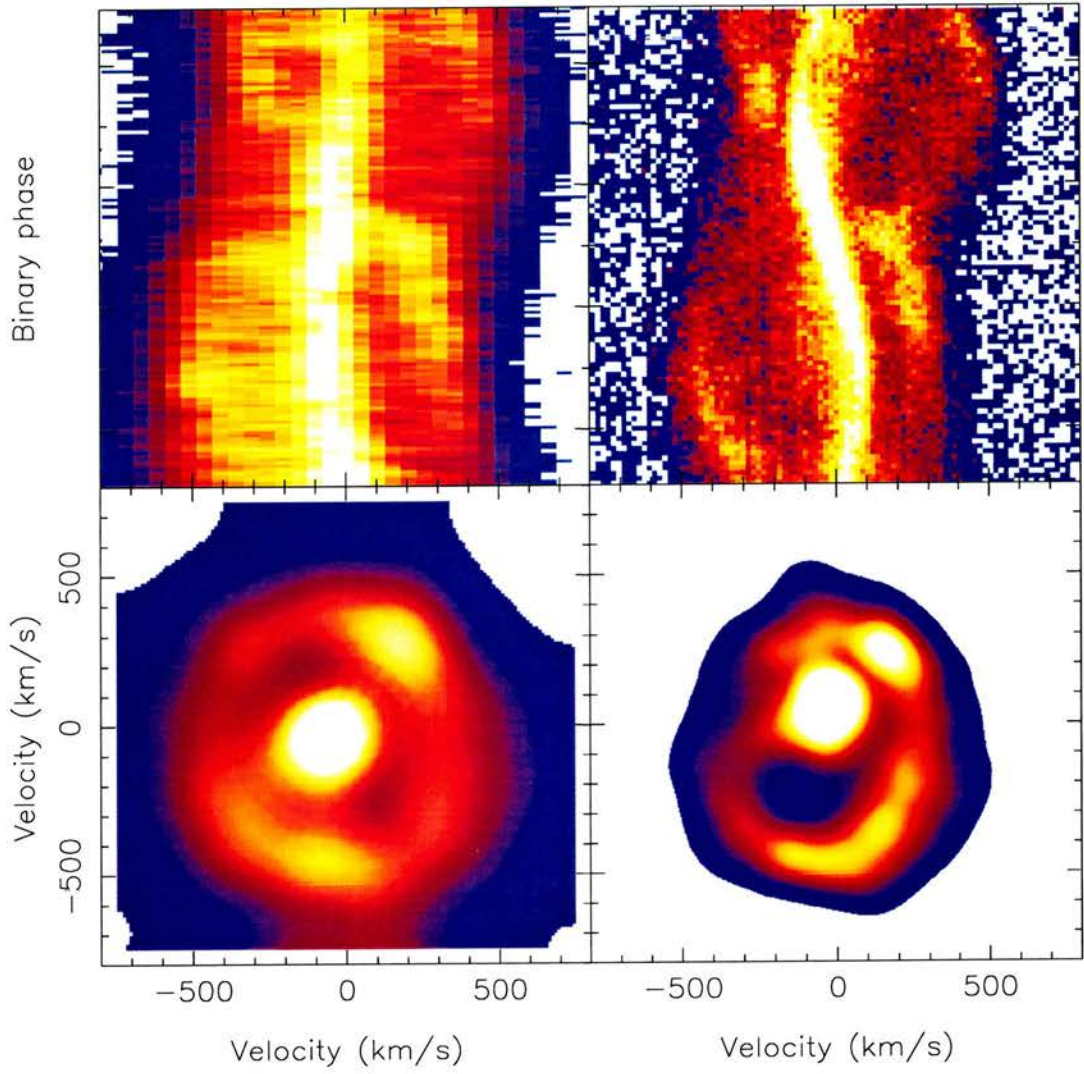


Figure 5.3: *SS Cygni* in outburst. The HeII 4686 and HeI 6678 observations from Steeghs et al. (1996) were used to calculate maximum entropy Doppler tomograms (bottom).

shaped arms most notably in the HeI 6678 emission profiles (Spruit 1999). These spirals are indeed very similar to those found in IP Pegasi and provide the most convincing evidence so far for spiral arms in a system other than IP Pegasi. Further support is given by eclipse mapping throughout the outburst cycle by Baptista & Catalan (1999). During the bright phases, a large amount of emission arises from the outer disc regions, producing a ring of emission in the eclipse maps. Such a ring is expected if spirals are present since the eclipse mapping is not able to resolve the spirals themselves, but produces a ring to reflect the extra emission originating from the spirals in the outer disc. The short outburst recurrence time of 23 days makes EX Dra an ideal target for time lapsed tomography throughout the outburst cycle during an intensive observing campaign.

For the systems below the period gap I have already remarked that some difference might be expected since these discs may be prone to precession. However, for example, Stehle (1999) finds prominent spiral arms even in low mass ratio systems when simulating outbursts. Observations of *OY Car* at the very end of a super outburst indicate a non circular and precessing disc (Hessman et al. 1992). O'Donoghue (1990) resolved the source of the super humps in *Z Cha* using maximum entropy eclipse deconvolution to be at the rim of the disc. The super hump light is distributed among two arcs on opposite sides of the disc and at the outer edge of the disc near the L1 point. Doppler tomography of the disc in *OY Car* during a normal outburst (Harlaftis & Marsh 1996) shows some evidence for the gas stream and its impact on the disc, but no obvious spiral disc structure. With only a few data sets to compare, it is too early to conclude that a systematic difference exists between the SU UMa systems and the longer period dwarf novae, though evidence for spiral waves in other dwarf novae is so far confined to the longer period systems.

Finally, nova-like variables provide permanent high mass transfer accretion discs, and we would therefore expect tidal structures to be important. Unfortunately the emission lines from these systems are poorly understood (Warner 1995, Dhillon 1996, Horne 1998). The lines are single peaked and contain S-wave components of unknown origin. Kaitchuck et al. (1994) published an atlas of Doppler tomograms of many CVs, most of them nova-likes. The problem is illustrated well as most of them show peculiar single peaked emission profiles and no evidence for an accretion disc in the tomograms. The exception appears to be *V347 Pup*,

V347 Puppis H β

V347 Puppis HeI 4921

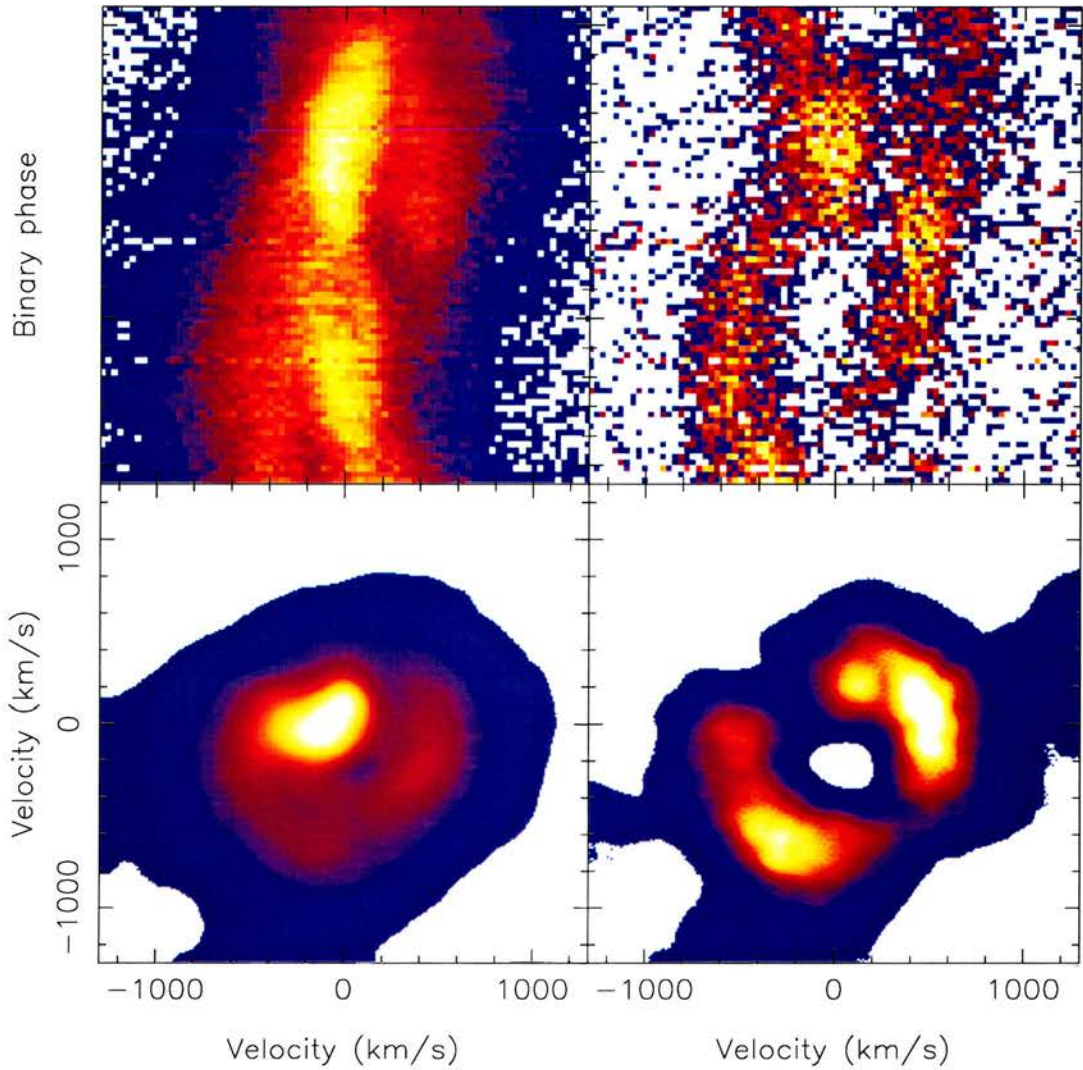


Figure 5.4: *The CV V347 Puppis is one of the few nova-like systems that exhibit clear evidence for disc emission. Top are observed H β and HeI $\lambda 4921$ emission line profiles obtained with the 1.9m SAAO telescope in January 1998. The H β line is dominated by a strong spot of emission and is remarkably different from the data presented by Still et al. (1998). The HeI line on the other hand show two arcs of emission originating from the accretion disc.*

the only eclipsing nova-like variable with clear double peaked emission line profiles originating in the disc (Still, Buckley & Garlick 1998). The Balmer line tomogram shows disc emission confined to the top right and lower left quadrants, where spiral waves are expected. The dominance of disc emission in the line profiles makes this one of the rare cases where one can study a high mass transfer disc in detail. Unfortunately, follow-up observations using the 1.9m Radcliffe telescope at SAAO revealed a very different structure in the Balmer lines in 1998 (Figure 5.4, left). However, the weak HeI emission lines were free of unusual emission components and instead showed clear disc emission, again confined to the arcs in the top right and lower left (Figure 5.4, right). A more thorough discussion of these observations is in preparation (Steeghs, Still, Dhillon & Buckley 1999). High signal to noise data of this system would allow us to construct reliable Doppler tomograms of these weak lines and make a comparison with disc simulations.

Marsh & Dhillon (1997) measured the local line broadening present in 20 CVs exploiting the near coincidence of the CaII H line with the HeI line. This study was motivated by the need to invoke supersonic line broadening to fit to the HST spectra of the dwarf nova OY Car (Horne et al. 1994). They found that for all quiescent dwarf novae observed, significant supersonic line broadening was required. If density waves are present in quiescent accretion discs, we have a natural process that produces a large velocity gradient along the line of sight due to the velocity jump associated with a spiral shock. Each line of sight in a high inclination system passes through several waves which leads to a large total velocity dispersion. Phase resolved spectroscopy of high atomic weight lines may in this way offer an opportunity to quantify the velocity structure of spiral waves in quiescence.

I have discussed the properties of CV discs since these are still the best laboratories to study the properties of thin, α type accretion discs where most heating is due to viscous dissipation. In particular, high quality spectroscopic studies of dwarf novae throughout their outburst cycles are invaluable in understanding the physics of thin accretion discs. It is important to confirm with further observations that the spiral density distribution in close binary accretion discs is a common phenomenon and during which states they can be observed.

The significance of tidal waves in the discs of X-ray binaries (Blondin & Owen 1997; Owen & Blondin 1997; Lanzafame & Belvedere 1998) is also considerable, since the Mach

numbers in these discs are much lower and the relevance of density waves to the total angular momentum budget of the disc is therefore greater compared to CVs. In due course this should be accessible to similar observational tests.

CHAPTER 6

Conclusions

6.1 Dissecting the accretion disc

This thesis concerns the properties of tidally driven spirals in the discs of accreting binaries. Although first recognised more than 13 years ago (Matsuda et al. 1986) as a possible source of angular momentum transport in accretion discs, we only recently were able to provide the first convincing observational evidence for such structures (Steeghs, Harlaftis & Horne 1997). Apart from its impact on the angular momentum budget of accretion discs, the study of spiral density waves is also of relevance to the overall dynamics of the accreting material and thus the geometry of the accretion flow. The complicated vertical structure introduced by such waves, can leave a variety of observational fingerprints.

The key to the discovery of these spiral patterns was the use of the indirect imaging method Doppler tomography (Marsh & Horne 1988) to achieve images of the accretion flow with an effective angular resolution of the order of micro-arcseconds. I gave a brief discussion of this method and some related imaging techniques in Chapter 2. The detection of a spiral pattern in IP Pegasi is a prime example of the power of such imaging methods. Cataclysmic variable stars provide a rare opportunity to study the dynamical properties of thin discs in real-time because of their convenient dynamical and viscous timescales.

6.2 The dwarf nova IP Pegasi

In Chapter 3 I reviewed the observations we obtained of this spiral structure at various epochs in the binary IP Pegasi using phase resolved spectroscopy. Apart from discussing the original discovery data, I discussed follow-up observations that were obtained of the system during outburst and quiescence. These data show that the spiral pattern is a persistent structure that co-rotates in the binary frame and is present during outbursts, but not during quiescent periods. It persists for at least 8 days during outburst maximum, which is not only much longer than the orbital period of the binary (3.8 hours), but also longer than the viscous timescale of the disc (1-2 days). A natural process that can sustain such severe asymmetries in the disc is the tidal interaction of the companion star on the disc material. A tidal origin would explain its co-rotation as well as its strong dependence on the disc size. We observed an exponential decay in the accretion disc radius right from the onset of the outburst, a result that consolidates the trend established by disc radius measurements towards the end of the outburst and during quiescence (Wood et al. 1986; Wolf et al. 1993).

A simple geometrical model was used to show that the positioning of the observed spiral arms indeed conform to the properties of tidally driven spiral arms. The spiral structure is detected in the Balmer lines but also in high ionisation lines such as HeI, HeII and NIII transitions. The strong contrast between the line emission from the background disc and that of the spirals, requires severe local enhancements in temperature and/or density at the location of the spiral arms. I also showed that there is evidence for a vertically extended disc that shields the equatorial regions of the secondary from high energy irradiation.

6.3 Searching for spiral waves

In order to test if the observations fit a more realistic model of tidal spirals and to explore the feasibility to detect spiral waves in other systems, I discussed in Chapter 4 recent hydrodynamical simulations of the accretion discs in CVs (Stehle 1999). These simulations were used to calculate predicted emission line profiles and lightcurves of accretion discs carrying spiral density waves.

I compared a large, hot disc, with a smaller and cooler disc, and showed that the emission line profiles expected from such discs differ significantly. An open spiral in the outer regions of a large disc produces a strong and distinct variation of the double peaks of emission lines. This variation is very different from the properties of axisymmetric or elliptically distorted discs. In axisymmetric discs we expect a constant separation between the peaks, and in elliptical discs a smooth, sinusoidal variation with orbital phase, without sudden jumps in the peak separation or the presence of multiple peaks arising from successive spiral arms. I showed that with modest instrumental requirements such open spiral patterns can be recovered using phase resolved spectroscopy and Doppler tomography methods. Small accretion discs carrying tightly wrapped spiral waves on the other hand will produce fairly symmetric disc images, since the spiral pattern is not resolved in the Balmer emission line profiles. Some asymmetry persists, but may be difficult to disentangle from other disc asymmetries such as the bright spot. In these situations, metal lines provide a much sharper and more sensitive probe for the presence of tidal waves.

I also showed that self occultation effects may be crucial for a proper interpretation of lightcurves from high inclination systems. Work is underway to assess if one can recover the presence of tightly wrapped waves in the inner disc regions by exploiting the self occultation that occurs if density waves are present (Stehle & Steeghs, in preparation).

6.4 The success of a tidal interpretation

The detailed analysis in Chapter 4 supports the tidal spiral wave interpretation as the explanation of the observed accretion disc behaviour in IP Pegasi. The observed outburst emission line properties are reproduced in detail by a large accretion disc carrying an open spiral pattern in its outer regions. I also demonstrated that the absence of a prominent spiral pattern in quiescence is a natural consequence of the reduced tidal response on the much smaller accretion disc in combination with lower disc temperatures. These findings are supported by various independent studies that were discussed in Chapter 5.

A prediction of this model is that similar disc dynamics should be observed in other high mass transfer rate systems that carry a large and hot accretion disc. I presented some

tentative evidence for tidal structures in other systems in Chapter 5, but the available phase-resolved data of CVs in outburst is limited. Although the analysis is complicated by our poor understanding of emission line formation in the disc, it is crucial to quantify with more observations the tidal effects on the dynamics of accretion discs in CVs. The promise of directly testing the interplay of viscous and tidal angular momentum transport in accretion discs justifies a significant observational effort. Apart from obtaining new data, it is also important that the tomography methods are further developed to allow better insights into the physical properties of the discs.

The reconstructed accretion disc images clearly show that tidal effects are very important in shaping the dynamics of the accretion disc gas. This needs to be taken into account properly in order to assess the structure of time dependent accretion discs. An important conclusion of the modeling is that wave driven angular momentum transport alone does not appear to be enough to explain the observations, and a significant amount of viscous angular momentum dispersal is required to sustain a large accretion disc in outburst. This indicates that there is still a need for a varying amount of local angular momentum transport that is the trigger of the dwarf nova outbursts. Implementing various prescriptions for this local angular momentum transport and comparing the resulting simulated disc structure with observations should shed light on the physics of this local angular momentum transport through its effect on the global disc structure. The development of more realistic accretion disc models can also pave the way for a critical test of the relative contribution of global waves versus local turbulent processes to the overall angular momentum transport of accretion discs.

APPENDIX A

List of Publications

This Appendix contains a list of journal papers and conference proceedings that have been published during my Ph.D. and includes material not covered in this thesis;

Spectropolarimetry of CVs; signatures of magnetic fields in accretion flows

D.Steeghs and K.Horne

in: *Proceedings of the IAU Colloquium 163: Accretion Phenomena and Related Outflows*, ASP Conference Series Volume 121, p. 418 (1997)

A Doppler map and mass-ratio constraint for the black hole binary Nova Ophiuchi 1977

E.Harlaftis, **D.Steeghs**, K.Horne and A.Filippenko

Astronomical Journal, volume 114, p. 1170 (1997)

Spiral structure in the accretion disc of IP Peg during rise to outburst

D.Steeghs, E.Harlaftis and K.Horne

MNRAS, volume 290, L28 (1997)

Erratum: Spiral structure in the accretion disc of IP Peg during rise to outburst

D.Steeghs, E.Harlaftis and K.Horne

MNRAS, volume 296, 463 (1997)

Spiral structure in the accretion disc of IP Pegasi

D.Steeghs, E.Harlaftis and K.Horne

in: *Proceedings of the 13th North American Workshop on Cataclysmic Variables*, ASP Conference Series Volume 137 (1997)

Polars - multisite emission - multiwavelength observations

A.Schwope, K.Beuermann, D.Buckley, D.Ciardi, M.Cropper, K.Horne, S.Howell, K.Mantel, A.Metzner, R.Schwarz, M.Sirk, **D.Steeghs**, M.Still and H.Thomas

in: *Proceedings of the 13th North American Workshop on Cataclysmic Variables*, ASP Conference Series Volume 137 (1997)

Spiral shocks in the accretion disc of IP Peg during outburst maximum

E.T.Harlaftis, **D.Steeghs**, K.Horne, E.Martin and A.Magazzu

MNRAS, volume 306, 348 (1999)

On the observability of spiral structures in CV accretion discs

D.Steeghs, R.Stehle

MNRAS, volume 307, 99 (1999)

Tomography of polars

A.D. Schwope, R. Schwarz, A. Staude, C. Heerlein, K.Horne and **D. Steeghs**

in: *Proc. Annapolis Workshop on Magnetic Cataclysmic Variables (MCV2)*, ASP Conference Series (1999)

Orbital period and Doppler maps of the dwarf nova HL Canis Minoris

M. D. Still, **D. Steeghs**, V. S. Dhillon, D. A. H. Buckley

MNRAS, volume 310, 39 (1999)

Multi-epoch Doppler tomography and polarimetry of QQ Vul

A.Schwope, M.Catalan, K.Beuermann, A.Metzner, R.Smith, **D.Steeghs**

MNRAS, in press (1999) [see ASTRO.PH. 11141S]

Observing spiral waves in accretion discs

D.Steeghs, K.Horne, E.Harlaftis, R.Stehle

in: *Cataclysmic Variables: a 60th Birthday Symposium in Honour of Brian Warner*, New Astronomy Reviews (1999)

REFERENCES

- Armitage P. J., Murray J. R., 1998, MNRAS, 297, L81
- Balbus S. A., Hawley J. F., 1991, ApJ, 376, 214
- Balbus S. A., Hawley J. F., 1998, Rev. Mod. Physics, 70, 1
- Balbus S. A., Hawley J. F., Stone J. M., 1996, ApJ, 467, 76
- Baptista R., Catalan M. S., 1999, in "Cataclysmic Variables: a 60th Birthday Symposium in Honour of Brian Warner", eds. P. Charles et al, New Astronomy Reviews
- Baptista R., Horne K., Wade R. A., Hubeny I., Long K. S., Rutten R. G. M., 1998, MNRAS, 298, 1079
- Billington I., Marsh T. R., Dhillon V. S., 1996, MNRAS, 278, 673
- Binney J., Tremaine S., 1987, Galactic Dynamics. Princeton Series in Astrophysics, Princeton University Press
- Blondin J., Owen M., 1997, in "Accretion Phenomena and Related Outflows", ASP Conference Series Volume 121. p. 361
- Bobinger A., Horne K., Mantel K.-H., Wolf S., 1997, A&A, 327, 1023
- Bobinger A., 1999, private communication
- Boffin H., Haraguchi K., Matsuda T., 1999, in "Disk instabilities in close binary systems - 25 years of the disk instability model", S. Mineshige and J.C. Wheeler, eds., Universal Academy Press. p. 137
- Bonnell I. A., Bate M. R., 1994, MNRAS, 271, 999
- Brandenburg A., Nordlund A., Stein R. F., Torkelsson U., 1995, ApJ, 446, 741
- Brett J. M., Smith R. C., 1993, MNRAS, 264, 641
- Bunk W., Livio M., Verbunt F., 1990, A&A, 232, 371
- Chandrasekhar S., 1961, Hydrodynamic and Hydromagnetic Stability. Dover publications, New York
- Cook M. C., Warner B., 1984, MNRAS, 207, 705
- Cordova F. A., Mason K. O., 1982, ApJ, 260, 716
- Cowley A. P., 1992, ARA&A, 30, 287
- Crawford J. A., Kraft R. P., 1956, ApJ, 123, 44

- Cropper M., 1990, *Space Science Reviews*, 54, 195
- Dhillon V. S., Marsh T. R., 1995, *MNRAS*, 275, 89
- Dhillon V. S., 1996, in "IAU Colloq. 158: Cataclysmic Variables and Related Objects", *ASSL Conference Series Volume 208*. p. 3
- Dhillon V., 1998, in "Wild Stars in the Old West", *Proceedings of the 13th North American Workshop on CVs*, *ASP Conference Series 137*. p. 132
- Duerbeck H. W., 1987, *Space Science Reviews*, 45, 1
- Echevarria J., Diego F., Tapia M., Costero R., Ruiz E., Salas L., Gutierrez L., Enriquez R., 1989, *MNRAS*, 240, 975
- Ferguson D. H., 1997, *ApJ*, 486, 987
- Frank J., King A. R., 1981, *MNRAS*, 195, 227
- Frank J., King A., Raine D., 1985, *Accretion power in astrophysics*. Cambridge University Press, Cambridge
- Goad M. R., O'Brien P. T., Gondhalekar P. M., 1993, *MNRAS*, 263, 149
- Godon P., Livio M., Lubow S., 1998, *MNRAS*, 295, L11
- Goranskij V. P., Lyutyj V. M., Shugarov S. Y., 1985, *Pis ma Astronomicheskii Zhurnal*, 11, 696
- Hameury J. M., Menou K., Dubus G., Lasota J. P., Hure J. M., 1998, *MNRAS*, 298, 1048
- Harlaftis E. T., Marsh T. R., 1996, *A&A*, 308, 97
- Harlaftis E. T., Horne K., Filippenko A. V., 1996, *PASP*, 108, 762
- Harlaftis E. T., Marsh T. R., Dhillon V. S., Charles P. A., 1994, *MNRAS*, 267, 473
- Harlaftis E. T., Steeghs D., Horne K., Filippenko A. V., 1997, *AJ*, 114, 1170
- Harlaftis E. T., Steeghs D., Horne K., Martin E., T. M., 1999, *MNRAS*
- Hawley J. F., Balbus S. A., Winters W. F., 1999, *ApJ*, 518, 394
- Hawley J. F., Gammie C. F., Balbus S. A., 1995, *ApJ*, 440, 742
- Heemskerk M. H. M., 1994, *A&A*, 288, 807
- Heerlein C., Horne K., Schwobe A. D., 1999, *MNRAS*, 304, 145
- Hessman F. V., Robinson E. L., Nather R. E., Zhang E. H., 1984, *ApJ*, 286, 747
- Hessman F. V., Mantel K. H., Barwig H., Schoembs R., 1992, *A&A*, 263, 147
- Hessman F. V., 1989, *AJ*, 98, 675

- Hind J. R., 1856, MNRAS, 16, 56
- Horne K., Cook M. C., 1985, MNRAS, 214, 307
- Horne K., Marsh T. R., 1986, MNRAS, 218, 761
- Horne K., Saar S. H., 1991, ApJ, 374, L55
- Horne K., Marsh T. R., Cheng F. H., Hubeny I., Lanz T., 1994, ApJ, 426, 294
- Horne K., 1985, MNRAS, 213, 129
- Horne K., 1991, in "12th North American Workshop on CVs", Ed. A. Shafter, Mount Laguna Observatory. p. 23
- Horne K., 1993, in: Accretion discs in compact stellar systems. Ed. Wheeler, J.D., World Scientific, Singapore
- Horne K., 1994, in Reverberation mapping of the Broad-line region in active galactic nuclei, ASP Conf. Series 69. p. 23
- Horne K., 1995, A&A, 297, 273
- Horne K., 1998, in "Accretion Processes in Astrophysical Systems: Some Like it Hot!" Eighth Astrophysics Conference, College Park, MD, October 1997. Edited by Stephen S. Holt and Timothy R. Kallman, AIP Conference Proceedings 431. p. 426
- Ichikawa S., Osaki Y., 1994, PASJ, 46, 621
- Kaitchuck R. H., Schlegel E. M., Honeycutt R. K., Horne K., Marsh T. R., White J. C. I., Mansperger C. S., 1994, ApJS, 93, 519
- King A. R., 1989, MNRAS, 241, 365
- Knigge C., Drew J. E., 1997, ApJ, 486, 445
- Lanzafame G., Belvedere G., 1988, MNRAS, 295, 618
- Larwood J., 1997, Ph.D. thesis, Queen Mary College, London
- Lin D. N. C., Papaloizou J., 1979, MNRAS, 186, 799
- Lipovetskij V. A., Stepanyan J. A., 1981, Astrofisica, 17, 573
- Livio M., 1994, in "Interacting Binaries", Saas-Fee Advanced Course 22. Lecture Notes 1992. Swiss Society for Astrophysics and Astronomy, XVI, Springer-Verlag Berlin Heidelberg New York
- Livio M., 1999, in "Astrophysical Discs - An EC Summer School", Astronomical Society of the Pacific, Conference series Vol #160, Edited by J. A. Sellwood and Jeremy Goodman. p. 33

- Lubow S. H., 1991, ApJ, 381, 259
- Lubow S. H., 1991, ApJ, 381, 268
- Lynden-Bell D., Pringle J. E., 1974, MNRAS, 168, 603
- Makita M., Miyawaki K., Matsuda T., 1998, MNRAS, in press
- Marsh T. R., Dhillon V. S., 1997, MNRAS, 292, 385
- Marsh T. R., Horne K., 1988, MNRAS, 235, 269
- Marsh T. R., Horne K., 1990, ApJ, 349, 593
- Marsh T. R., Horne K., Schlegel E. M., Honeycutt R. K., Kaitchuck R. H., 1990, ApJ, 364, 637
- Marsh T. R., Robinson E. L., Wood J. H., 1994, MNRAS, 266, 137
- Marsh T., 1986, Ph.D. thesis, Cambridge University
- Marsh T. R., 1988, MNRAS, 231, 1117
- Marsh R. T., 1999, in *Astrophysical Discs - An EC Summer School*, Astronomical Society of the Pacific, Conference series Vol #160, Edited by J. A. Sellwood and Jeremy Goodman, 1999, p. 3.
p. 3
- Martin J. S., Jones D. H. P., Smith R. C., 1987, MNRAS, 224, 1031
- Martinez-Pais I. G., Giovannelli F., Rossi C., Gaudenzi S., 1994, A&A, 291, 455
- Martinez-Pais I. G., Giovannelli F., Rossi C., Gaudenzi S., 1996, A&A, 308, 833
- Matsuda T., Sekino N., Shima E., Sawada K., Spruit H., 1990, A&A, 235, 211
- Matsuda T., Makita M., Yukawa H., Boffin H., 1999, in "Proceedings of Numerical Astrophysics 1998", Tokyo, Japan, 10-13 March, 1998, eds. S. M. Miyama, K. Tomisaka and T. Hanawa, Kluwer Academic Publishers. p. 207
- Meyer F., Meyer-Hofmeister E., 1981, A&A, 104, L10
- Morales-Rueda L., Marsh T., Billington I., 1999, MNRAS, in press
- Murray J. R., 1996, MNRAS, 279, 402
- Murray J. R., 1998, MNRAS, 297, 323
- O'Brien K., 2000, Ph.D. thesis, University of St. Andrews
- Odonoghue D., 1990, MNRAS, 246, 29
- Osaki Y., 1996, PASP, 108, 39
- Owen M., Blondin J., 1997, in "Accretion Phenomena and Related Outflows", ASP Conference

Series Volume 121. p. 779

Paczynski B., 1977, ApJ, 216, 822

Papaloizou J., Pringle J. E., 1977, MNRAS, 181, 441

Piche F., Szkody P., 1989, AJ, 98, 2225

Pringle J. E., 1981, ARA&A, 19, 137

Rappaport S., Joss P. C., Webbink R. F., 1982, ApJ, 254, 616

Ritter H., Kolb U., 1998, A&AS, 129, 83

Robinson E., Marsh T., Smak J., 1993, *Accretion discs in compact stellar systems*. World Scientific, Singapore

Rozyczka M., Spruit H. C., 1989, in: *Theory of accretion disks*. Kluwer, Dordrecht

Rozyczka M., Spruit H. C., 1993, ApJ, 417, 677

Rutten R., Dhillon V., 1996, in "IAU Colloq. 158: Cataclysmic Variables and Related Objects",
ASSL Conference Series Volume 208, , 21

Rutten R. G. M., Dhillon V. S., Horne K., Kuulkers E., Van Paradijs J., 1993, Nature, 362, 518

Rutten R. G. M., Van Paradijs J., Tinbergen J., 1992, A&A, 260, 213

Ryu D., Goodman J., 1992, ApJ, 388, 438

Savonije G. J., Papaloizou J. C. B., Lin D. N. C., 1994, MNRAS, 268, 13

Sawada K., Matsuda T., Hachisu I., 1986, MNRAS, 219, 75

Sawada K., Matsuda T., Inoue M., Hachisu I., 1987, MNRAS, 224, 307

Schachter J., Filippenko A. V., Kahn S. M., Paerels F. B. S., 1991, ApJ, 373, 633

Schwope A. D., et al., 1998, in "Wild Stars in the Old West", Proceedings of the 13th North
American Workshop on CVs, ASP Conference Series 137. p. 44

Schwope A. D., Mantel K. H., Horne K., 1997, A&A, 319, 894

Schwope A. D., Schwarz R., Staude A., Heerlein C., Horne K., Steeghs D., 1999, in "Annapolis
Workshop on Magnetic Cataclysmic Variables", ASP Conference Series, Volume 157, edited by
Coel Hellier and Koji Mukai. p. 71

Shakura N. I., Sunyaev R. A., 1973, A&A, 24, 337

Sion E. M., 1999, PASP, 111, 532

Skilling J., Bryan R. K., 1984, MNRAS, 211, 111

Smak J., 1981, *Acta Astronomica*, 31, 395

Smak J., 1994, *Acta Astronomica*, 44, 265

Spruit H. C., Matsuda T., Inoue M., Sawada K., 1987, *MNRAS*, 229, 517

Spruit H. C., 1987, *A&A*, 184, 173

Spruit H. C., 1999, *A&A*, submitted

Steeghs D., Stehle R., 1999, *MNRAS*, 307, 99

Steeghs D., Harlaftis E. T., Horne K., 1997, *MNRAS*, 290, L28

Steeghs D., Harlaftis E. T., Horne K., 1998, *MNRAS*, 296, 463

Steeghs D., Horne K., Marsh T. R., Donati J. F., 1996, *MNRAS*, 281, 626

Stehle R., Spruit H., 1999, *MNRAS*, 304, 674

Stehle R., 1998, in "Wild Stars in the Old West", Proceedings of the 13th North American Workshop on CVs, ASP Conference Series 137. p. 323

Stehle R., 1999, *MNRAS*, 304, 687

Still M. D., Buckley D. A. H., Garlick M. A., 1998, *MNRAS*, 299, 545

Stone J. M., Hawley J. F., Gammie C. F., Balbus S. A., 1996, *ApJ*, 463, 656

Toomre A., 1969, *ApJ*, 158, 899

Velikhov E. P., 1959, *Soviet Phys JETP*, 36, 995

Verbunt F., Bunk W. H., Ritter H., Pfeffermann E., 1997, *A&A*, 327, 602

Verbunt F., 1993, *ARA&A*, 31, 93

Verner D. A., Ferland G., Korista K., Yakovlev D., 1996, *ApJ*, 465, 487

Vrielmann S., Horne K., Hessman F. V., 1999, *MNRAS*, 306, 766

Warner B., 1995, *Cataclysmic variable stars*. Cambridge University Press, Cambridge

Webb N. T., et al., 1999, *MNRAS*, in press

Wells L. D., 1896, *Harvard Coll. Obs. Circ.*, 12

Welsh W. F., Horne K., 1991, *ApJ*, 379, 586

Whitehurst R., 1988, *MNRAS*, 232, 35

Wolf S., Mantel K. H., Horne K., Barwig H., Schoembs R., Baernbantner O., 1993, *A&A*, 273, 160

Wolf S., Barwig H., Bobinger A., Mantel K.-H., Simic D., 1998, *A&A*, 332, 984

Wood J., Crawford C. S., 1986, *MNRAS*, 222, 645

Wood J. H., Horne K., Vennes S., 1992, ApJ, 385, 294

Wood J., Horne K., Berriman G., Wade R., O'Donoghue D., Warner B., 1986, MNRAS, 219, 629

Wood J. H. et al., 1989, MNRAS, 239, 809

Yukawa H., Boffin H. M. J., Matsuda T., 1997, MNRAS, 292, 321

Zhang E. H., Robinson E. L., 1987, ApJ, 321, 813